Chip-integrated Metasurface Polarimetric Imaging Sensor and Applications

by

Jiawei Zuo

A Dissertation Presented in Partial Fulfillment
of the Requirements for the Degree
Doctor of Philosophy

Approved January 2023 by the
Graduate Supervisory Committee:

Yu Yao, Co-Chair
Chao Wang, Co-Chair
Joseph Palais
Kanupriya Sinha

ARIZONA STATE UNIVERSITY

May 2023

ABSTRACT

Polarization imaging and polarization microscopy is of great interest in industrial inspection, defense, biomedical and clinical research, food safety, etc. An ideal polarization imaging system suitable for versatile applications should be full-Stokes, compact, broadband, fast, and highly accurate within a large operation angle. However, such a polarization imaging system remains elusive among state-of-the-art technology.

Recently, flat optics based on metasurfaces have been explored for polarization detection and imaging. Compared with state-of-art, metasurface-based solutions have the advantages of compactness, great design flexibility, and feasibility for on-chip integration. This dissertation reports a dual wavelength (630 to 670nm and 480nm to 520nm) chiral metasurfaces featured with sub-wavelength dimension, extinction ratio over 10 across a broad operation bandwidth (175nm) and efficiency over 60%, which can be used for detection and generation of circular polarization (Chapter 2).

This dissertation then reports a chip-integrated full-Stokes polarimetric Complementary metal–oxide–semiconductor (CMOS) imaging sensor based on metasurface polarization filter arrays (MPFA) mentioned above. The sensor has high measurement accuracy of polarization states with an angle of view up to 40°. Calibration and characterization of the device are demonstrated, whereby high polarization states measurement accuracy (measurement error <4%) at incidence angle up to ±20° and full Stokes polarization images of polarized objects are shown. (Chapter 3).

A scalable fabrication approach based on nano imprint lithography is demonstrated, with improved fabrication efficiency, lower cost, and higher optical performance up to 10 times compared to EBL process. (Chapter 4).

Several polarization imaging applications including a dual-camera full-Stokes underwater polarization navigation system are discussed. Polarization mapping under clear sky and clear water is demonstrated for proof concept. Enhancing contrast of objects through turbid water and polarization images of silver dendrites are also discussed (Chapter 5).

Though distinctive in its advantages in rich polarization information, most existing Mueller matrix microscope (MMM) operate at single mode, narrow bandwidth with bulky components. This dissertation reports a compact, dual wavelength, dual mode MMM with satisfactory measurement accuracy (Mueller matrix (MM) measurement error$\leqslant$ 2.1%) using polarimetric imaging sensor mentioned previously, MM imaging of photonic structures, bio-tissues, etc are demonstrated for proof of concept (Chapter 6).

DEDICATION

To my family, with love.

ACKNOWLEDGMENTS

Firstly, I appreciate my supervisor, Professor Yu Yao and Professor Chao Wang. They gave me this chance to study at ASU, and they continuously supported me in completing my research. I have benefited from their encouragement and valuable advice in conducting research countless times. This dissertation could not have been finished without their help.

I am honored to have comments and guidance from my committee members: Professor Joseph Palais and Professor Kanupriya Sinha.

I want to thank the helps I received from my group members, both Professor Yu Yao and Professor Chao Wang's groups. Dr. Jing Bai, Dr. Shinhyuk Choi, Dr.Pengkun Xia, and Dr. Ali Basiri, Dr.Xiahui Chen greatly helped me with device characterization, optical alignment, FDTD simulation, and nanofabrication of polarimetric imaging sensors. Dr. Zhi Zhao helped me with spectrometer measurements. Hossain Mansur Resalat Faruque, Nabasindhu Das, and Ashutosh Bangalore helped me with the optical characterization of the polarimetric imaging sensor and polarization microscope. Dr. MD Ashif Ikbal helped me to maintain lab supplies.

Staff from ASU Nanofab, Jaime Quintero, Kevin Nordquist, Carrie Sinclair, Scott Ageno, Arthur Handugan, and Diana Convey have helped me greatly in the past years. I also appreciate Dr. Roland Himmelhuber at the University of Arizona for training and help in EBL and wafer dicing.

I hold my deepest gratitude to my family members, including my parents and parents-in-law, for their support, love, and encouragement throughout my Ph.D. study. Last but not least, I would like to thank my lovely wife, Karchyi Chang, for her love, support, and upbringing life attitude. Because of her, I have finally reached the end of my Ph.D. life without frustration or giving up.

TABLE OF CONTENTS

Page

LIST OF TABLES

Table Page

LIST OF FIGURES

Figure Page

Figure Page

Figure Page

Figure Page

Figure Page

CHAPTER 1

INTRODUCTION

Polarization, together with intensity and wavelength, are one the three fundamental properties of light. Detection of polarization and manipulation of polarization of light have been applied nearly every aspect of our life: from the target detection[1], biomedical and clinical research[2], optical communication[3], remote sensing[4], industrial inspection[5] , 3D displays[6] and so forth. Conventional methods for controlling polarization require rotating bulky optical setup, which limits its application range and miniaturization. To date, a fast, compact, broadband full-Stokes polarization imaging sensor with high measurement accuracy over large angle of view remains elusive among the State-of-the-art technologies. Flat optics based on metasurfaces has distinct advantages in its ultra-compactness, large design flexibility, promising to address the issue mentioned above. In this chapter, we presented an introduction to physics of polarization, Stokes parameters and Mueller calculus. Lastly, we briefly discuss a summary of the existing state-of-the art polarization imaging techniques.

1.1. Electromagnetic Waves and Polarization.

The polarization is one the fundamental properties of electromagnetic (EM) waves that describes the geometrical orientation of EM wave oscillation [7]. Define an EM plane wave propagating along the z-direction, the electric field in time-harmonic form can be expressed by:

$$\boldsymbol{E}(z,t) = E_x + E_y = E_{x0} cos(\mathrm{kz} - \omega t) + E_{y0} cos(\mathrm{kz} - \omega t + \Delta\varphi) \qquad (1.1)$$

Where $\Delta\varphi$ corresponds to the phase difference of input electric field E_x and E_y. E_{x_0} and E_{y0} are the amplitude of E_x and E_y respectively. k is the propagation constant of the light along z-direction where light is propagating at. Inserting equation above into the Helmholtz wave equation we get:

$$\frac{E_x(z,t)^2}{E_{x0}^2} + \frac{E_y(z,t)^2}{E_{y0}^2} - \frac{2E_x(z,t)E_y(z,t)}{E_{x0}E_{y0}} cos\Delta\varphi = sin^2\Delta\varphi \qquad (1.2)$$

Plotting the equation above in the cartesian coordinates, we can get a ellipse, defined as polarization ellipse, as shown in Figure 1.1.

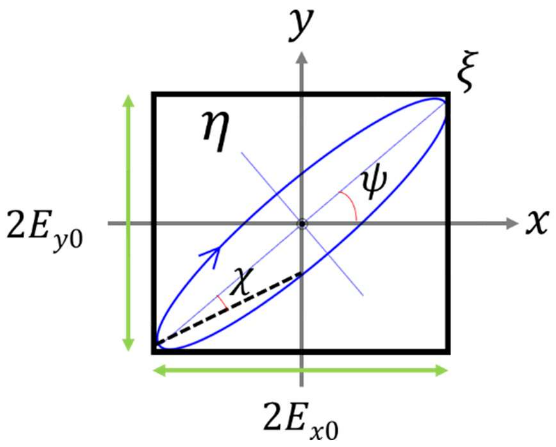

Figure 1.1: Illustration of a polarization ellipse in η,ξ coordinate system. ψ is the azimuth angle of the polarization ellipse, χ denotes the ellipticity angle.

The major axis of the polarization ellipse is along ξ direction and the minor axis of polarization ellipse is along η direction, the angle ψ between axis ξ and x direction specifies the angle of polarization (AOP) and χ denotes the ellipticity angle.

There are two special cases besides elliptical polarization: linear polarization (LP), where EM waves only oscillates along one direction, i.e., ξ direction. Another case is circular polarization (CP), whose trace is a perfect circle shape. According to how light is traced, CP can be divided into right-handed polarization (RCP) and left-handed polarization (LCP) [8]. Here we trace light along the propagation direction, LCP is defined in clockwise, and RCP is defined counterclockwise.

1.2. Stokes Parameters and Poincare' Sphere.

Although polarization ellipse is a convenient mathematical tool for visualizing polarization, it has two major limitations. First, it is time dependent, thus is an instantaneous representation of polarization, not possible to be measured. Second, the ellipticity angle cannot be directly measured too. To solve these issues, Stokes parameters were derived from the polarization ellipse equation firstly by Stokes (1852) [9] after taking the time average of polarization ellipse, accounting for parts of EM waves whose phase are not random in time, i.e. polarized part, yielding the equation:

$$\begin{pmatrix} S_0 \\ S_1 \\ S_2 \\ S_3 \end{pmatrix} = \begin{pmatrix} E_{x0}^2 + E_{y0}^2 \\ E_{x0}^2 - E_{y0}^2 \\ E_{x0}E_{y0}cos\Delta\varphi \\ 2E_{x0}E_{y0}sin\Delta\varphi \end{pmatrix} \tag{1.3}$$

Where S_0 describes the intensity of EM wave; S_1 describes the EM wave amplitude difference projected onto 0 and 90 degrees from the x-axis, S_2 describes the EM wave amplitude difference projected onto 45 and 135 degrees from the x-axis; S_3 describes the difference between the CP components of EM waves. For fully polarized light, the relationship between S_0 , S_1 , S_2 , S_3 can be written as:

$$S_0^2 = S_1^2 + S_2^2 + S_3^2 \tag{1.5}$$

For partially or unpolarized light, the relationship between S_0 , S_1 , S_2 , S_3 becomes unequal, as unpolarized part of light cannot be taken into time averaging because of its randomness:

$$S_0^2 > S_1^2 + S_2^2 + S_3^2 \tag{1.6}$$

The degree of polarization (DOP) is applied to describe the extent of light being polarized; DOP can be calculated via the equation:

$$DOP = \frac{\sqrt{S_1^2+S_2^2+S_3^2}}{S_0^2} \tag{1.7}$$

Similarly, we define degree of circularly polarization (DOCP) and degree of linear polarization (DOLP) to determine how much light is circularly polarized or linearly polarized, DOCP is written as equation below:

$$DOCP = \frac{S_3}{S_0} \tag{1.8}$$

DOLP is defined as :

$$DOLP = \frac{\sqrt{S_1^2+S_2^2}}{S_0^2} \tag{1.9}$$

In addition, Angle of polarization (AOP) , which is the azimuth angle ψ of the polarization ellipse can be calculated using equation:

$$AOP = \frac{1}{2}\arctan\left(\frac{S_2}{S_1}\right) \tag{1.10}$$

Poincaré sphere is a convenient method to visualize the Stokes parameters, developed by Poincaré (1892) [10], an arbitrary polarization state plotted on Poincaré sphere plotted is shown in Figure 1.2, where three major axis corresponds to S_1 S_2, S_3, respectively. Yellow vector length is corresponding to DOP, therefore, for polarization states that are fully polarized, polarization vector has length of 1 and thus these polarization states are locating on the surface of the Poincaré sphere. As for partially polarized light, their Stokes parameters will locate inside the Poincaré sphere.

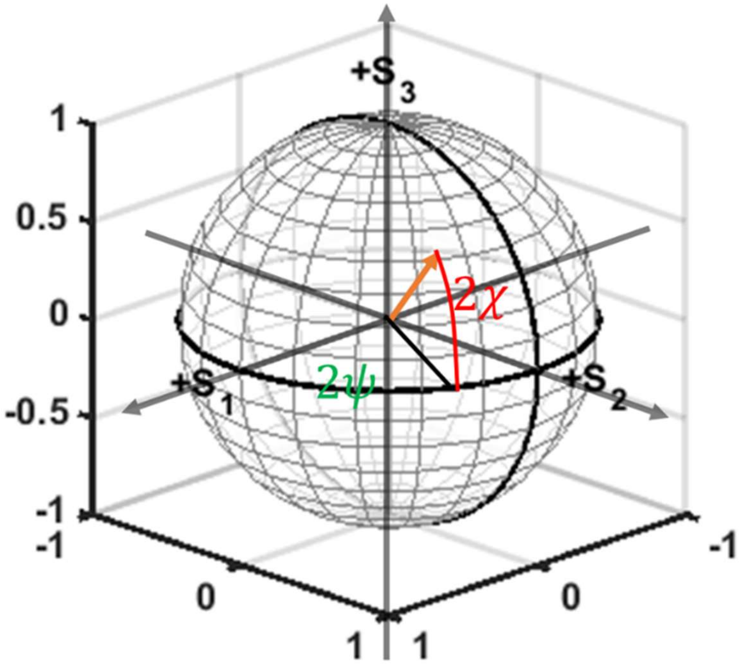

Figure 1.2: Stokes vector on Poincare' sphere. ψ is the azimuth angle of the polarization ellipse, χ denotes the ellipticity angle.

1.3. Jones Calculus and Mueller Calculus.

Fully polarized light can be described using the jones calculus [10], firstly discovered by Jones(1941)[11]. We can describe the EM complex amplitude as:

$$\boldsymbol{E}=\begin{pmatrix}\boldsymbol{E_x(t)}\\ \boldsymbol{E_y(t)}\end{pmatrix}=\begin{pmatrix}\boldsymbol{E_{0x}e^{i(kz-\omega t+\phi_x)}}\\ \boldsymbol{E_{0y}e^{i(kz-\omega t+\phi_y)}}\end{pmatrix}=\begin{pmatrix}\boldsymbol{E_{0x}e^{i\phi_x}}\\ \boldsymbol{E_{0y}e^{i\phi_y}}\end{pmatrix}\boldsymbol{e^{i(kz-\omega t)}} \tag{1.11}$$

Where $\begin{pmatrix} E_{0x}e^{i\phi_x} \\ E_{0y}e^{i\phi_y} \end{pmatrix}$ is the jones vector. E_{0x} E_{0y} are the amplitude of the electric filed component along *x,y* directions respectively. ϕ_x, ϕ_y describes phase of electric field along *x, y* directions.

Jones matrix describes the polarization response of objects by linking input E_{in} and output jones vectors E_{out} :

$$\begin{pmatrix} E_x^{out} \\ E_y^{out} \end{pmatrix} = \begin{pmatrix} j_{xx} & j_{yx} \\ j_{xy} & j_{yy} \end{pmatrix} \cdot \begin{pmatrix} E_x^{in} \\ E_y^{in} \end{pmatrix} \tag{1.12}$$

For light that is unpolarized or partially polarized, Mueller calculus is required. One thing worth notice is that, only jones calculus can be applied to coherent light as Mueller calculus is based on time averaging of measured light intensity[12]. Mueller calculus is discovered by Mueller (1943) to describe the manipulation of Stokes parameters by the optical system using a 4×4 matrix called Mueller matrix. The Mueller matrix can link the input and output Stokes parameters using the equation:

$$\begin{pmatrix} S_0^{out} \\ S_1^{out} \\ S_2^{out} \\ S_3^{out} \end{pmatrix} = \begin{pmatrix} m_{00} & m_{01} & m_{02} & m_{03} \\ m_{10} & m_{11} & m_{12} & m_{13} \\ m_{20} & m_{21} & m_{22} & m_{23} \\ m_{30} & m_{31} & m_{32} & m_{33} \end{pmatrix} \cdot \begin{pmatrix} S_0^{in} \\ S_1^{in} \\ S_2^{in} \\ S_3^{in} \end{pmatrix} \tag{1.13}$$

A linear polarizer i.e., linear diattenuation with polarization axis 0°, the linear polarization extinction ratio (LPER) can be calculated using maximum transmission q and minimum transmission r:

$$LPER = \frac{q}{r} \tag{1.14}$$

The Mueller matrix of such linear diattenuator can be written as [13]:

$$\begin{pmatrix} q+r & q-r & 0 & 0 \\ q-r & q+r & 0 & 0 \\ 0 & 0 & 2\sqrt{qr} & 0 \\ 0 & 0 & 0 & 2\sqrt{qr} \end{pmatrix} \tag{1.15}$$

The Mueller matrix of a linear retarder with retardance δ and fast axis at 0°can be written as:

$$\begin{pmatrix} 1 & 0 & 0 & 0 \\ 0 & 1 & 0 & 0 \\ 0 & 0 & cos\ \delta & sin\ \delta \\ 0 & 0 & -sin\ \delta & cos\ \delta \end{pmatrix} \tag{1.16}$$

The Mueller matrix after rotating these optical elements by an angle θ by following the right-hand rule, can be described using the equation:

$$M(\theta) = R(-2\theta)M(0)R(2\theta) \tag{1.17}$$

where $R(2\theta)$ is the rotation matrix, written as:

$$R(2\theta)=\begin{bmatrix} 1 & 0 & 0 & 0 \\ 0 & \cos{(2\theta)} & \sin{(2\theta)} & 0 \\ 0 & -\sin{(2\theta)} & \cos{(2\theta)} & 0 \\ 0 & 0 & 0 & 1 \end{bmatrix} \tag{1.18}$$

On the other hand, Jones matrix can also be converted to Mueller matrix[14], using the equation:

$$M = A(J \otimes J^{*})A^{-1} \tag{1.19}$$

Where $\otimes$ is Kronecker product, and A can be written as:

$$A = \begin{pmatrix} 1 & 0 & 0 & 1 \\ 1 & 0 & 0 & -1 \\ 0 & 1 & 1 & 0 \\ 0 & -i & i & 0 \end{pmatrix} \tag{1.20}$$

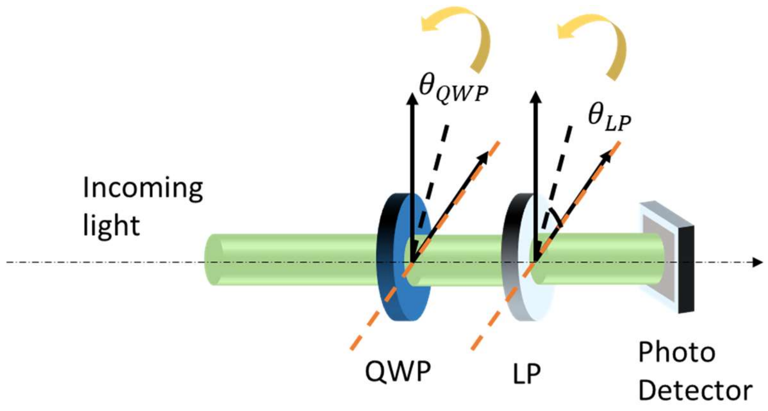

Figure 1.3: Schematic of measuring input light Stokes parameters by rotating polarizer axis of LP and fast axis of QWP.

In this section, we discuss the traditional method for measuring the polarization states by rotating optical components, such as linear polarizers (LP) and quarter waveplates (QWP). Normally, there are three ways of measuring the polarization states, method one is rotating QWP and LP to specific angles to measure the Stokes parameters by directly subtracting transmission intensities [13]. The experimental setup for method one is shown in Figure 1.3. In measurement, we need to firstly remove QWP, and then add QWP and keep its fast axis ±45° with respect to LP axis, Stokes parameter of fully polarization light can be obtained using the equation:

$$\begin{pmatrix} S_0 \\ S_1 \\ S_2 \\ S_3 \end{pmatrix} = \begin{pmatrix} I_0 + I_{90} \\ I_0 - I_{90} \\ I_{45} - I_{135} \\ I_{RCP} - I_{LCP} \end{pmatrix} = \begin{pmatrix} I_{45} + I_{135} \\ I_0 - I_{90} \\ I_{45} - I_{135} \\ I_{RCP} - I_{LCP} \end{pmatrix} = \begin{pmatrix} I_{RCP} + I_{LCP} \\ I_0 - I_{90} \\ I_{45} - I_{135} \\ I_{RCP} - I_{LCP} \end{pmatrix} \tag{1.21}$$

Where I_0, I_{90}, I_{45} , I_{135} are the transmitted intensity measured by linear polarizers (LP) with polarization axis along 0°, 45°, 90°, 135° respectively. I_{RCP} and I_{LCP} are transmitted intensity measured by RCP and LCP polarizers, respectively. CP polarizers can be constructed by rotating QWP fast axis ±45° with respect to LP axis. For partially polarized light, it is required to measure the background intensity without use of QWP and LP to obtain absolute value of S_0.

The advantage of method one is it is the straightforward and fast in determining the Stokes parameter. However, method one normally requires users to accurately align LP and QWP axis before measurements to avoid systematic error. Another drawback is the measurement requires high LPER for LP and QWP with retardance of $\frac{\lambda}{4}$ to achieve high measurement accuracy, which is practically expensive to achieve.

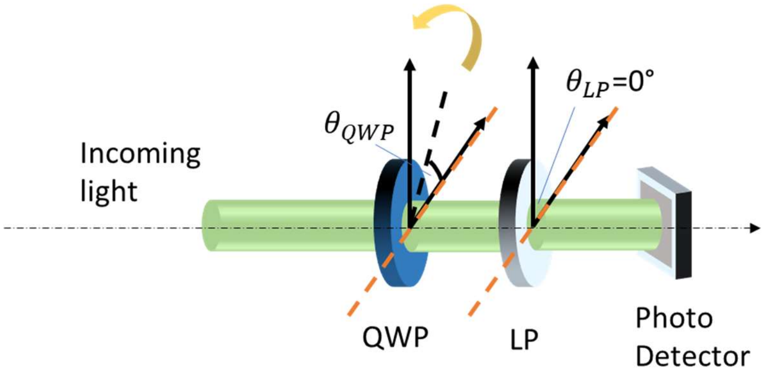

Figure 1.4: Schematic of measuring input light Stokes parameters by rotating fast axis angle of QWP.

The second method for measuring Stokes parameters is by rotating the fast axis angle θ_{QWP} of QWP while keep the angle of LP at constant value $\theta_{LP} = 0°$ [15]. The experimental setup for method two is shown in Figure 1.3. In this method, the intensity measured by the photo detector $I(\theta)$ can be expressed using the following equation:

$$I(\theta) = \frac{1}{2}(S_0 + S_1 \cos^2 2\theta + S_2\, cos\, 2\theta\, sin\, 2\theta + S_3 sin\, 2\theta) \tag{1.22}$$

Where θ is the fast axis angle of QWP. Equation above can be rewritten using the trigonometric half-angle formula:

$$I(\theta) = \frac{1}{2}(A + B\, sin\, 2\theta + C\, cos\, 4\theta + D\, sin\, 4\theta) \tag{1.23}$$

Where:

$$A = S_0 + \frac{S_1}{2}, B = S_3, C = \frac{S_1}{2}, D = \frac{S_2}{2} \tag{1.24}$$

For this Fourier series, the highest frequency is 4θ, therefore, the minimum amount of data points required to obtain A, B, C, D is 8 according to Nyquist sampling theorem. Here is an example, suppose one take measurement of input polarization state using method three, he would need to measure 8 or $N \geq 8$ points, N is an even number. The A, B,C,D can then be obtained using equations:

$$A = \frac{2}{N}\sum_{n=1}^{N} I_n \;,\; B = \frac{4}{N}\sum_{n=1}^{N} I_n\, sin\, 2\theta_n \tag{1.25a}$$

$$C = \frac{4}{N}\sum_{n=1}^{N} I_n\, cos\, 4\theta_n\, , D = \frac{4}{N}\sum_{n=1}^{N} I_n\, sin\, 4\theta_n \tag{1.25b}$$

Where $\theta_{n+1} = \theta_n + 180°/N$. I_n is the normalized intensity of photo detector recording each time. The Stokes parameter can then be reconstructed by:

$$S_0 = A - C\, , S_1 = 2C, S_2 = 2D, S_3 = B \tag{1.26}$$

The third method for measuring the Stokes parameter S_0, S_1, S_2, and absolute value of S_3 of input light can be done by rotating θ_{LP} , this method does not require a QWP. The relationship between intensity measured by the photodetector with LP angle θ_{LP} can be expressed as:

$$I(\theta_{LP}) = E_{0x}^2 \cos^2 \theta_{LP} + E_{0y}^2 \sin^2 \theta_{LP} + E_{0x}E_{0y}\sin 2\theta_{LP} cos\Delta\phi \tag{1.27}$$

Where $\Delta\phi$ is the phase difference between E_x and E_y of jones vector, E_{0x}^2 , E_{0y}^2 is the intensity along x, y direction. Complex value of E_x, E_y can be fitted with $I(\theta_{LP})$ of over 4 or more different LP angles input. The Stokes parameter can then be converted from fitted jones vector results. For high measurement accuracy, a larger number of points is preferred for least square fitting method. The requirement of LPER of LP is high for this method, it is better to use LPER higher than 10000 to reduce measurement error to less than 0.5%.

1.5. Polarization Detection Techniques

As mentioned in the section 1.4, conventional evaluation of polarization states requires manually rotating optical components like LP and QWP, the requirement of moving parts limited its application range and bulky size of the experimental setup hinders miniaturization of the system. In this section, we briefly introduce the working principle of the state-of-the-art polarization techniques and compare their advantages and disadvantages.

So far, several types of polarimetry imager were proposed, including division of time (DoT)[16], division of amplitude (DoA)[17] and division-of-focal-plane(DoFP)[18-20] to achieve more compact or automatic polarization imaging.

A representative DoT technique is proposed by Salsa Corp ltd[16], where an electric modulated liquid crystal layer is added in front of a linear polarizer as a polarization state analyzer (PSA). The PSA is then added in front of the charged coupled device (CCD) camera to form a full Stokes polarization camera. During the measurement, linear crystals are modulated every few mS while CCD captures the images, the Stokes parameters can then be extracted using the method three mentioned in the section 1.4. The advantage of this method is it has measurement accuracy. However. the Stokes parameters needs multiple frames to be measured, thus the imaging speed of it is fundamentally limited.

Another measurement method is based on DoA[17], where incoming light is divided into multiples channels. One part of Stokes parameters can be recorded simultaneously in each channel. Full Stokes parameters can be obtained after combining the information obtained from cameras in each channel. This method does not have moving parts, the measurement speed thus can be much faster. However, this method requires complex optical components and multiple cameras, making system is bulky and expensive.

In the last decade, another type of polarimetric imaging sensor based on DoFP has been demonstrated [19, 21]. Generally, these DoFP based polarimetric imagers integrated four micro polarizers with unique directions onto neighboring pixels of the CMOS sensor for detecting S0, S1, S2. Compared to DoT and DoA based polarimeters, DoFP is the most compact, less costly technique to date, as it requires no moving part and less complex optics, and the frame rate is not limited to any optics. Despite many advantages, these devices are limited to only linear polarization (LP) detection. Recently, a micro retarder layer has been added onto DoFP polarization imaging sensor (Sony IMX250MYR) to enable full Stokes detection[17]. Full Stokes parameters are obtained after registering the analyzer vector. However, the retarder pixels have uniformity issues due to stress of substrate, causing gaps between them, which leads to optical crosstalk and thereby limiting its operation angle. So far, an full Stokes DoFP polarization imager that can operate at broad angle of view with high measurement accuracy remains challenging.

1.6. Measurement of Mueller Matrix

Mueller matrix of objects can be obtained using experimental setup similar to the ones for measuring the Stokes parameters. The difference is to obtain Mueller matrix of objects, it is required to have both polarization states generator (PSG) and polarization states analyzer (PSA). The optical path of a PSG can be treated as an inverse of a PSA.

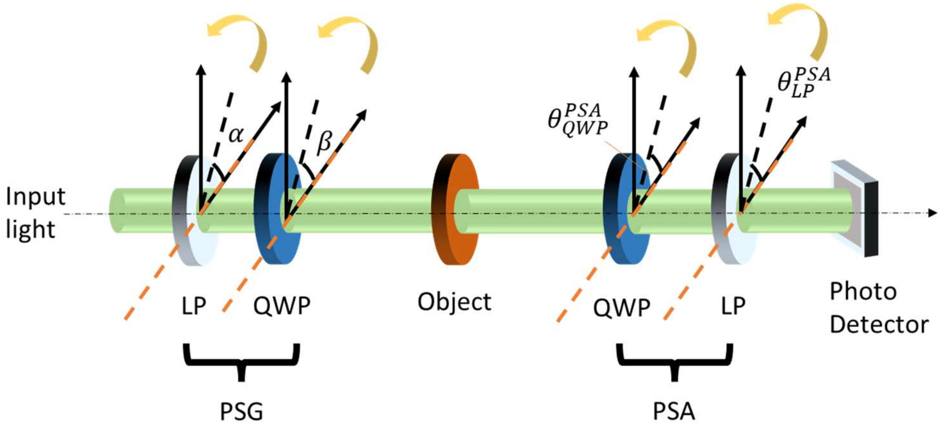

Figure 1.5: Schematic of measuring Mueller matrix of an object in transmission mode using PSG and PSA.

A typical experimental setup for measuring Mueller matrix of sample in transmission mode is shown in Figure 1.5. Relationship between generated polarization states S_{in} and angle of LP axis α, and angle of QWP fast axis β of PSG can be expressed as:

$$S_{in} = S_0 \times \begin{pmatrix} 1 \\ cos\ 2\beta\ cos\ (2\beta - 2\alpha) \\ sin(2\beta) cos\ (2\beta - 2\alpha) \\ sin(2\beta - 2\alpha) \end{pmatrix} \tag{1.28}$$

Several different methods are proposed to measure the Mueller matrix of the objects. One of the most common methods is generating N≥ 4 polarization states $S_{in_{4\times N}}$, the transmitted polarization states is then measured as $S_{out_{4\times N}}$ using PSA with method one or method two mentioned in the section 1.4. The Mueller matrix of the object can then be calculated using the equation:

$$M_{objects} = S_{out_{4\times N}} \cdot {S_{in_{4\times N}}}^{-1} \tag{1.29}$$

It is noteworthy that the most common method for solving the inverse of matrix is by lower Upper (LU) decomposition of the input matrix [22], the issue is that when N= 4, $M_{objects}$ is often easily affected by the measurement error of Stokes parameters. Therefore, an input of N≥ 4 polarization states is often preferred to make the equation over defined, the Mueller matrix can then be calculated by solving linear equations via fitting [23].

1.7. Mueller Matrix Decomposition

Mueller matrix polar decomposition (MMPD) is a mathematical interpretation method for Mueller matrix to extract physical information hidden inside the Mueller matrix of objects. This section discuss one of the most common Mueller matrix decomposition method, proposed by Lu-Chipman [24]. A normalized Mueller matrix M_S can be written as below:

$$M_S = \begin{pmatrix} 1 & \vec{D} \\ \vec{P} & \boldsymbol{m} \end{pmatrix} \tag{1.30}$$

Where $\vec{P}$ is the polarizance vector, $\vec{D}$ is the diattenuation vector, and $\boldsymbol{m}$ is a 3×3 submatrix, defined as:

$$\vec{P} = \begin{pmatrix} m_{10} \\ m_{20} \\ m_{30} \end{pmatrix}, \vec{D} = \begin{pmatrix} m_{01} & m_{02} & m_{03} \end{pmatrix}, \boldsymbol{m} = \begin{pmatrix} m_{11} & m_{12} & m_{13} \\ m_{21} & m_{22} & m_{23} \\ m_{31} & m_{32} & m_{33} \end{pmatrix} \tag{1.31}$$

The polarizance p and diattenuation d can then be calculated as:

$$p = \frac{\sqrt{m_{10}^2+m_{20}^2+m_{30}^2}}{m_{00}}, \quad \mathrm{d}=\frac{\sqrt{m_{01}^2+m_{02}^2+m_{03}^2}}{m_{00}} \tag{1.32}$$

In addition, Mueller matrix of sample can be decomposed into a depolarizing matrix M_{Δ} , diattenuation matrix M_D and retardation matrix M_R:

$$M_S = M_{\Delta} \cdot M_R \cdot M_D \tag{1.33}$$

The depolarization coefficient Δ can be calculated using equation:

$$\Delta = 1 - \frac{|\mathrm{tr}(M_{\Delta}) - 1|}{3} \tag{1.34}$$

Where $\mathrm{tr}(M_{\Delta})$ is the trace of the depolarization matrix M_{Δ}.

The retardance R can be calculated using equation:

$$R = \mathrm{acos}\,(\frac{\mathrm{tr}(M_R)}{2} - 1) \tag{1.35}$$

Where $\mathrm{tr}(M_R)$ is the trace of the retardance matrix M_R, specifically, linear retardance LR, and circular retardance CR can then be calculated using elements of M_R:

$$\mathrm{LR}{=}\mathrm{acos}(sqrt\left(\left(M_{R_{11}} + M_{R_{22}}\right)^2 + \left(M_{R_{21}} + M_{R_{12}}\right)^2\right) - 1) \tag{1.36}$$

$$\mathrm{CR}{=}\mathrm{acos}(\frac{M_{R_{21}} - M_{R_{12}}}{M_{R_{11}} + M_{R_{22}}}) \tag{1.37}$$

CHAPTER 2

DUAL WAVELENGTH CHIRAL METASURFACES

Polarization imaging can uncover an object's unique features invisible to conventional imaging with intensity and color information. Thus, it is of great interest in industrial inspection, defense, biomedical and clinical research, food safety, etc. Traditional methods for polarization imaging require complex optical components and moving parts, which makes system miniaturization challenging. An ideal polarization imaging system suitable for versatile applications should be full-Stokes, compact, broadband, fast, and highly accurate within a large operation angle. However, such a polarization imaging system remains elusive among state-of-the-art technology. Recently, flat optics based on metasurfaces have been explored for polarization detection and imaging. Compared with state-of-art, metasurface-based solutions have the advantages of compactness, great design flexibility, and feasibility for on-chip integration. This chapter discusses the design of dual-working wavelength chiral metasurfaces and vertically coupled Aluminum double-layered gratings (VCDG) for full Stokes polarization detection. The demonstrated design shows an operation bandwidth of over 175nm and high efficiency at red color (650nm) upon normal incidence. We then discussed the device performance at oblique incidence and its impact on a higher angular field of view full Stokes polarization detection.

2.1. Introduction

It is no exaggeration to say that the development of imaging systems has profoundly impacted our lives, from smartphone cameras to the most advanced medical imaging equipment and even to space exploration. Besides light intensity and color, capturing the polarization state of light emitted, scattered, or transmitted by an object has been proven to be essential for various applications such as target detection [1, 25, 26], biomedical diagnostics [27, 28], remote sensing [4], defense [29], and astronomy [30], etc. Thus, it is highly desirable, though challenging, to provide a compact and economical solution for a polarimetric imaging system, where not only the light intensity at each pixel is recorded, but also the polarization state at each pixel is also collected to provide complete information on the sample under test.

Recent development in optical metasurfaces has enabled much more compact, flexible and robust solutions for polarization manipulation and detection than polarization filters based on liquid crystal polymers or linear retarders [17, 20]. Thus metasurface-based polarization imagers and polarimeters have been extensively explored in the past decades. Among these designs, the circular polarization (CP) detection device based on plasmonic [31-34] and dielectric metasurface[35] was first produced, as CP detection is conventionally much more difficult than LP detection due to the lack of natural optical materials with strong chirality. Recently, metasurface-based full Stokes polarimeters and even polarization imagers have been experimentally reported [36-48]. Among them, the dielectric metasurfaces based on diffraction can achieve high efficiency and are highly compact [36-39]. However, their working bandwidth is limited to less than 10nm in the visible range due to complexities in diffraction phase mask design [37, 38]. In addition, the dielectric metasurfaces based on resonances achieve high efficiency and circular dichroism [40], but the working wavelength is limited to near infrared (NIR). Plasmonic structures have achieved large working bandwidth [41, 42, 47], high detection accuracy [41, 43], and direct integration with photodetector[44, 46, 48] for infrared wavelengths. In the visible wavelength range, polarization detection with high efficiency, high detection accuracy, and direct integration with imaging sensors remains challenging for plasmonic structures due to high optical loss. Dielectric gratings or metalens [36-39] have achieved ultra-compactness and high efficiency in visible [36-39], yet their incidence angle and operation bandwidth remains normal incidence and less than 10nm respectively due to their angular and chromatically dispersive nature; metal-dielectric hybrid metasurfaces have been used for chiral metasurfaces and polarization detection with high efficiency and performance for near IR wavelengths [45] and is suitable for extending into visible range, leveraging the advantages in high efficiency of metal and broadband width of plasmonic structures. Despite the great achievement of previous works for metasurface-based polarization detectors, most of those polarization controlling effects were demonstrated mostly under normal incidence [37, 49] or narrow incidence angle of ±5° [38]. Therefore, ultra-compact high speed full-Stokes polarimetric imaging sensors for visible wavelengths with high efficiency, high detection accuracy, and broad AFOV remains elusive.

In this chapter, we employ a metal-dielectric hybrid design concept [45] in the visible regime for CP detection because of its efficiency, chirality, and integrability advantages onto photodetectors. We attribute the dual-wavelength operation to the unique design of the multi-order quarter-wave plate (QWP), like birefringent Si nanograting, as part of the chiral metasurface design. At wavelengths centered around 500nm, Si nanograting exhibits leaky guided and mie resonance hybrid mode along the grating width direction and acts as an absorber along the grating length direction, leading to an advance phase of $\frac{3}{2}\pi$ at grating width direction. At wavelengths centered around 630nm, the a-Si nanograting exhibit leaky guided mode along the grating width direction, a Fabry Perot mode along the grating length direction, resulting in an advance phase of $\frac{1}{2}\pi$ at grating width direction. (See table 2.1 for a detailed comparison between our device with other metasurface based full Stokes polarimeters)

Table 2. 1. Full Stokes polarimetric detectors based on metasurfaces

Full Stokes polarimeters	materials	Chip Integrated?	Detection error	FOV	Operational wavelength
Our Work	Dielectric metal Hybrid	Yes	<2% (S1,S2,S3) at normal incidence <4% (S1,S2,S3) at ±20° incidence at red color	40° for red 10° for cyan	630-670nm(red) 480-520nm(cyan)
Graphene, plasmonic hybrid	metal	No	<3.9% (S1), <6.5% (S2), <2.5% (S3)	normal incidence	6.7μm-6.8μm
		Yes	<50%(S3) Ellipticity:7~10degree AOP:7~14 degree	normal incidence	Narrow band 1.55μm
Plasmonic metasurface		No	<0.44%(S1), <1.4% (S2), < 0.79%(S3)	normal incidence	3.5 to 5 μm
		No	7.3–12.3% (S1), 7.2–27.4% (S2), 5.2–17.7% (S3)	normal incidence	Narrow band 830nm
		No	<2.3% (DOLP) <10.3% (DOCP)	normal incidence	3.725 μm to 3.875 μm
		No	<45% (S1, S2, S3)	normal incidence	750-1050nm
Plasmonic scatters		No	>6% (S1), >5.8% (S2), >4.7% (S3)	normal incidence	1500–1565 nm
Plasmonic diffractor		No	<50%(S1) <30%(S2) <20%(S3)	normal incidence	400nm-640nm

Table 2.1. Full Stokes polarimetric detectors based on metasurfaces(continued)

Full Stokes polarimeters	materials	Chip integrated?	Detection error	FOV	Operational wavelength
Our work	Dielectric-metal hybrid	Yes	<2% (S1,S2,S3) at normal incidence <4% (S1,S2,S3) at ±20° incidence at red color	40° for red 10° for cyan	630-670nm(red) 480-520nm(cyan)
Dielectric gratings	Dielectric	No, Requires spacing	DOP error < 20%	Normal incidence	Narrow band 530nm
Dielectric gratings		No, Requires space for focus	DOP error <1.59%	Normal incidence	Narrow band 808nm
Dielectric Nanobar on gold nanowires	Dielectric-metal hybrid	No	<1.9% (S1), <2.7% (S2), <7.2% (S3)	normal incidence	1.3-1.6 µm

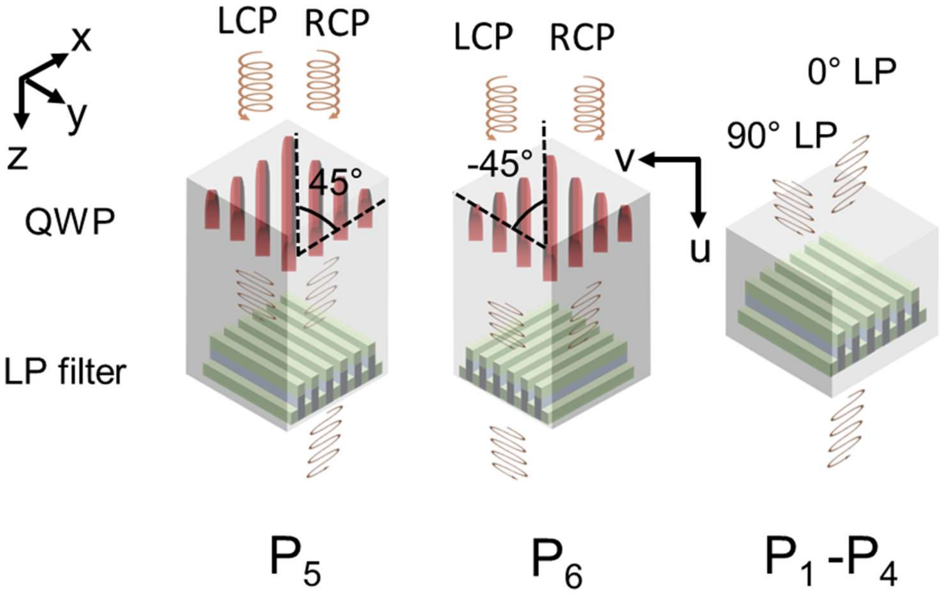

Figure 2.1: 3D Conceptual illustration of a pair of chiral metasurfaces responsible for transmitting RCP and LCP light, respectively (P5, P6) and an LP filter (P1-P4)

Zoomed-in illustrations of LCP filters, RCP filters, and LP filters are shown in Figure 2.1. For LP filters, we adopted vertically coupled [50, 51] double-layered Aluminum gratings(VCDG) because of its high linear polarization extinction ratios (LPER) and fabrication simplicity compared to single-layered wire grid polarizers as VCDG does not require the etching of metal. For CP filters, we designed a metal-dielectric hybrid chiral metasurface structure composed of Si metasurface with artificial birefringence (top), a dielectric spacing layer, and a VCDG (bottom). Both LP and CP polarization filters have a thickness of less than a wavelength, resulting in a highly compact form factor for the demonstrated full-stokes polarimetric imaging camera.

2.3. Full Wave Simulation of VCDGs

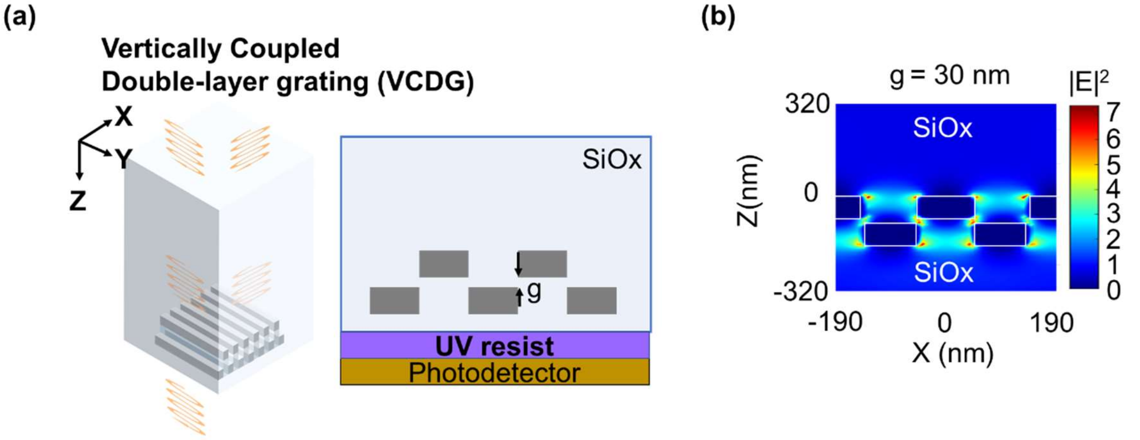

Figure 2.2: Design of the VCDG for LP detection. (a). 2D schematic of VCDG cross-section. The thickness of Aluminum (Al), width, period, and the vertical gap of VCDG are tAl= 80nm, p1=190nm, wAl = 95nm, and g=30nm, respectively. (b). Cross-sectional view of VCDG near field distribution with TM polarization input at 650nm.

Previously, we applied single-layer gold (Au) nanogratings for LP detection in near-infrared (NIR)[45]. In this work, we used Aluminum (Al) to reduce optical loss in the visible range. In addition, VCDG composed of vertically stacked bi-layer Al nanowires was applied as LP filters, as shown in Figure 2.2(a). The vertical nanogap (g) between the top and bottom Al nanowires is designed to be g=30nm to introduce near-field coupling (Figure 2.2(b)).

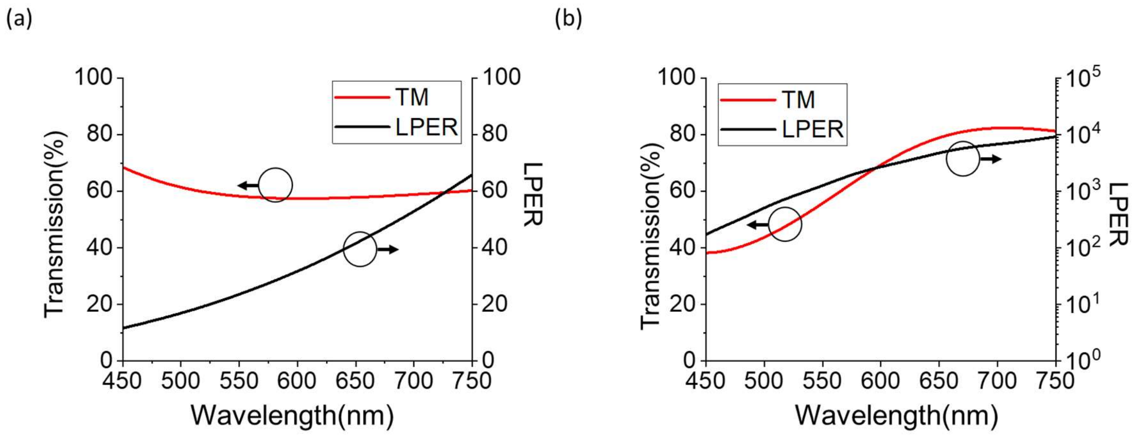

Figure 2.3: LPER and efficiency of single-layered gratings with different thicknesses. (a) Transmission efficiency and LPER of single-layered grating with Al deposition thickness of 80nm, which is the same as VCDG design. The period and duty cycle of Al grating are 190nm and 0.5. (b) Transmission efficiency and LPER of single-layered grating with Al thickness of 180nm, the period, duty cycle of Al gratings are 190nm and 0.5.

Figure 2.3 shows the LPER and efficiency of single-layered gratings with different Al deposition thicknesses. At the same thickness of 80nm, VCDG has 3 orders higher LPER than single layered gratings (Figure 2.3(a)); we contribute such high LPER of VCDG to its bi-layer nature, which allows transmitted electric field from top Al nanowire to be further damped out by the lower grating. Further, we increased the single grating thickness to 180nm to catch up with the LPER difference, as shown in Figure 2.3(b). However, such thick Al requires Al etching in fabrication, which is a challenging task because both etching uniformity and etching reproducibility needs to be optimized for millimeter-scale fabrication. On the contrary, the fabrication of VCDG does not require the etching of Al but Al deposition, which is much simpler and robust. Therefore, in general the advantage of VCDG over single layered gratings is it has high LPER thanks to its bi-layer nature and is much simpler in fabrication as it does not require the etching of metal.

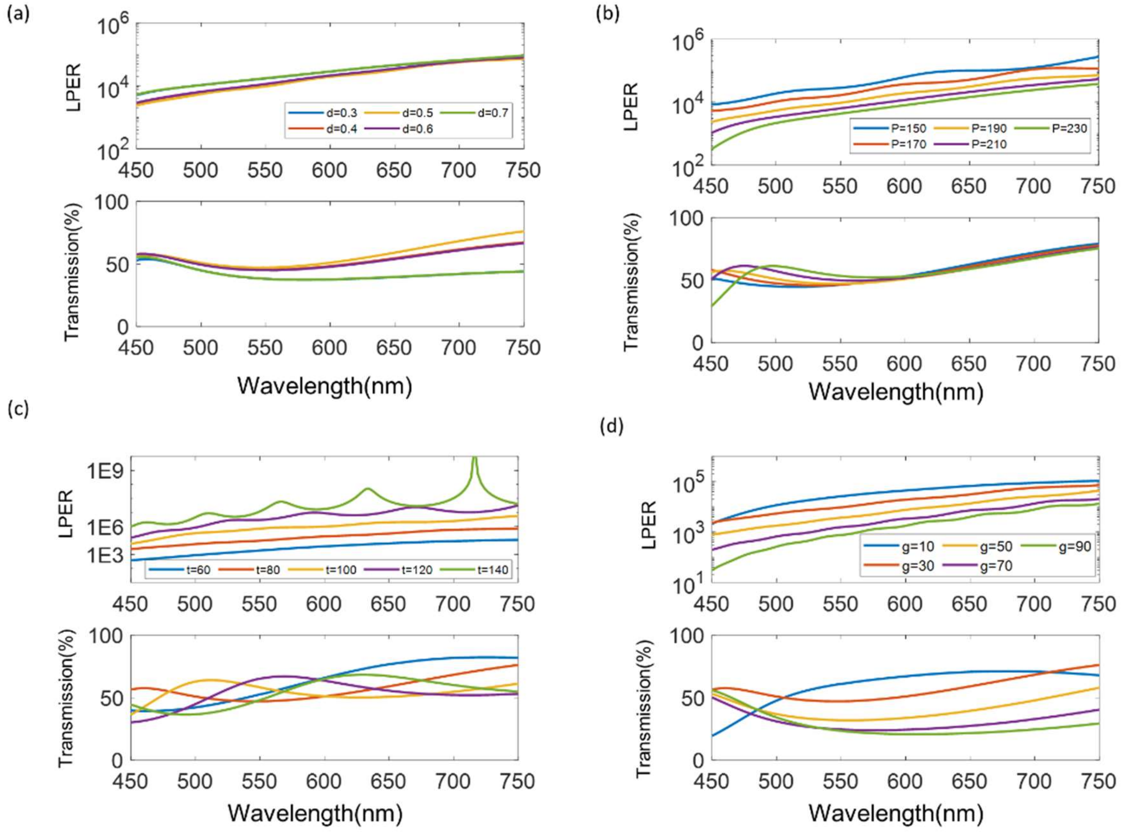

Figure 2.4: Parameter scan of VCDG's duty cycle d, period P, Aluminum thickness t, and vertical gap g. (a) Simulated transmission and LPER as a function of duty cycle written as d, here d is defined as the ratio between the width of elevated Al grating and VCDG period. Al thickness, vertical gap, and period are fixed to be 80nm, 30nm, and 190nm, respectively. (b) Simulated transmission and LPER as a function of VCDG period written as P. Al thickness, vertical gap, and the duty cycle is fixed to be 80nm, 30nm, 0.5, respectively. (c) Simulated transmission and LPER as a function of Aluminum thickness written as t. period, vertical gap, and the duty cycle are fixed to be 190nm, 30nm, and 0.5, respectively. (d) Simulated transmission and LPER as a function of vertical gap written as g. period, Aluminum thickness and duty cycle are fixed to be 190nm, 80nm, 0.5, respectively.

Figure 2.4 shows the parameter scan of VCDG optical performance in full wave simulation for design optimization. Here, the VCDG duty cycle was optimized to be 0.5 for maximum efficiency, (Figure 2.4(a)), the period and Al thickness was selected to be 190nm and 80nm, respectively, for sufficient efficiency at a shorter wavelength(<500nm) , as shown in Figure 2.4(b) and Figure 2.4(c).

Figure 2.4(d) Compared to the impact of vertical gap size to the optical performance of VCDG different. The transmission efficiency and LPER of VCDG increase significantly when g is decreased, this is because the vertical near-field coupling will gradually smear out as vertical gap g enlarges.

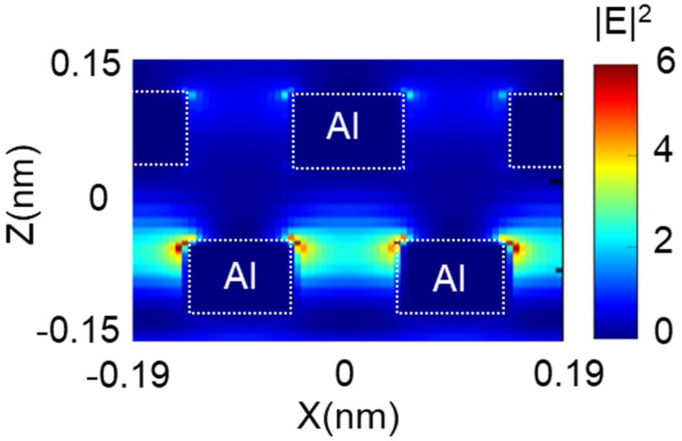

Figure 2.5: Near field distribution at 620nm for VCDG with a vertical gap of 90nm, Grating period is 190nm, Al thickness is 80nm with duty cycle 50%. In this case, there is no vertical coupling between the elevated grating and its bottom counter part due to too far a different distance.

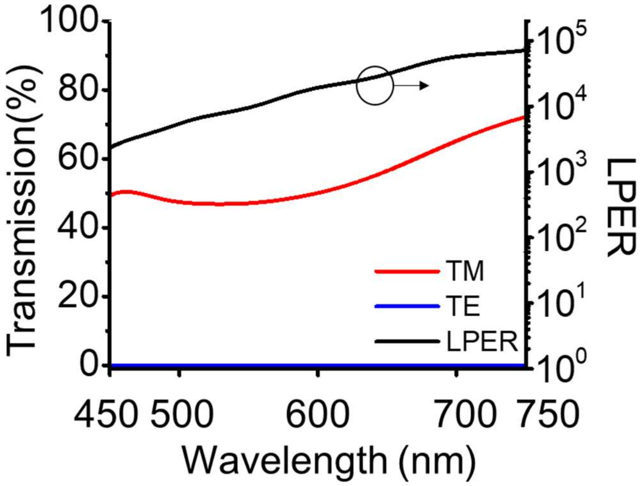

Figure 2.6: Transmission spectra and linear polarization extinction ratio (LPER) of VCDG under TE and TM polarization.

Figure 2.5 shows the near field of the VCDG at g=90nm, in which vertical near-field coupling smears out due to the too far separate distance. Overall, our designed VCDG has LPER over 1000 in the visible range with maximum efficiency of 55.8% and 46.5% at 650nm and 510nm, respectively, as shown in Figure 2.6.

2.4. Full Wave Simulations of Dual Wavelength Chiral Metasurfaces

We have demonstrated the metal-dielectric hybrid chiral metasurface concept at NIR in our previous work, which is composed of a top dielectric metasurface layer formed of Si nanopillar array and a bottom layer of Au nanowires[45]. In this work, we applied 1D subwavelength Si nanogratings (period 297nm, width 100nm, and height 130nm) as the dielectric metasurface layer to achieve multi-order QWPs with high efficiency and phase control at multi-operation bandwidth.

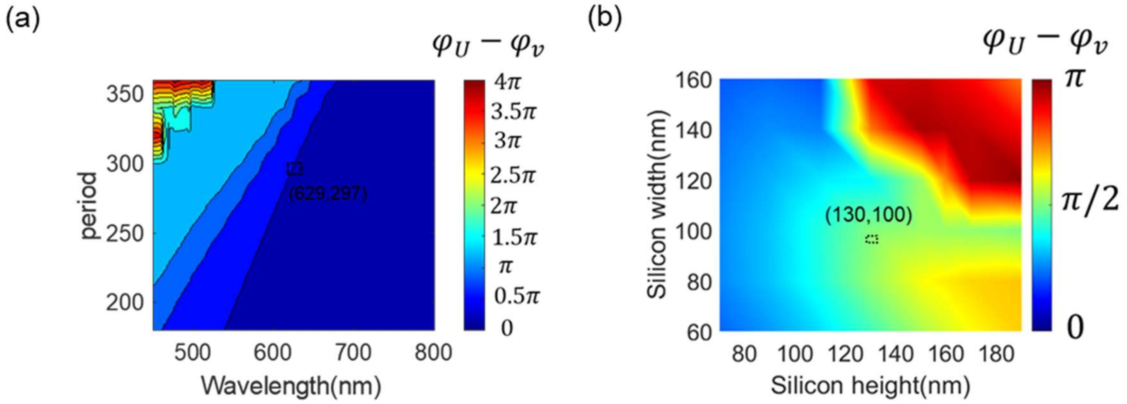

Figure 2.7: Full Wave simulation Optimization process for Si nanogratings. (a). Tuning working wavelength of Si nanogratings by chaging Si grating period, the duty cycle is fixed to be ~0.34 and the Si grating height is fixed to be 130nm in FDTD simulation. The contour line highlighted by black dashed circle corresponds to $\frac{\pi}{2}$ phase difference. (b). Tuning phase difference between U,V axes at 630nm by changing Si grating height and grating width. Si grating period is fixed at 297nm in FDTD simulation.

Figure 2.7 shows the optimization process for selecting period of Si nanogratings. The period of Si grating was selected to be 297nm to work at ~630nm as a high efficiency QWP. The duty cycle was selected to be 0.34 as this range provides large fabrication error toleration(±20nm) to achieve a QWP with retardance error < 5% from ideal. As for the bottom layer, we used VCDG with optimized dimensions (period 210nm, duty cycle 0.5, Al thickness 80nm, and vertical gap 30nm) for its high LPER and fabrication simplicity, as mentioned above.

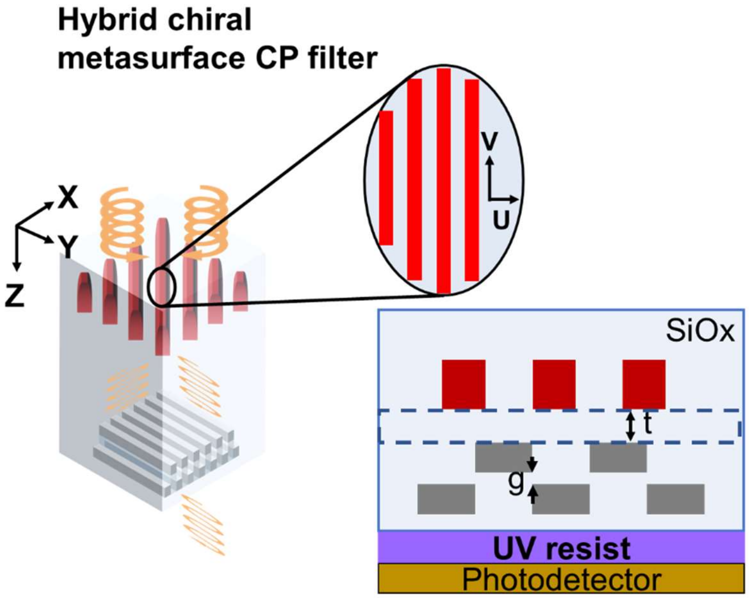

Figure 2.8: 2D cross-sectional illustration of the top layer Si nanograting and bottom layer VCDG, respectively. The thickness, period, width, and tilted angle of Si nanograting are tsi=130nm, pSi=297nm, and wSi=100nm. The thickness of Aluminum (Al), period, and vertical gap of bottom layer VCDG are tAl= 80nm, p2= 210nm, and g=30nm, respectively. The thickness of the SiOx spacer layer is t=400nm.

3D schematic and 2D cross-sectional illustration of the chiral metasurface is shown in Figure 2.8. Compared to Si nanopillars in our previous work[45], Si nanogratings introduce a bigger artificial birefringence Δn (written as $\Delta n = n_V - n_U$, where n_V , n_U are defined as the effective refractive index of Si nanogratings along grating length and width directions) because 1D sub-wavelength Si gratings have a larger filling factor of Si over 2D sub-wavelength Si nanopillar array, thus the required Si nanograting height-to-width aspect ratio (1.3) for $\frac{\pi}{2}$ phase difference engineering is much less than Si nanopillars.

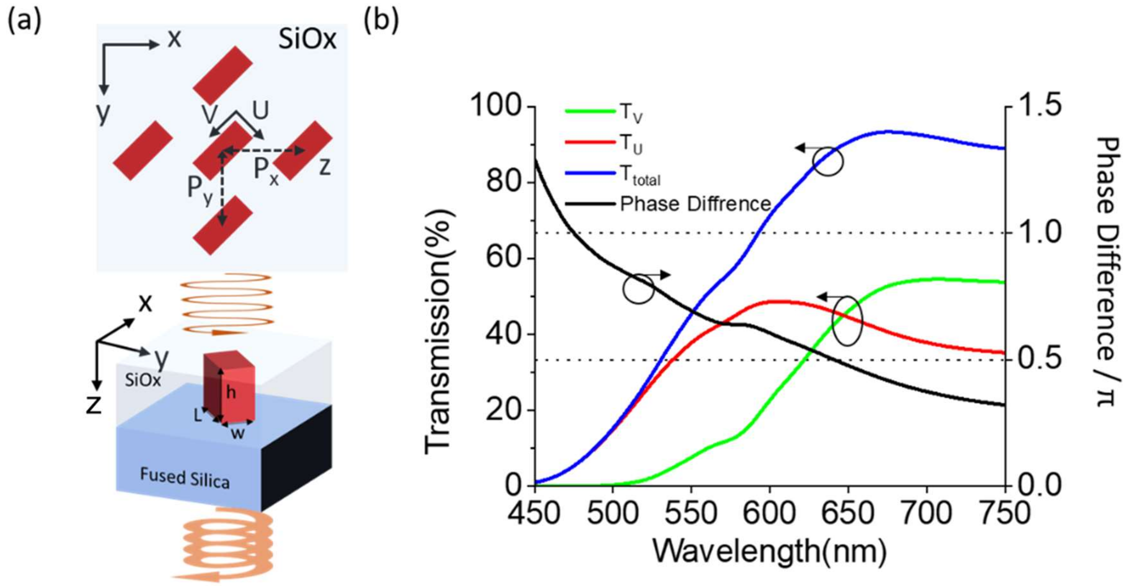

Figure 2.9: Optimized Si Bar nanopillars working as QWP at 645nm. (a) 2D illustration of Si nanobar array and 3D illustration of Si nanobarn unit cell. Si nanopillar is immersed in SiOx for on chip integration. The width w, length L and height h and period along x axis and y axis of Si nanopillar are w=60nm, L=250nm, h=260nm, Px=Py=190nm respectively.(b) Phase difference between fast axis(U axis) and slow axis (V aixs), left axis, and correspondent transmission along U axis(red) and V axis(green) and total transmission (black) (right axis).

An exemplar design for Si nanopillars optimized at 645nm is shown in Figure 2.9, where the aspect ratio is over 4. Such a low aspect ratio (1.3) of Si nanogratings makes it much easier to fabricate as it does not require a highly anisotropic etching of Si.

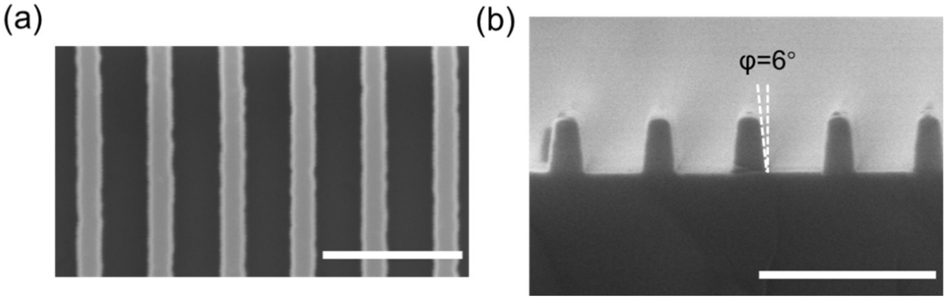

Figure 2.10: Top view and Cross-section SEM image of the dry etched Si gratings. (a) Top view SEM, scale bar: 500nm. (b) Cross-section SEM, scale bar: 500nm.

Images of fabricated Si nanogratings are shown in Figure 2.10. The etched Si nanograting has a slightly slanted sidewall due to a partially anisotropic dry-etching process; thus, a tilting angle of 6° is considered in the full wave simulation.

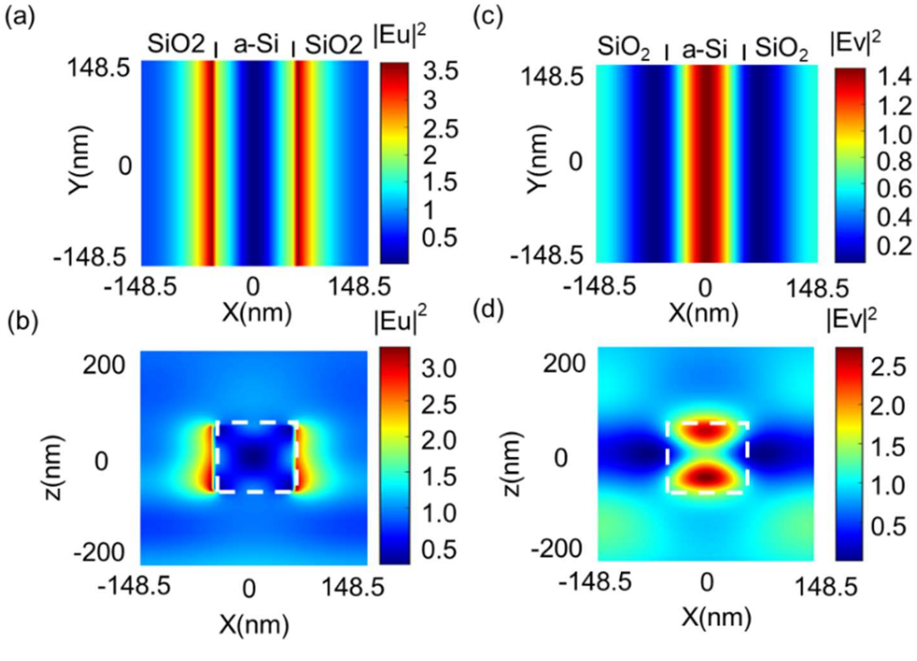

Figure 2.11: Near field distribution of the Si grating with incident polarization along the width of the Si nanogratings (U axis) and length of the Si nanogratings (V axis) at 629nm.

Like Si nanopillars, the artificial birefringence of multi-mode Si nanogratings stems from the anisotropic near-field distribution under different incident light polarization, as illustrated in Figure 2.11. When incident light is polarized along the fast axis (U axis), the Si grating works in leaky mode [52-54], and the electric field intensity is highly localized in SiO_x gaps between Si, as shown in Figure 2.11(a) and Figure 2.11(b). On the other hand, for incident light polarized along the slow axis (V axis), the Si nanogratings exhibit Febry Perot mode, and the electric field intensity is located inside Si, as shown in Figure 2.11(c) and Figure 2.11(d).

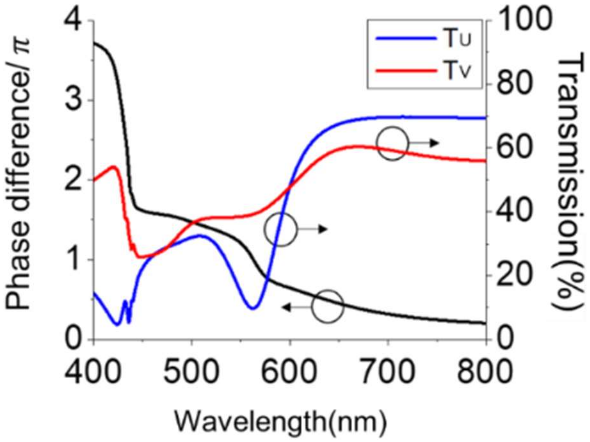

Figure 2.12: Phase difference between EU and EV calculated by FDTD simulation.

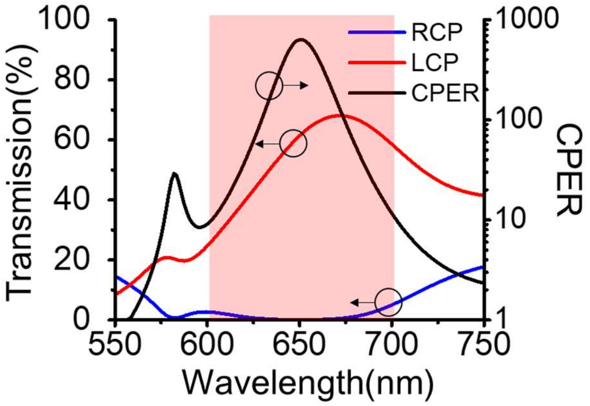

Figure 2.13: Finite difference time domain (FDTD) simulated transmission spectra(left) and circular polarization extinction ratio (CPER) (right) of dielectric-metal hybrid chiral metasurface at 550nm-750nm.

Subsequently, the phase difference between fast and slow axes was engineered to be $\frac{\pi}{2}$ at 629nm with a transmission difference of ~7% as shown in Figure 2.12.

Figure 2.13 shows the transmission spectra (left axis) and the CPER (right axis) of an LCP filter at 550~750nm. The device has a maximum CPER of over 600 with a transmission efficiency of 61.5% at 650nm. Moreover, the device design can operate from 600nm to 700nm with CPER over 10.

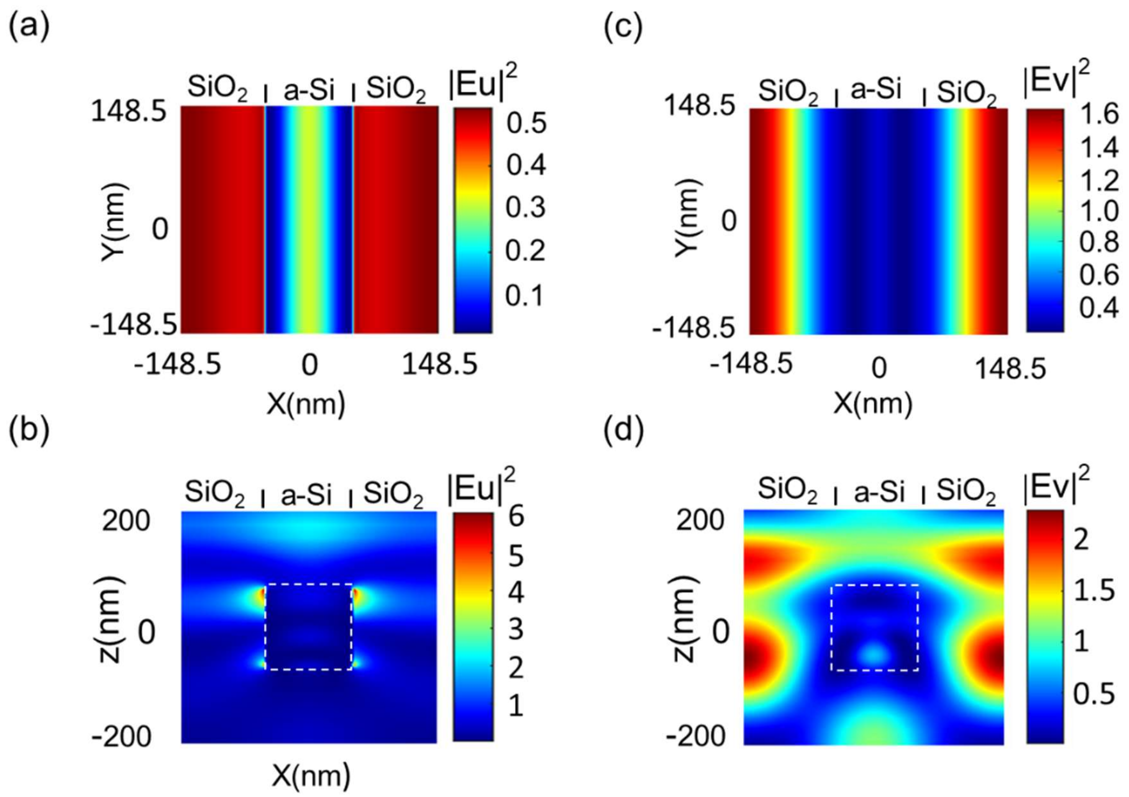

Figure 2.14: Near field distribution of the Si grating with incident polarization along the U and V axes at 500nm.

Meanwhile, Si nanograting has another mode functioning as QWP at a shorter wavelength centered around 500nm, mainly due to its highly dispersive near-field distribution, as shown in Figure 2.14. This leads to an advanced phase $\frac{3}{2}\pi$ along the fast axis, while their electric field transmission coefficient difference is less than 4% (Figure 2.12).

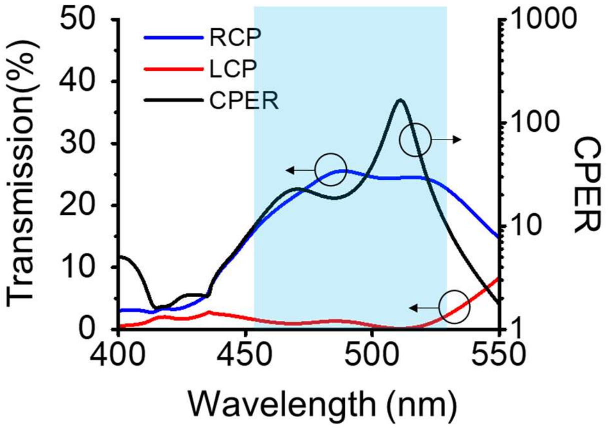

Figure 2.15: FDTD simulated transmission spectra(left) and CPER (right) of dielectric-metal hybrid chiral metasurface at 400nm-550nm.

As a result, the chiral metasurface detects opposite CP handedness at a shorter wavelength, as shown in Figure 2.15. The chiral metasurface exhibits a maximum CPER of 170 with a transmission efficiency of 24.5% at 510nm and 450nm to 525nm with CPER over 10. The dual working wavelength of Si nanograting broadened the operation wavelength range, which is another unique advantage over Si nanopillars reported in our previous work. In total, our design has an operation bandwidth of 175nm(CPER>10), which is one order higher than other grating diffraction-based designs[37, 38].

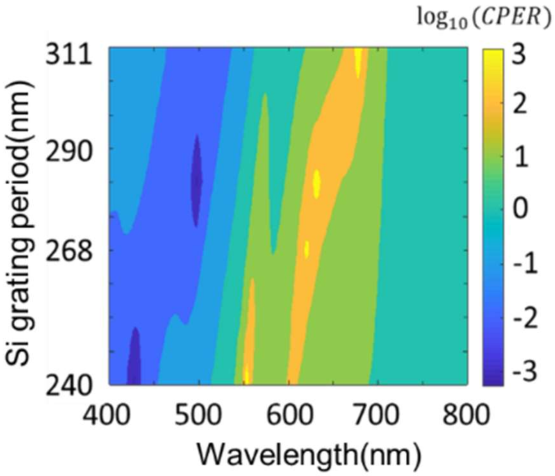

Figure 2.16: Device CPER Parameter scan as a function of Si nanograting period, the CPER is defined as the transmitted intensity of LCP divided by the transmitted intensity of RCP.

The parameter scan of CPER as a function of the grating period is shown in Figure 2.16. It is possible to cover an even broader wavelength range by setting pairs of chiral metasurfaces with different Si grating periods, as the working wavelength gets red-shifted when increasing the Si nanograting period.

2.5. Conclusion and Discussion

In this chapter, we presented a dual-wavelength chiral metasurface design based on the metal-dielectric hybrid concept. Si nanogratings are adopted as dielectric layers due to their advantages in simpler fabrication feasibility compared to our previous work. The device design demonstrated shows dual working wavelength with CPER over 10 (450nm to 525nm and 600nm to 700nm). It shows high efficiency at red color (>60%) thanks to low loss of Si in visible. The device has a subwavelength dimension and has compatibility with on chip integrated, enabling compact polarimetric imaging sensors for various polarization imaging applications.

CHAPTER 3

CHIP-INTEGRATED FULL-STOKES POLARIMETRIC CMOS IMAGIN SENSOR

In this chapter, we report a Metasurface-based Chip-integrated Full-Stokes Polarimetric CMOS Imaging sensor (MCFPI) with a dual-wavelength operation (630-670nm and 480nm-520nm). Calibration and characterization of our device are demonstrated, whereby high polarization states measurement accuracy (measurement error <4%) at incidence angle up to ±20° and full Stokes polarization images of polarized objects is shown. Our proposed device is ultra-compact and compatible with CMOS fabrication, promising various applications in remote sensing, industry surveillance, and biomedical imaging.

3.1. Introduction

Conventional polarization imaging systems require complex optical components and moving parts, making system miniaturization difficult [16, 17, 55]. Moreover, these systems also suffer from reduced frame rates and inaccurate extracted polarization information due to motion in the scene. Monolithic integrated polarimetric imaging systems have been studied by quite a few groups [56-59]. In these systems, silicon (Si) photodetectors and micro polarization filters are integrated on the same substrate, and the incoming light is filtered with spatially distributed microscale polarization filters in front of the imaging pixels. All of them adopt spatial division measurement schemes to avoid moving parts, making on-chip integration much easier and more reliable. Such a spatial division measurement approach requires 4 to 6 different polarization filters, including linear and circular polarizations, to measure the polarization state of light at one site. Various types of polarization filters have been applied, including liquid crystal polymers [20, 34], birefringent polymers [60, 61], metallic nanowires [21, 62], and micro retarders on metallic nanowires[18]. However, the applications of these polarimetric imaging systems are hindered by various limitations. The thin-film structures (for example, Liquid crystal[63] and silica films[64]) usually require fabrication techniques that are not compatible with CMOS technology. Their extinction ratios are also not high enough. Some of them are based on organic materials, such as liquid crystal polymer[63] and organic chiral dyes[65], which has stability issues. Moreover, the array size is quite limited, and the crosstalk issue is severe due to the thick film thickness and large distance from the underlying imager array. The method based on metallic nanowires [21, 66, 67]exhibits a high extinction ratio (>50) and subwavelength thickness and is compatible with CMOS technology; however, they can only measure the linearly polarized light but not the circularly polarized light (CPL), i.e. to determine DOCP and S_3.

In this chapter, for the first time, we report a chip-integrated full Stokes polarimetric CMOS imaging sensor based on sub-wavelength scale metasurface polarization filter array (MPFA) with the dual-wavelength operation, i.e., 630-670nm and 480-520 nm (red and cyan) and high measurement accuracy at acceptance angle up to ±20°. (Stokes parameter measurement error <2% for red and cyan at normal incidence and <4% for red at ±20°). The optical performance, such as measurement accuracy, sensor compactness, operation wavelength range, and operation angle range between our full Stokes polarization imaging sensor with state-of-the-art full Stokes polarization imagers based on metasurfaces, are shown in table 3.1. Table 3.2 presents a comparison between our polarization imaging sensor with other polarization imaging technology not based on metasurfaces.

In general, the advantage of our device can be summarized in three folds: First, the nanofabrication process of our metasurfaces is compatible with traditional CMOS fabrication techniques. To the best of our knowledge, our device is the first metasurface design directly integrated into a CMOS imaging sensor, providing ultra-compact full Stokes polarization imaging at a single snapshot. Second, our device has dual operation wavelengths because of multi-mode Si nanograting, as discussed in detail in chapter 2. Third, we achieved high accuracy in full Stokes parameter detection at an acceptance angle of up to ±20° via a simple snapshot. This is achieved by calibrating the device before the measurement using the instrument matrix method [68]. With advantages in ultra-compactness, dual operating wavelengths, high detection accuracy at acceptance angle up to ±20°, and feasibility in nanofabrication at different scales, our device is ideal for ultra-compact polarization imaging systems, promising applications in biomedical imaging, industrial imaging, and remote sensing, etc.

Table 3. 1. Full Stokes polarimetric imagers based on metasurface structures.

Full Stokes polarimeters	materials	Chip integrated?	Detection error	FOV	Bandwidth	Pixel Number of polarization images
Our work	Dielectric-metal hybrid	Yes	<2% (S1,S2,S3)	Up to 40°	Dual color 630-670nm(red) 480-520nm(cyan)	335×224
Dielectric metasurface diffraction grating	Dielectric	No (requires spacing to diffract incoming light)	Polarization contrast error < 10%[1]	10°[1]	Narrow band 527 to 537nm[1]	3M
Microscale polarization metalens array		No (requires spacing for focus)	averaged relative error <4.85% (S1,S2,S3)[2]	normal incidence	Narrow band 1550 nm[2]	5×10 [2]
Microscale polarization metalens splitter array		No (requires spacing for focus)	7.5-15%(S1,S2,S3)[3]	normal incidence	Narrow band 845-855nm[3]	70×46 [3]
Plasmonic metasurface microscale polarization filter array	Plasmonic	No (requires relay lens)	<6%(S1), <8% (S2), < 7%(S3)[4]	normal incidence	Broadband 4~9 μm[4]	30×25

Table 3. 2. Comparison with State-of-the-art polarization imaging sensors

Full Stokes polarization imagers	Detection error	Angle demonstrated	Operational wavelength	Compactness	Type	Full Stokes
Our Work	<2%(S1,S2,S3), DOLP<1.5%, DOCP<2% AOP<0.8° at normal incidence <4%(S1,S2,S3) DOLP<2.28% DOCP<4%, AOP<0.9° at ±20° incidence (red color)	40° for red 10° for cyan	630-670nm(red) 480-520nm(cyan)	Subwavelength, No gaps between CMOS and MPFA	Division of focal plane (DoFP)	Yes
Rotational Liquid Cystal and a fixed linear polarizer	Elliptical polarization: DOCP error< 2% DOLP error<3%[16]	NA	520-550nm	mm~cm scale	Division of time (DoT)	Yes
Metallic wire-grid LP filters	LPER = 80~450[19]	45°	400-900nm	Subwavelength, No gaps between CMOS and MPFA	Division of focal plane (DoFP)	No
Birefringent polymer integrated on micro LP filters array	full Stokes image of LCD screen: DOCP error <6.7% DOLP error < 3.35% AOP error < 1.90°[18]	f/2 ~f/8	400-700nm	~2μm for Microretarder ≥3.45 μm gap exists due to retarder substrate stress	Division of focal plane (DoFP)	Yes
Liquid crystal polymer based DoFP polarimeter	full Stokes image of retarders at different angle: DOCP error: 2%~ 25% DOLP error:1%~18% [20]	f/5.6	577.5-582.5nm	N.A. for Microretarder 76 μm residual gaps between device and imaging sensor	Division of focal plane (DoFP)	Yes

3.2. Design Concept of Chip Integrated Full Stokes Polarization Imager

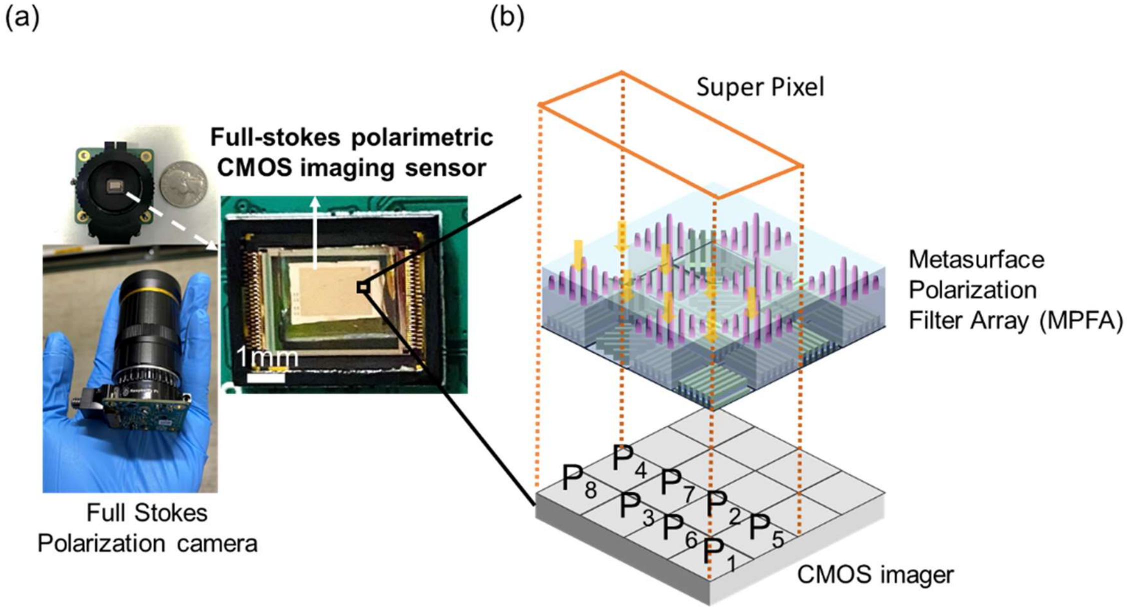

Figure 3.1: Chip-integrated full-Stokes CMOS polarization imager with dual operation wavelength. (a). Image of full Stokes polarization imaging sensor besides a U.S. dollar coin. (top left), image of polarization imaging sensor assembled with a zoom lens held on a palm(bottom), the image of zoomed-in full Stokes polarization imaging sensor. (b). Image of full Stokes polarimetric CMOS imaging sensor (b) 3D Conceptual illustration of MCFPIs. Here P1-P4 denotes the LP filters with transmission axes at 0° 90° 45° 135°, respectively. P5 and P6 denote chiral metasurface filters transmitting right-handed circularly polarized (RCP) and left-handed circularly polarized (LCP), respectively.

The design of MCFPIs is based on the space division measurement approach [56-59]. The polarimetric imaging sensor, as shown in Figure 3.1(a) and Figure 3.1(b), comprises an MPFA and a commercial CMOS imaging sensor beneath it. The sensor consists of over 9400 super-pixels, and each super-pixel has two pairs of circularly polarized light (CPL) filters, P_5, P_7 are identical and is designed for transmitting LCP, and P_6 ,P_8 are designed for transmitting RCP. Each super-pixel also contains four linear polarization (LP) filters (P_1 to P_4) and each polarization filter is defined as one pixel.

3.3. Device Fabrication and Characterization

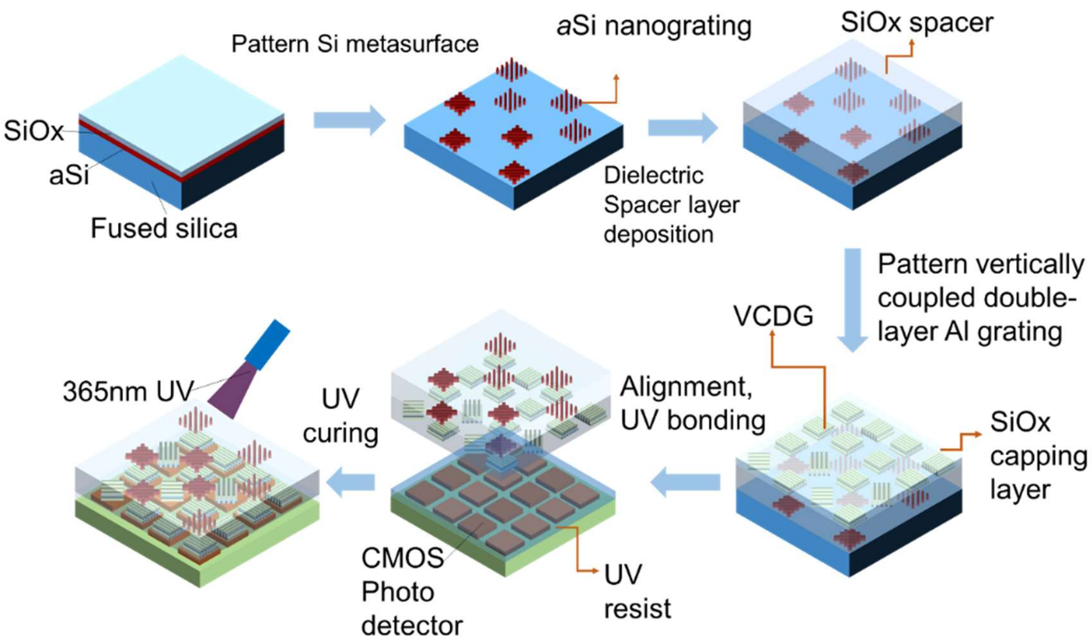

Figure 3.2: 3D illustrated schematic of the fabrication process for MPFA and on-chip-integration with CMOS imaging sensor.

Figure 3.2 shows the fabrication procedures for MPFA. First, amorphous silicon (*a*-Si) and SiOx were deposited onto fused silica wafers by plasma-enhanced chemical vapor deposition (PECVD), followed by electron-beam lithography (EBL), lift-off, reactive-ion etching (RIE) of SiOx mask, and inductively coupled plasma etching (ICP) of *a*-Si to form Si nanogratings. Then, a dielectric spacer layer (520nm) of SiO_x was sputtered onto Si nanogratings, followed by alignment and the 2nd layer of EBL to pattern nanogratings. After lift-off, the SiO_x spacer layer was etched down 110nm by reactive-ion etching (RIE), followed by 80nm Aluminum (Al) deposition by electron beam evaporation to form VCDG. Finally, the fabricated MPFA was deposited with 200nm SiOx as the capping layer. Then the device was cut into a 6mm*5mm large wafer piece using a wafer dicing saw, then the device was bonded onto the CMOS imaging sensor (Sony IMX 477) using a homemade UV bonding setup.

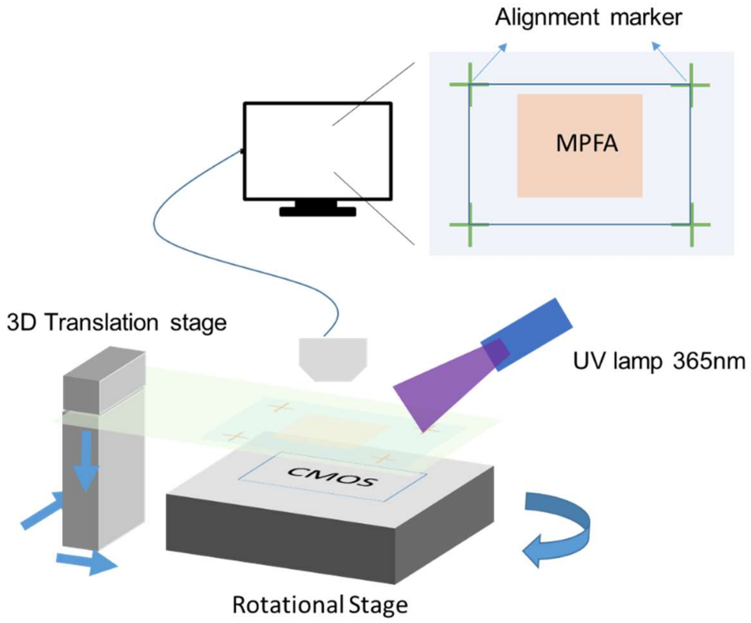

Figure 3.3: Homemade CMOS bonding setup for aligning and bonding the MPFA onto the CMOS imaging sensor.

The schematic of the UV bonding setup is shown in Figure 3.3. The device is taped onto a glass slide and then mounted on a 3D translation stage. Meanwhile, the CMOS imaging sensor is spin-coated with UV resist and mounted onto the rotational stage. Then the device is visually aligned to the CMOS imaging sensor using a pre-designed alignment marker. After alignment, the device is bonded to the CMOS imaging sensor via UV bonding.

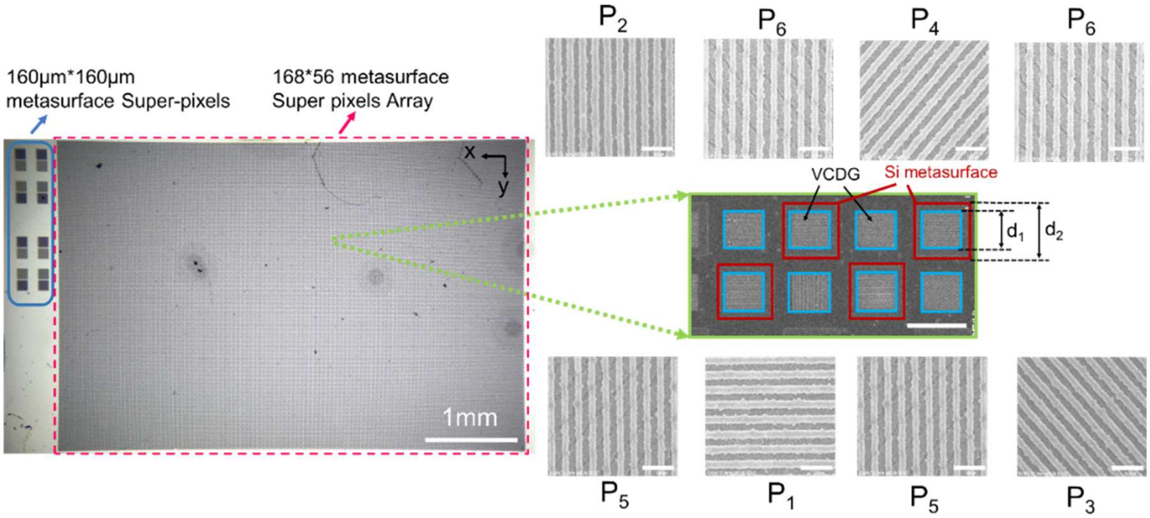

Figure 3.4: The microscopic photograph(left) and the SEM image of one super pixel among the fabricated MPFA (right), scale bar:10μm. 90°,45°,0°,135° LCP, and RCP on each sub-figure indicate the polarization state each metasurface filter transmits. Scale bar: 500nm (white). The length and width of the CP filter is d1Xd1 = 9.3μmX9.3μm, The length, and width of the LP filter are d2Xd2 = 6.2μmX6.2μm, the spacing between each LP filter is 4.65μm along both x and y direction.

Figure 3.4 shows a microscopic photograph of the fabricated MPFA. MPFA is 3.654mm wide and 2.434mm long. In total, we fabricated 336×384 microscale metasurface polarization filters. Besides the microscopic photograph, the break-in images are the scanning electron microscope (SEM) images that show detailed dimensions of eight metasurface units in one super-pixel.

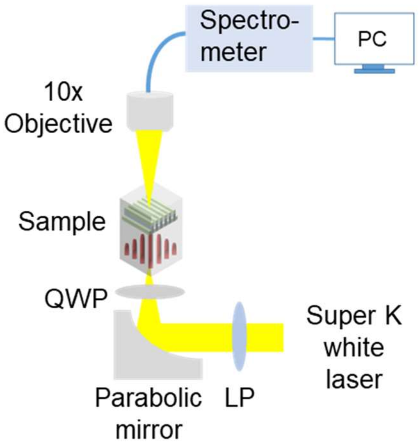

Figure 3.5: Schematic of the spectroscopy setup for chiral metasurface and VCDG characterization.

The performance of fabricated MPFA was first characterized by a visible spectrometer, as shown in Figure 3.5. the unpolarized laser was first polarized by linear polarizer (WP25M-UB by Thorlabs, Inc.) and super achromatic QWP (SAQWP05M-700 by Thorlabs, Inc.) to generate LCP, and RCP input, respectively. The CP light is then focused onto the sample with a focal spot size of 15um in diameter. The transmission efficiency was then measured using Olympus BX53 fluorescent microscope and Horiba iHR320 visible spectrometer. The CPER of LCP chiral metasurface was calculated using the formula:$E = T_{LCP}/T_{RCP}$, where T_{LCP} ,T_{RCP} denotes the transmission efficiency of LCP and RCP input, respectively. As for double-layer gratings, the transmission efficiency of s-polarized and p-polarized input was measured respectively to calculate LPER.

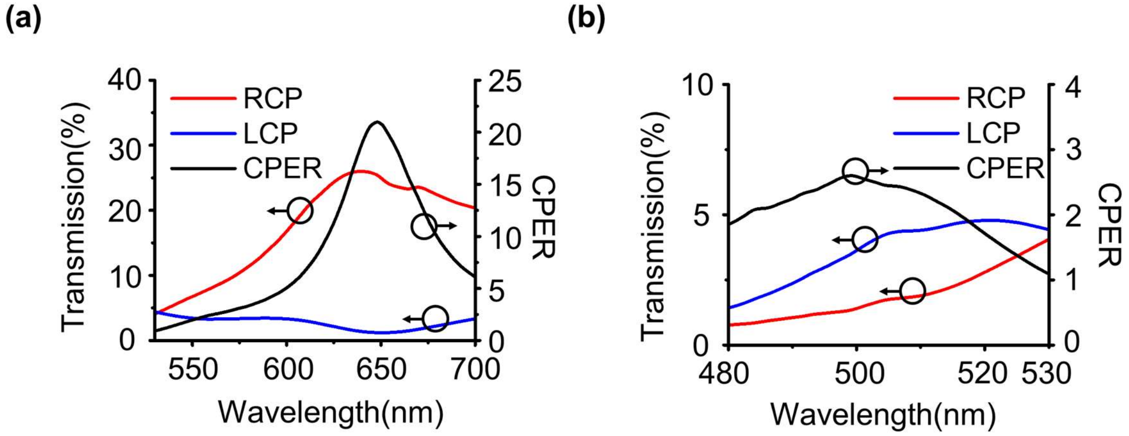

Figure 3.6: Transmission and extinction ratio characterization results of chiral metasurface and VCDGs. (a, b) Measured transmission and CPER of the chiral metasurface at 480nm-530nm and 530-700nm, respectively. Legend RCP, LCP indicates the input CP handedness (c). Measured transmission and LPER of fabricated VCDG under TM and TE polarization.

Figure 3.6(a) shows the measured circular dichroism (CD) spectra of a right-handed chiral metasurface (RCM). The RCM device has a transmission efficiency of 23% and CPER over 23 around 650nm. The RCM device provides CPERs of more than ten over a wavelength range of 60nm around operation wavelength 650nm. Figure 3.6(b) shows the measured circular dichroism (CD) spectra of the same device at a shorter wavelength. As expected in the design, the RCM device is converted into a left-handed chiral metasurface (LCM) device at a lower wavelength, which exhibits a transmission efficiency of 4% and CPER of ~2.5 at 500nm.

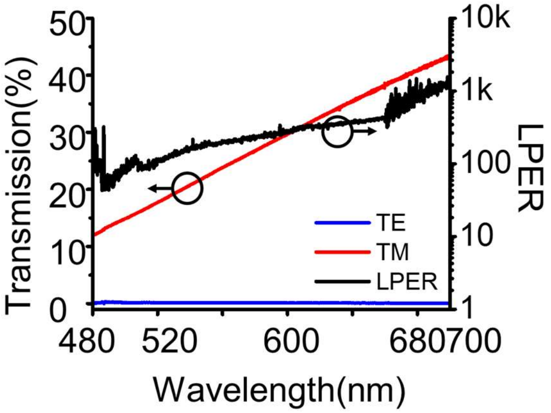

Figure 3.7: Measured transmission and LPER of fabricated VCDG under TM and TE polarization.

Figure 3.7 shows the measured transmission spectra of the VCDG (oriented at 0°) patterned on the SiOx spacer layer without the Si metasurface buried underneath, which shows an efficiency of 35% and LPER over 400 around 650nm. Noticeably the VCDG provides LPERs over 100 from 520nm to 700nm, offering broadband LP detection with high accuracy.

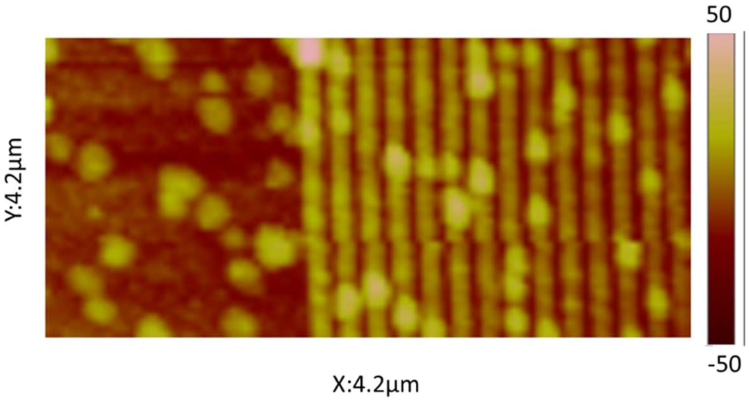

Figure 3.8: AFM image of VCDG before Al deposition. Surface roughness Ra=8.43nm at blank regions.

Two major aspects in fabrication contribute to the degradation of the transmission efficiency and LPER of fabricated VCDG compared to its original design: Firstly, the Al deposited by electron beam evaporation has significant edge roughness due to the large Al grain size as deposited, which introduces substantial optical loss due to scattering, thereby reducing LPER and efficiency of VCDG. Secondly, the sputtered SiOx spacer layer introduced surface roughness in the substrate (Ra=8.43nm, as shown in Figure 3.8); large SiOx grains modified the surface morphology of VCDG, especially vertical gap at certain locations, which reduces the LPER and efficiency of VCDG.

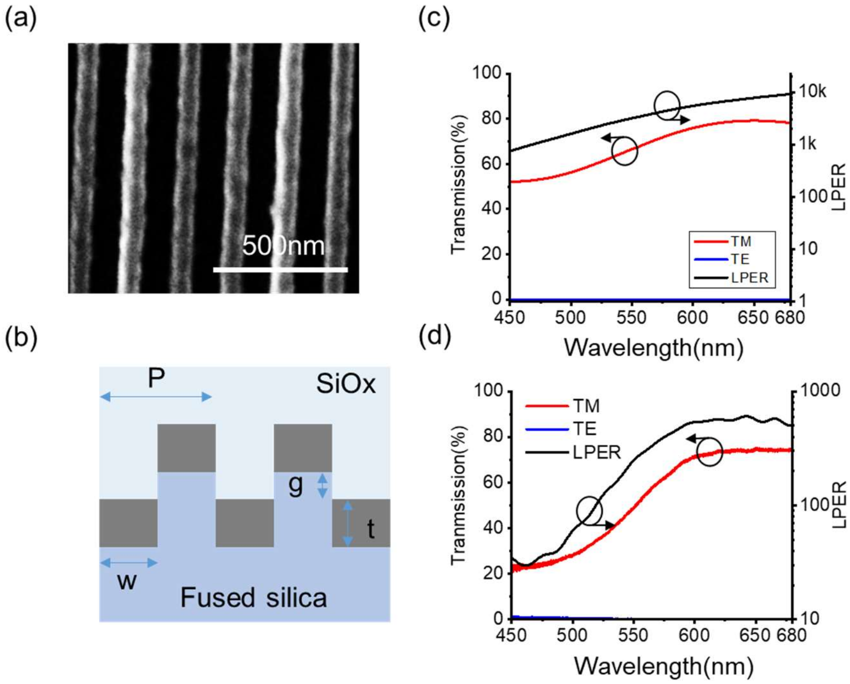

Figure 3.9: SEM image and characterization of VCDG fabricated by EBL patterning on fused silica wafer. (a) SEM image of VCDG, after taking SEM images, 200nm SiOx is sputtered as encapsulation layer on device. (b)2D cross sectional illustration of VCDG fabricated, the period, thickness of Al, vertical gap size and grating width are P=180nm,

t=60nm, g=20nm, and w=88nm, respectively. (c) Simulated transmission and LPER of VCDG. (d) Measured transmission and LPER of VCDG.

As a comparison, we fabricated VCDG on a fused silica wafer with similar dimensions by EBL patterning followed by Al E-beam evaporation. We increased the Al deposition rate and vacuum level to improve Al deposition quality. The resultant VCDG shows improved Al edge roughness (as shown by the SEM image in Figure 3.9(a)). In addition, it has a much higher efficiency (Figure 3.9(b)) than the current device, which is only 5% less than the maximum efficiency in FDTD simulation (Figure 3.9(d)). Therefore, increasing the optical performance of our VCDG is possible by improving Al deposition quality and SiOx sputtering quality.

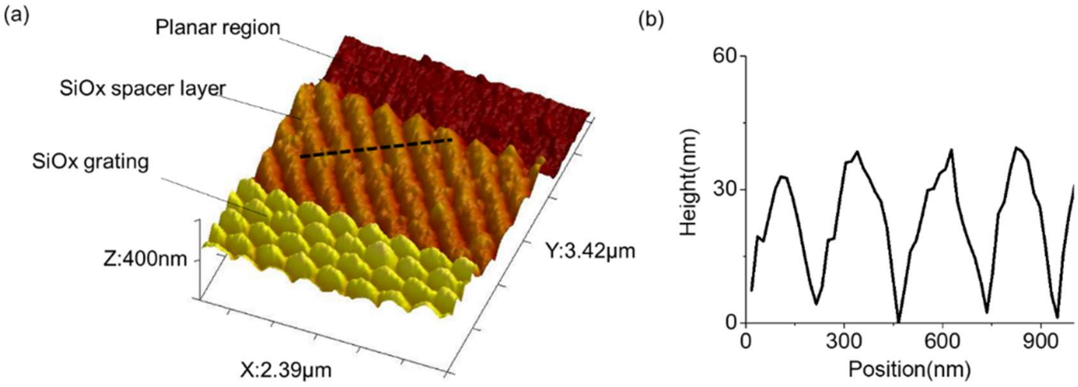

Figure 3.10: Fabrication of chiral metasurface. (a). Atomic Force Microscope (AFM) 3D image of SiOx spacer layer and SiOx grating after 2nd EBL patterning followed by dry etching of 100nm SiOx to form SiOx grating. (b) Height variation of SiOx spacer layer after SiOx etching, indicating surface roughness of SiOx spacer layer (Ra= 27.8nm).

On the other hand, the reduced optical performance of the chiral metasurface is also due to the surface roughness (Ra = 28.3 nm, as shown in the AFM image of Figure 3.10) of the SiOx spacer layer. Si nanogratings buried under the spacer layer leave a bumpy surface morphology for VCDG, leading to a significant decrease in LPER and thereby reducing the CPER of the chiral metasurface.

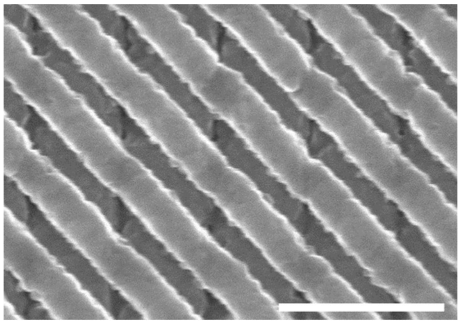

Figure 3.11: SEM of another chiral metasurface (Device B) fabricated by the same fabrication procedures. Scale bar: 500nm. The thickness, period, width, and tilted angle of Si nanograting are tsi=130nm, p1=268nm, and w=100nm. The thickness of Aluminum (Al), period, and vertical gap of bottom layer VCDG are tAl= 60nm, p2= 190nm, and g=20nm, respectively. The thickness of the SiOx spacer layer is t=335nm measured by Atomic Force Microscope (AFM).

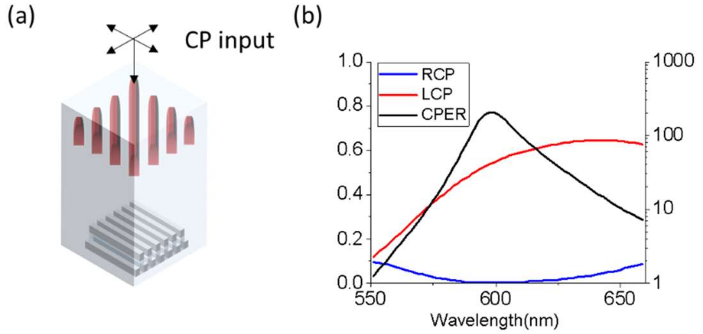

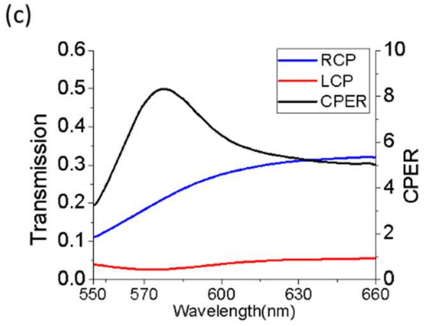

Figure 3.12: FDTD simulated and measured transmission/ CPER of chiral metasurface (device B) with CP light input from the Si grating side of the chiral metasurface. (a). 3D schematic to show CP input from the Si grating side of the chiral metasurface. (b). FDTD simulated CPER and efficiency of the chiral metasurface. (c). Measured CPER and efficiency of chiral metasurface (device B).

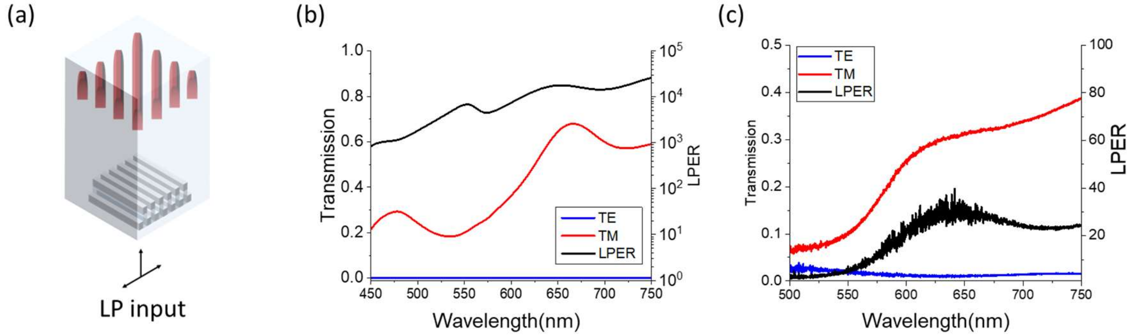

Figure 3.13: FDTD simulated and measured transmission/ LPER of VCDG with LP light incident from VCDG side of chiral metasurface (device B). (a). 3D schematic to show LP input from the VCDG side of the chiral metasurface. (b). FDTD simulated LPER and efficiency of chiral metasurface with LP input from VCDG side of chiral metasurface. (c). Measured LPER and efficiency of chiral metasurface with LP input from VCDG side of chiral metasurface.

To support our conclusion, we measured the LPER (Figure 3.13) of the bottom layer VCDG of a chiral metasurface (device B) with similar dimensions (Figure 3.11) together with its CPER (Figure 3.12), the CPER of device B is limited to only 8 at 580nm. In contrast, the LPER of the bottom layer VCDG is only ~15. This suggests that surface planarization of the dielectric spacer layer is required for the high optical performance of such a bi-layer dielectric-metal hybrid chiral metasurface design, which is what we plan to resolve at the next stage.

3.4. High Accuracy Polarimetric Detection

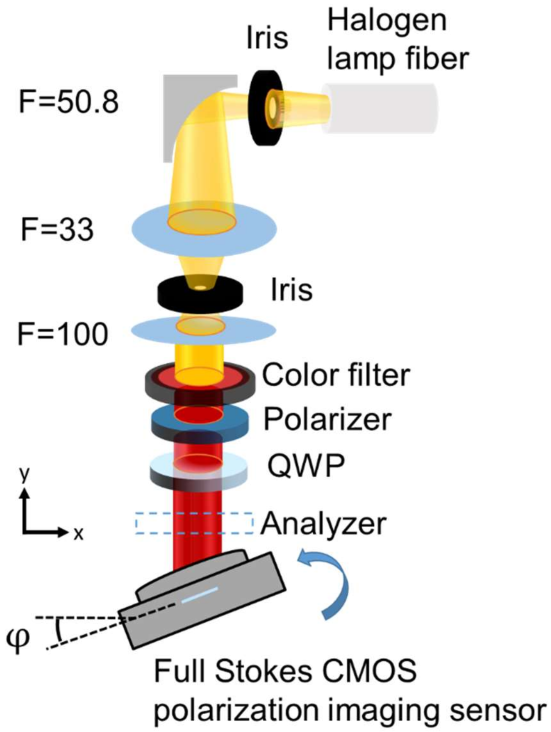

Figure 3.14: A schematic of the experimental setup, φ denotes the camera rotation in azimuth angle for oblique incidence measurement.

Traditionally, Stokes parameters are directly subtracted based on the intensity of 0°,90°,45°,135° LP, and RCP and LCP components of incoming light [69]. With this method, the accuracy is often constrained by the detectors' LPER and CPER [70]. Here, we first go through the calibration of the device by registering the instrument matrix A of MPFA, Stokes parameters S can be obtained after a snapshot of intensity I of MPFA using the equation: $S = A^{-1}I$. Such a calibration process can bypass the detection error introduced due to limited LPER and CPER as long as the calibrated instrument matrix is accurate. Therefore, this method can greatly increase polarization detection accuracy [41, 68].

Figure 3.14 shows a customized optical setup for calibrating the device. A color-filtered, uniform, collimated beam with sufficient spot size is incident onto the full Stokes polarization imaging sensor, which is mounted onto a rotational stage to control the light incidence angle φ. During the calibration, φ is kept at 0° (normal incidence) to register the instrument matrix. We apply a polarization state generator (polarizer and QWP) to generate arbitrary polarization states. With each polarization state input, a snapshot of the transmitted light intensity through MPFA was taken to obtain the intensity vector [68]. The instrument matrix A of MPFA could be readily obtained after sufficient polarization state input to form an intensity matrix.

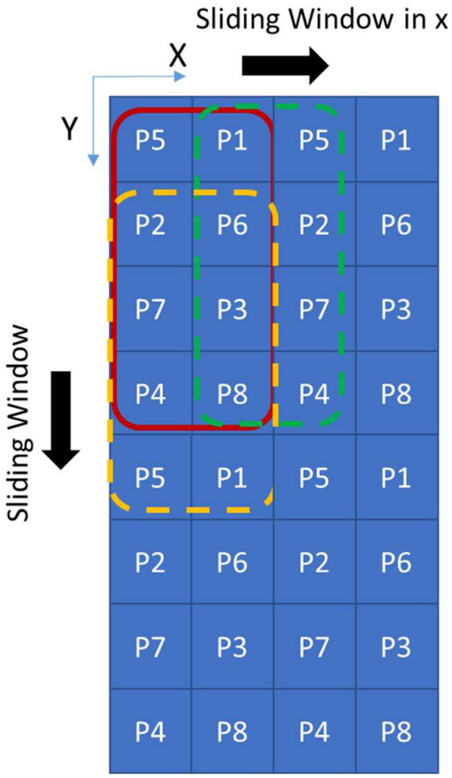

Figure 3.15: Illustration of the working principle of demosaicking during the instrument matrix calibration process.

To enhance the spatial imaging resolution, we also performed demosaicking during the instrument matrix calibration using a sliding window sampling approach. A new intensity vector can be obtained by sliding the superpixel registry window at both the x and y direction, 1 pixel per step, because of the periodic distribution of each pixel (P1-P8), as shown in Figure 3.15. Each newly registered super pixel has a complete set of LP filters and CP filters, a correspondent instrument matrix can thus be registered.

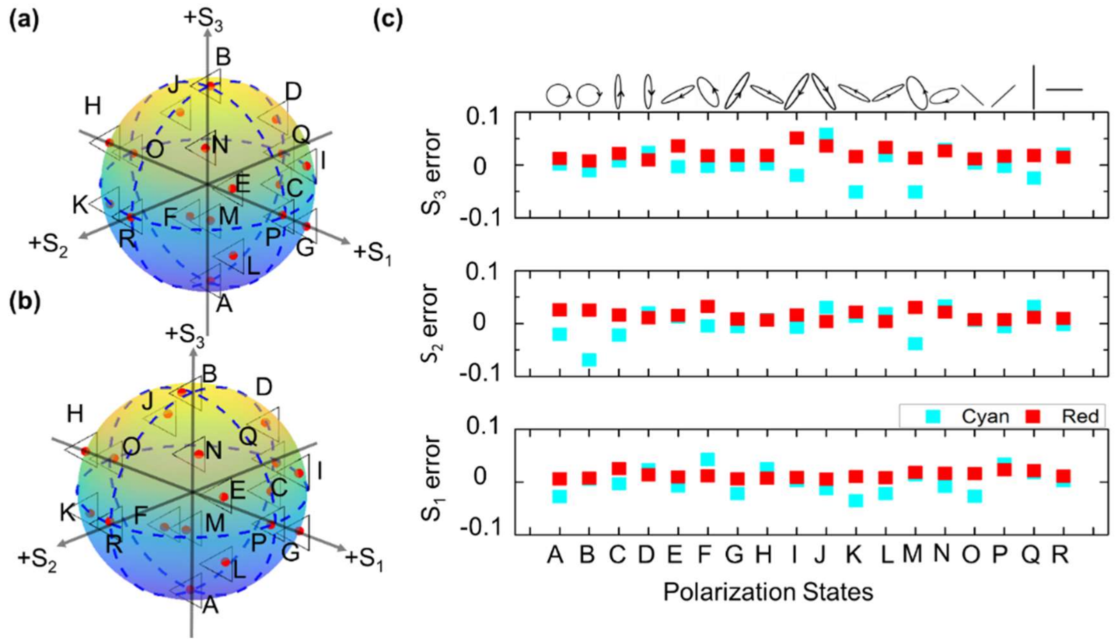

Figure 3.16: Full Stokes polarization detection of 18 arbitrary polarization states. (a,b) Illustration of measured polarization state (Red dot) and its input reference (Triangle) distribution on Poincare' sphere in red and cyan color, respectively. (c) Error distribution for Red/Cyan color full stokes parameter detection measurement result.

After calibration, we performed full-Stokes polarization detection on the same setup at different incidence angles, using the instrument matrix A calibrated at $\varphi = 0°$. We first treat our full Stokes imaging sensor as a single-point polarization detector to determine polarization detection accuracy. Figure 3.16(a,b) depicts the measured Stokes parameter S_i^j and their reference values ${S_R}_i^j$ measured by polarization state analyzer (PSA) (*i=1,2,3; j=* A,B… R) on the pointcaré sphere under red and cyan color input, respectively. In total, we chose 18 reference polarization states sparsely distributed in all eight quadrants of the pointcaré sphere to verify the full stokes polarimetric detection accuracy better. Here S_i^j is averaged out over the entire MPFA : $S_i^j = \frac{\sum_{a=1,b=1}^{n,p} S_{i\ a,b}^j / S_{0\ a,b}^j}{n \times P}$, i=1, 2, 3, j= 1,2… 18, n=335, p=221. where $S_{i\ a,b}^j / S_{0\ a,b}^j$ represents normalized Stokes parameters measured by each pixel. Figure 3.16(c) shows the measurement error ΔS_i^j for each polarization states at $\varphi = 0°$ under red and cyan colors. Here ΔS_i^j is defined as : $\Delta S_i^j = S_i^j - S_{R}{}_i^j$ (i=1, 2, 3, j=1,2… 18). The mean absolute error (MAE) $\frac{\sum_{j=1,}^{18} \left|\Delta S_i^j\right|}{18}$ (*i*=1,2,3) for S_1, S_2, S_3 are 1.84 %, 1.93 %, 1.79% for cyan and 1.03%, 1.43%, 1.99% for red, respectively.

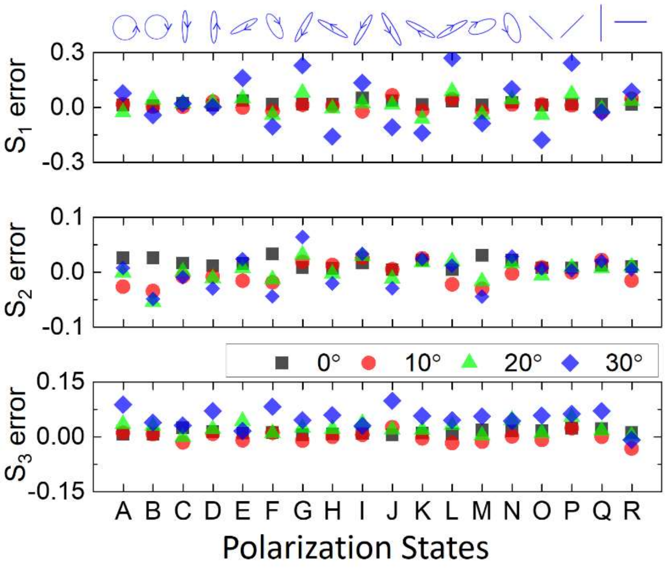

Figure 3.17: Full Stokes polarization measurement at different incidence angles, bandwidth 630-670nm.

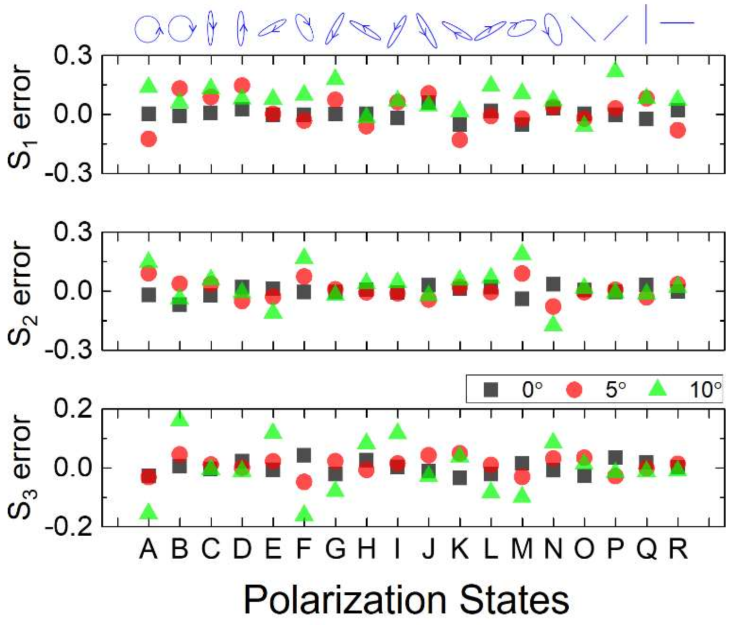

Figure 3.18: Full Stokes polarization measurement at different incidence angles, bandwidth 480-520nm.

Measured ΔS_i^j of other incidence angles are shown in Figure 3.17 for red and Figure 3.18 for cyan color. Based on the Stokes parameters measured, we calculated the angle of polarization (AOP=$\frac{1}{2}\arctan\frac{S_2}{S_1}$), degree of circular polarization (DOCP=S$_3$/S$_0$), and degree of linear polarization (DOLP=$\sqrt{S_1^2+S_2^2}/S_0$). Here σ_i is written as: $\sigma_i = \frac{\sum_j^{18}\sigma_i^j}{18}$ i=1,2,3, j=1,2…18 where σ_i^j is defined as the standard deviation of Stokes parameter measurement error of MPFA, denoted as: $\sigma_i^j = \sqrt{\frac{\sum_{a=1,b=1}^{n,p}\left(S_{i\,a,b}^{j}/S_{0\,a,b}^{j} - S_{R_i}^{j}\right)^2}{n\times p}}$.

Table 3. 3. Table of mean absolute error and average standard deviation for 18 polarization states at different incidence angle at red color input.

Red (630-670nm) MAE ± SD						
φ	***S_1/S_0***	***S_2/S_0***	***S_3/S_0***	***DOCP***	***AOP***	***DOLP***
0°	1.03%±0.84%	1.43%±0.77%	1.99%±0.88%	1.99%±0.88%	0.26°±0.28°	1.41%±0.72%
10°	2.02%±3.97%	1.57%±3.69%	2.78%±4.35%	2.78%±4.35%	0.63°±1.24°	1.71%±3.68%
20°	3.29%±3.88%	1.82%±3.85%	3.84%±4.72%	3.84%±4.72%	0.85°±1.23°	2.28%±3.80%
30°	9.99%±5.93%	5.19%±5.36%	17.51%±7.14%	17.51%±7.14%	3.07°±1.54°	6.41%±6.16%

Table 3. 4. Table of mean absolute error and average standard deviation for 18 polarization states at different incidence angle at cyan color input.

Cyan (480-520nm) MAE± SD						
φ	***S_1/S_0***	***$S2/S_0$***	***S_3/S_0***	***DOCP***	***AOP***	***DOLP***
0°	1.84%±0.85%	1.93%±0.76%	1.79%±2.38%	1.79%±2.38%	0.78°±0.25°	1.26%±0.79%
5°	1.88%±3.21%	2.03%±3.09%	4.44%±11.38%	4.44%±11.38%	0.85°±1.07°	1.04%±2.97%
10°	2.17%±3.54%	3.71%±3.49%	22.75%±15.39%	22.75%±15.39%	0.78°±1.15°	3.52%±3.34%

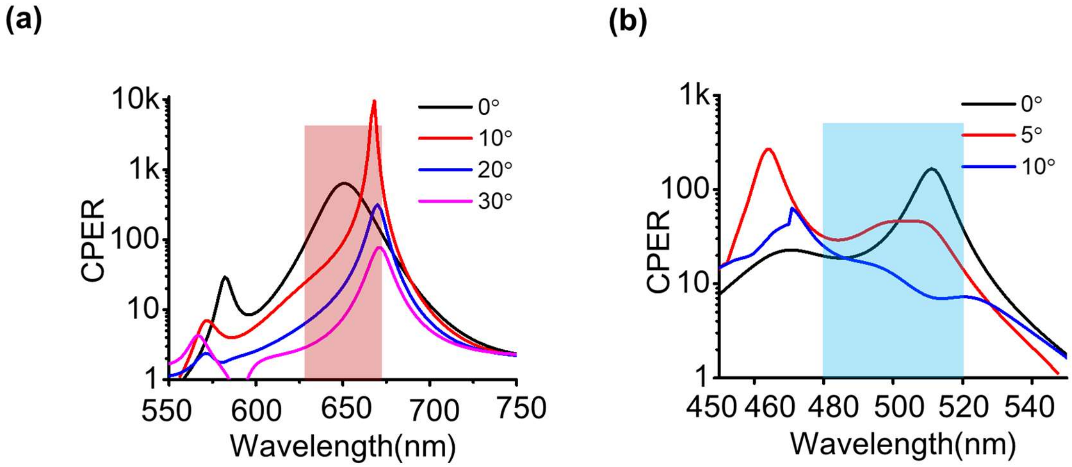

Figure 3.19: FDTD simulated CPER of chiral metasurface of under oblique incidence. (a,b).FDTD simulation at 550nm~750nm and 450nm~550nm respectively.

Measured MAE and averaged standard deviation σ_i for S_1, S_2, S_3, AOP, DOLP, and DOCP at different incidence angles are shown table 3.3 for red and table 3.4 for cyan color. MAE for AOP, DOLP, and DOCP is 0.26°,1.41%, 1.99% for red and 0.78°, 1.26%, 1.79% for cyan when $\varphi = 0°$. When φ is within ±20°, MAE for S_1, S_2, S_3 can maintain less than 4% for red. At ±30° incidence, MAE for S_3 increases to 17.51%, this is because CPER of chiral metasurface reduces by two orders compared to normal incidence, indicated by FDTD simulation (Figure 3.19(a)). Similarly, the device has an MAE of less than 4.1% for cyan color input with incidence angle within ±5°, with incidence angle up to ±10°, the detection error of S3 increases to 15% due to a decrease of CPER (Figure 3.19(b)).

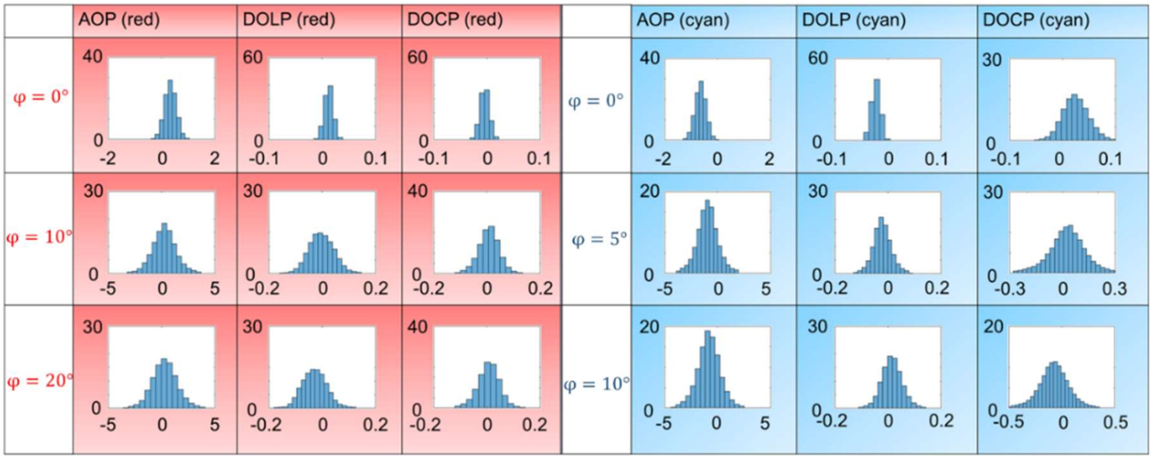

Figure 3.20: S_1, S_2, and S_3 detection error distribution of MPFA for polarization state D under red color, cyan color, and normal incidence and oblique incidence, respectively.

We then treat our full Stokes imaging sensor as a polarization beam profiler. In this case, the uniformity of polarization states measured by MPFA needs to be carefully evaluated to reflect the polarization imaging quality. Figure 3.20 shows the distribution of measurement error of AOP, DOCP, and DOLP for polarization state D at different incidence angles. Here we write them as $\Delta AOP_{a,b} = AOP_{a,b} - AOP_R$, $\Delta DOCP_{a,b} = DOCP_{a,b} - DOCP_R$, $\Delta DOLP_{a,b} = DOLP_{a,b} - DOLP_R$ (a=1,2…335, b=1,2…221) , where AOP_R , $DOCP_R$, $DOLP_R$ are reference values measured by PSA and $AOP_{a,b}$, $DOCP_{a,b}$, $DOLP_{a,b}$ are measured values from each pixel. Over 90% of $|\Delta DOLP_{a,b}|$,$|\Delta DOCP_{a,b}|$ and $|\Delta AOP_{a,b}|$are less than 0.04, 0.04, 0.5° respectively for both red and cyan color at normal incidence. A larger AOP, DOCP and DOLP error range can be seen when incidence angle increases. When φ is within ±20°, over 80% of $|\Delta DOLP_{a,b}|$,$|\Delta DOCP_{a,b}|$ and $|\Delta AOP_{a,b}|$ are less than 0.1, 0.1, 2°. The increase of the non-uniformity of measurement errors at oblique incidence is majorly due to instrument matrix is calibrated at φ=0°(normal incidence) , causing calibration errors when the imaging sensor is measuring polarization states in oblique incidence as MPFA has different CPER upon oblique incidence(Figure 3.19). Measurement error distribution of other polarization states under the red/cyan input can be found in Appendix B.

So far, we have shown that with the instrument matrix method, our full Stokes polarization imager allows highly accurate polarization state detection at red and cyan colors with a single snapshot. Moreover, we have shown that the instrument matrix method can be applied to an array of micro polarization filters with a standard deviation of less than 1% for both red and cyan color under normal incidence and are less than 5% for red color within ±20° oblique incidence. Our polarization imager, together with the instrument matrix reconstruction method, has the potential to achieve high accuracy full stokes parameter imaging with dual-wavelength coverage.

3.5. Dual-Wavelength Full-Stokes Parameter Imaging

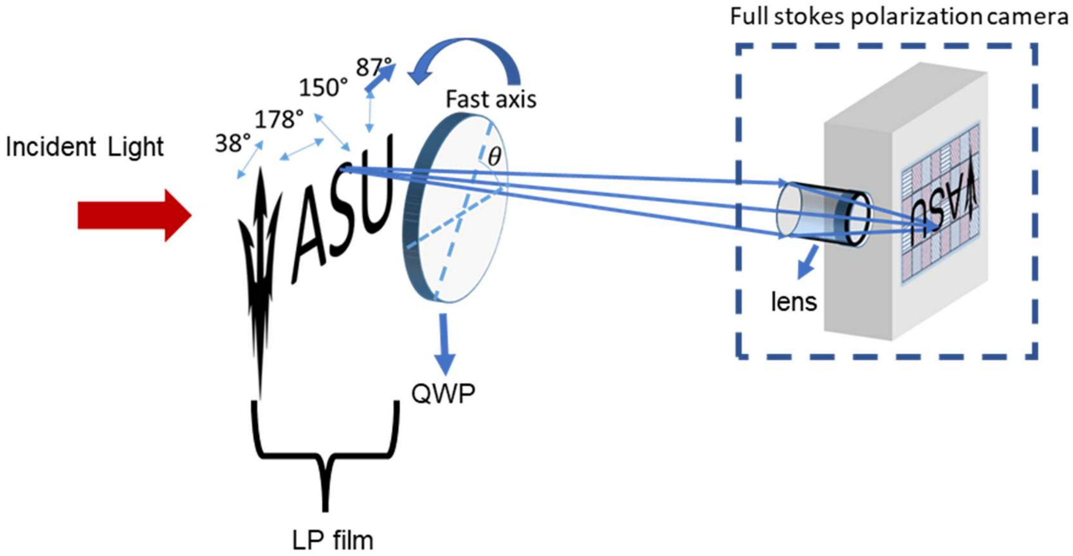

Figure 3.21: Experimental setup for dual wavelength full-Stokes polarization imagery in the lab environment.

In this session, we demonstrate dual wavelength full Stokes polarization imaging of various object in Lab environment to show the potential of MCFPIs. The experimental setup for full Stokes polarization imaging is shown in figure 3.21. A 40-nm bandpass filter centered at 650nm and 500nm was applied in front of the mercury lamp fiber separately. The object imaged here are linearly polarizing films cutted into the Arizona State University logo. Logo' fork',' A',' S',' U' are linearly polarized at 38°,178°,150°,87° respectively. For better contrast and to allow light to transmit from behind, the LP logo was taped onto unpolarized paper. A camera zoom lens with a field of view of 45°(H)-5.35°(H) is applied for imagery. In the indoor measurement environment, the practical field of view applied in the measurement is ~±12°. A zero-order quarter-wave plate (QWP) with a fast axis along 45° was attached to the camera lens to modulate transmitted LP into elliptically polarized light .

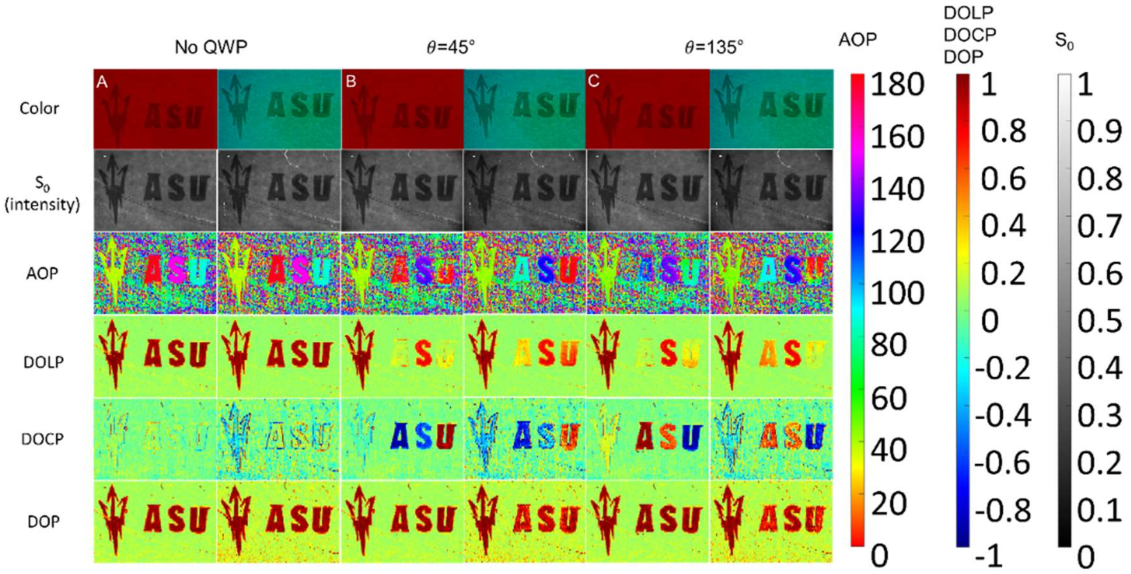

Figure 3.22: Full Stokes polarization imaging of a linearly polarized film with a quarter-wave plate as an imaging filter. Image section A, The linearly polarized polymer film cutted into the logo of Arizona State University. B. A zero-order quarter-wave plate with a fast axis rotated to 45° was added as the imaging filter. C. Quarter-wave plate fast axis rotated to 135°.

Figure 3.22 shows the full Stokes polarization images by our polarization camera of a homemade Arizona State University logo that is elliptically polarized. Section A shows the linearly polarized logo measured under red and cyan color, respectively. The AOP image of the LP film accurately depicts the major axis of the polarization ellipse, which is unseen by a normal camera. A high value of both DOLP and DOP image at the logo region shows that light transmitted through the ASU logo are highly linearly polarized. Section B shows the quarter-wave plate fast axis rotating at 45°. For red color input, the zero-order waveplate has retardance close to $\pi/2$, and the 'fork' and 'S' LP sheets' major axis is close to the fast axis. Thus, their imaged polarization state remains highly linearly polarized, as indicated by the red DOLP image. Logo 'A' 'U' LP axis is close to 45°, 135°away from the fast axis; thus, their imaged polarization state is highly circularly polarized with opposite handedness, as accurately indicated by the red DOCP image. On the other hand, the zero-order waveplate has retardance close to 0.64π. Therefore the cyan DOCP values of the 'A' , 'U' are smaller than the red color, while the cyan DOLP values of 'fork' and 'S' are larger than the red color counterpart. As clearly indicated by the cyan DOLP and DOCP images. Despite obvious changes in DOLP and DOCP images compared to Section A, the DOP values remain high in Section B; this means the linearly polarized light is converted to circular polarization without polarization degeneration. On the contrary, for Section C, the fast axis of the QWP rotates to 135° since the QWP fast axis and slow axis are flipped. In this case, the sign of DOCP of 'fork' , 'A' , 'S' , 'U' are all reversed, as clearly indicated by red and cyan color DOCP images.

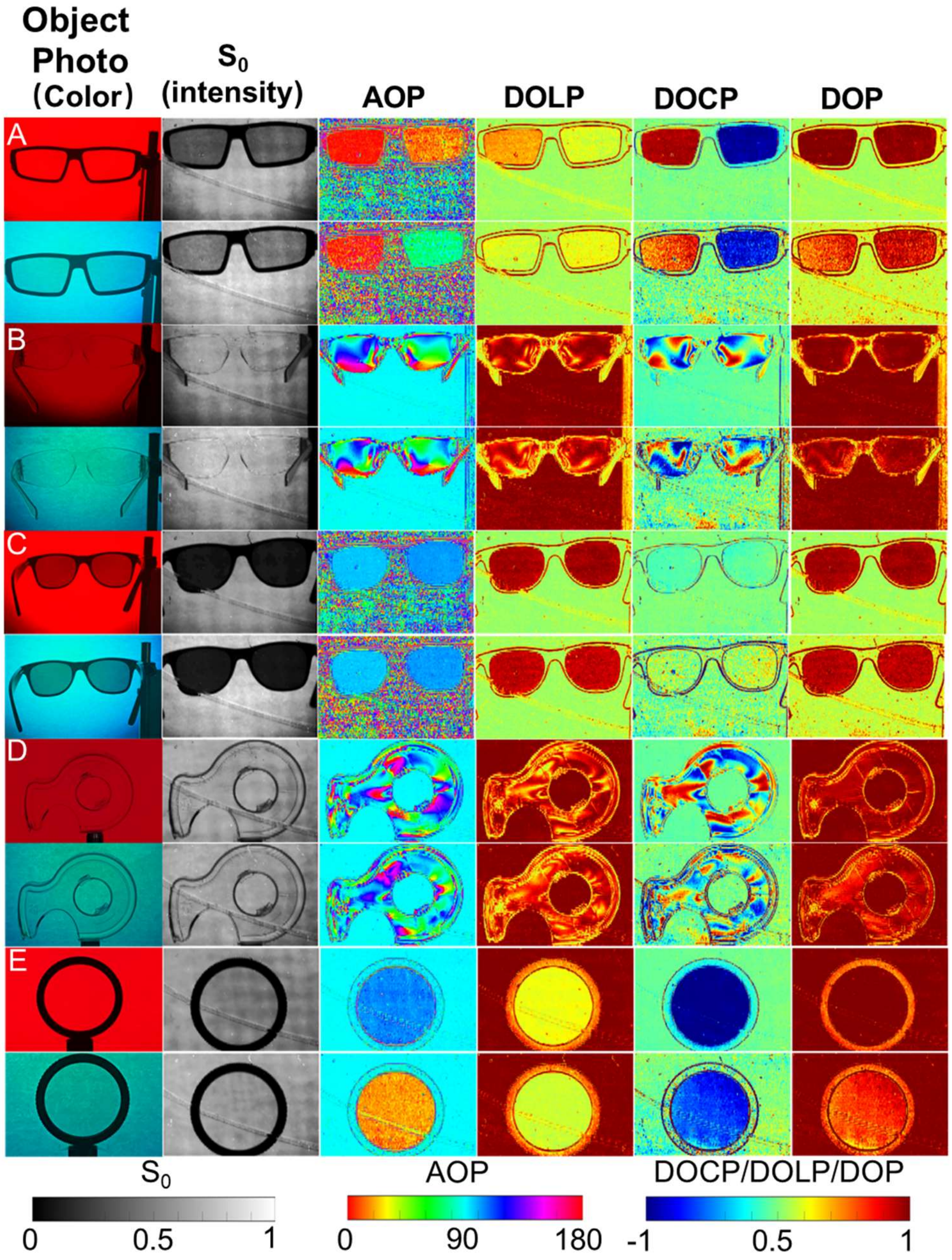

Figure 3.23: Full stokes polarization images of various objects. Full Stokes polarization imaging of objects carrying polarization information. Section A:3D glasses with the unpolarized background; section B: Plastic goggles with CP input as background. Section C: Sunglasses with unpolarized input as background. Section D: Plastic cage, with CP input as background. Section E: A camera CP filter, with CP input as background. In each case, an object photo was taken by a cell phone camera. “Color” image indicates Bandpass filters applied, 650nm±20nm (Red) and 500nm±20nm(Cyan) in front of the light source.

Next, we demonstrate the full Stokes polarization imagery with several objects containing polarization information invisible to normal imaging sensor, as shown in Figure 3.23. Each image section includes an object photo taken by a cell phone camera; an image with colorful background identifying the color; the raw exposure S_0; the angle of polarization (AOP); the degree of linear polarization (DOLP); the degree of circular polarization (DOCP) and the degree of polarization (DOP). Next, we discuss those sections respectively. Section A shows a pair of 3D glasses consisting of opposite CP information. The handedness of the input CP cannot be seen in the sample photo and intensity image but is clearly shown in the DOCP image. We notice that the values of DOCP and AOP of the right glasses are different when taken with red and cyan colors, indicating differences in the transmitted polarization state of 3D glasses under a different color. Section B shows a pair of plastic goggles. In the sample photo, the plastic goggle looks transparent. However, the DOCP image of goggles looks rather un-uniform because of the birefringence of plastic stemming from stress. In addition, the goggles' DOCP image under the red and cyan color light input shows readily different distribution, indicating plastics' birefringence dependence on the input color. Such demonstration clearly exemplifies the advantage of full Stokes polarization imaging under dual operation wavelengths, which could be applied to numerous applications such as biomedical imaging, surveillance, and remote sensing. Section C examines the polarization information of sunglasses. The red and cyan DOLP images and DOP images both show high values, while the DOCP value of the glasses region is nearly 0, indicating the unpolarized light gets linearly polarized upon transmission through the sunglasses. Both red color and cyan color images show similar conclusions, revealing the broadband linearly polarized characteristics of the sunglasses. Section D depicts a plastic cage imaged with 0°LP as the input background. High DOCP values and un-uniform AOP image in the cage area are due to the inner stress of the plastic material upon molding, giving rise to birefringent material optical characteristics. We notice that the red and cyan color DOCP are readily different, which reveals differences in the inner stress distribution of the plastic cage under different colors. Section E examines a simple test; the LCP camera filter is circularly polarized; this is not visible to the traditional imaging sensor but is clearly shown in red and cyan color DOCP images. Besides, thanks to dual operation wavelength, our sensor shows that the AOP of the CP filter is readily different in red and cyan color, indicating the light transmitted through the LCP filter with different wavelengths shows different polarization states.

3.6. Conclusion and Discussion

In this work, we have designed and fabricated MPFA of 168 by 56 meta-pixels and integrated them onto a CMOS sensor to form a full Stokes polarization imaging sensor. We first experimentally demonstrated the chiral metasurface operated on dual wavelength with CPER over 22 at red color and 2.5 at Cyan color. Moreover, we fabricated VCDG with LPER at the operation wavelength range. We then integrated the MPFA onto the CMOS sensor and calibrated the sensor polarization detection with the instrument matrix calibration method. With calibration, we achieved high stokes measurement accuracy: Averaged measurement Error less than 2% for S_1, S_2 S_3 in red and cyan color. Moreover, our polarization imaging sensor can maintain an error of less than 5% up to ±20° oblique incidence for red color and ±5° for Cyan color. Finally, we demonstrated the full Stokes polarization imaging in real-life objects invisible to the traditional imaging sensor at red and cyan color with total operation bandwidth of 80nm. From the polarization images of objects, we find polarization information carried by these objects is color-dependent, revealing the advantage of dual-wavelength operation.

Overall, our full Stokes polarization sensor is a mini, ultra-compact, full Stokes parameter imaging device that could be widely adopted in various real-life applications, such as enhancing contrast in machine vision, material index sensing, and biomedical imaging. Etc.

CHAPTER 4

SCALABLE NANO MANUFACTURING OF METASURFACE POLARIZATION IMAGING SENSORS

This chapter demonstrates a scalable manufacturing process based on nanoimprint lithography (NIL) for the chip-integrated full Stokes polarization imaging sensor. The proposed NIL fabrication process greatly increases fabrication efficiency, thanks to its layer-by-layer nature. More importantly, we successfully demonstrate that NIL based fabrication process can not only simplify the fabrication procedures, thereby dramatically lowering the cost, but also improves the optical performance of chiral metasurface by surface planarization. Remarkably, an improvement in optical performance in CPER was observed up to 10 times compared to devices fabricated by an EBL-based process, as demonstrated in Chapter 3.

4.1. Introduction

Previously in chapter 3, a full Stokes polarization imaging sensor using an MPFA composed of a bi-layered metasurface has been demonstrated. Such metasurface structures require fabrication accuracy of structural dimensions up to less than 10 nanometers scale, plus a highly accurate alignment between the top and bottom metasurfaces to measure each polarization state. This task is resolved using EBL, which has been widely used to fabricate nm-scaled metasurfaces. The first layer is an EBL pattern followed by sputtering of the dielectric layer, i.e., silicon dioxide (SiO_x) as the spacer layer prior to 2nd EBL patterning and alignment. Although this process managed to demonstrate the feasibility of bi-layer integration, it is not suitable for scalable manufacturing. Because EBL can only write one device at a time at a low writing speed due to its line-scanning nature. In addition, it is proved in chapter 3 that the spacer layer sputtered by SiO_x has high surface roughness, resulting in a pronounced degradation of device performance in their LPER and CPER.

This chapter demonstrates a scalable manufacturing process based on NIL for the chip-integrated full Stokes polarization imaging sensor. Here, the top layer of Si nanogratings is patterned by thermal-NIL. Followed by the 2nd layer of the ultra-violet NIL (UV-NIL) process. A mask aligner with Moiré fringe is applied for an accurate alignment process with an alignment accuracy of less than 150 nm in x- direction and less than 200nm in the y-direction. Noticeably, the spin-coated UV resist from the 2nd layer NIL process acts as a spacer layer and provides surface planarization without adding additional fabrication processes. Therefore, the proposed NIL fabrication process greatly increases fabrication efficiency by simplifying the fabrication process, thereby dramatically lowering the cost. As expected, an improvement in optical performance in CPER was observed up to 10 times compared to devices fabricated by an EBL-based process, as demonstrated in Chapter 3.

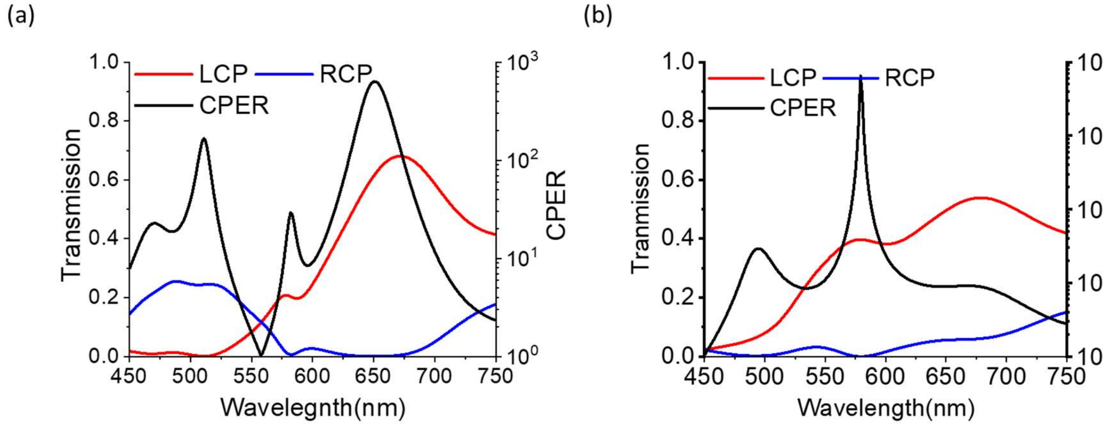

Figure 4.1: FDTD simulated transmission and CPER of chiral metasurfaces design. (a) Design A target to cover red and blue color wavelengths (b) Design B target green color wavelengths.

The configuration for the metasurface polarization filter array (MPFA) is similar to the ones demonstrated in chapter 3.2. Each super pixel composes of 4 micro scales VCDGs as LP filters. The dimensions for VCDGs are the same as the design discussed in chapter 2.3. The period, Al thickness, duty cycle, and vertical gap size are 210nm, 80nm, 0.5, and 30nm, respectively. In addition, two pair of chiral metasurfaces with different dimensions designed with working wavelength center at Red(650nm)/Blue(480nm) and green color(530nm) is added to broaden the detection wavelength range, as shown in Figure 4.1. The period of top Si nanogratings, Si thickness, and Si grating width are 297nm, 130nm, and 100nm for design A. The spacer layer thickness is considered to be 400nm and period, Al thickness, duty cycle, and vertical gap for bottom layer VCDGs are 210nm, 80nm, 0.5, and 30nm for design A. For design B, the period of top Si nanogratings, Si thickness, and

Si grating width are 180nm, 130nm, and 70nm, respectively. The spacer layer thickness is 400nm, too, while the period, Al thickness, duty cycle, and vertical gap for bottom layer VCDGs are 180nm, 80nm, 0.5, and 30nm, respectively.

Figure 4.1(a) shows the optical performance of design A, which is the same as the ones demonstrated in chapter 2.4. CPER of design B is larger than 10 from 540nm to 600nm, as shown in Figure 4.1(b). With two pairs of chiral metasurface combined, CPER is larger than 10 from 450 to 525nm and 540nm to 700nm, which covers 235nm wavelength range in visible. On the other hand, the metal frame spacing distance between adjacent polarization filters is reduced to 3.1 μm and the size of the metasurface filter is reduced to 4.65 μm×4.65μm to increase the image resolution.

4.3. Scalable Nano Fabrication by NIL

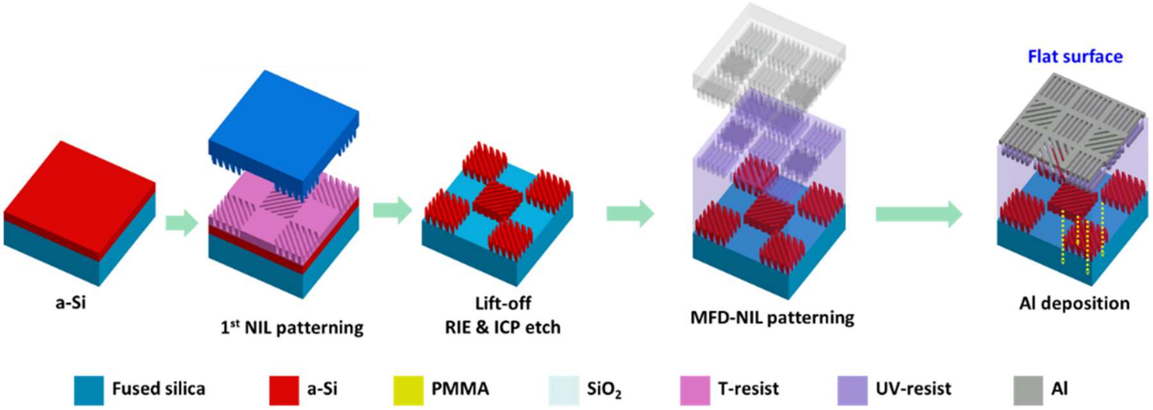

Figure 4.2: Fabrication schematic of metasurface array for full Stokes polarization imaging sensor using NIL. (Acknowledged Shinhyuk Choi for developing the fabrication process based on NIL and providing the schematics of fabrication process)

Figure 4.2 shows the schematic of the fabrication process flow for the metasurface filter array based on NIL. Si nanogratings are firstly patterned by hard mold using NIL, followed by Si drying etching to form Si gratings. Then a thin layer of UV resist is spin-coated onto the fabricated Si nanogratings. Because UV resist can fill the gap caused by Si nanogratings, the spin-coated surface has a much lower surface roughness than SiOx sputtering. NIL is performed directly on planarized UV resist to form grating patterns, followed by Al deposition to form vertically coupled double-layered Al gratings.

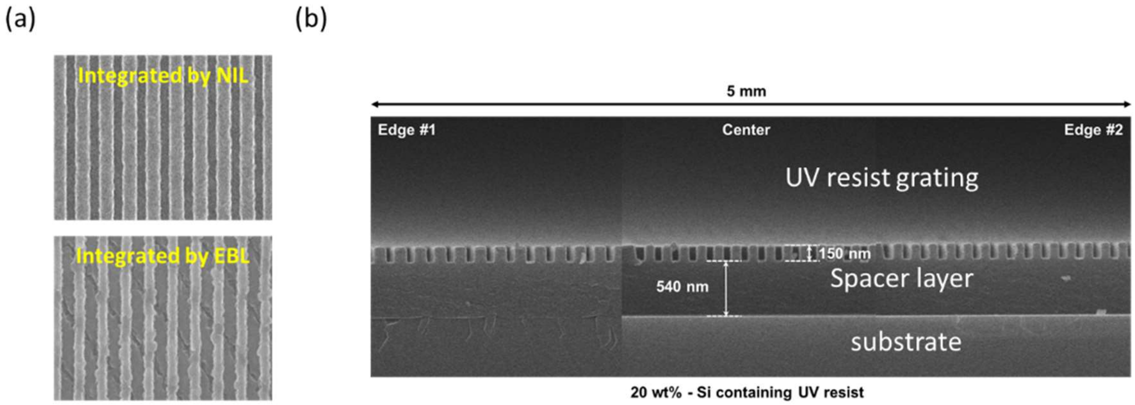

Figure 4.3: SEM images of chiral metasurfaces fabricated by NIL and EBL, respectively. (a) Top-down view SEM images of chiral metasurfaces fabricated by NIL and EBL, respectively. (b) Cross-sectional SEM images of chiral metasurfaces fabricated by NIL. (Acknowledged Shinhyuk Choi for providing SEM images and performing NIL fabrication)

Figure 4.3(a) shows the SEM image of a device fabricated by NIL and EBL, respectively. For the EBL sample, a clear surface modulation on the spacer layer can be observed, indicating a large surface roughness. On the contrary, surface modulation on the NIL sample is not observable, meaning a great improvement in the surface roughness of spacer layer. A cross sectional SEM image of chiral metasurfaces fabricated by NIL is shown in Figure 4.3(b), the surface roughness of the planarized spacer layer shows a thickness of 540nm across the 5mm range, indicating a good surface planarization uniformity in mm scale range.

4.4. Optical Characterization of VCDGs and Chiral Metasurfaces Fabricated by NIL

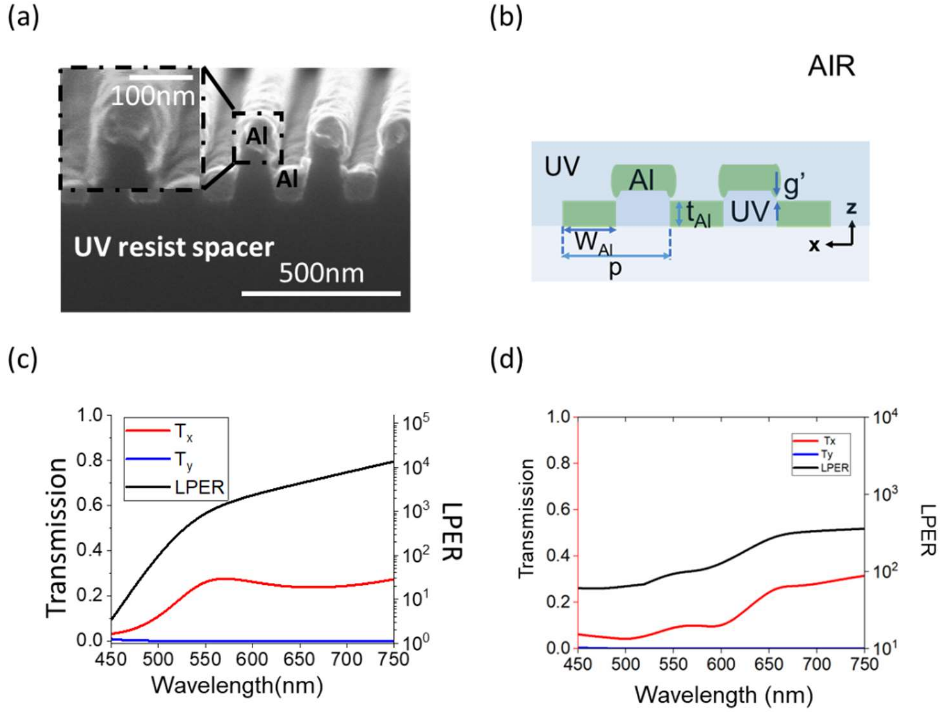

Figure 4.4: Optical characterization of VCDGs fabricated by NIL using a visible spectrometer. (a) Cross-sectional SEM image of VCDGs manufactured by NIL (b) simulation setting adapting metal attachment to the VCDGs sidewall (c) FDTD simulation of VCDGs fabricated by NIL. (d) Measured transmission and LPER of VCDGs. (Acknowledged Shinhyuk Choi for taking SEM picture and performed NIL fabrication of VCDGs)

Figure 4.4(a) shows the cross-sectional SEM image of the VCDGs fabricated by the NIL fabrication process. 80nm of Al is deposited onto the imprinted UV resist gratings. Noticeably, metal attachment is observed after Al deposition. This is because the nano imprinter we applied does not have sufficient pressure to ensure a straight sidewall of UV resist as imprinted, leading to a curved shape at the UV resist grating edge and thereby causing the metal attachment to the sidewall. This issue can be resolved by using a higher-pressure nano imprinter. As a result, the metal attachment needs to be reflected in the FDTD simulation to reflect the real dimension configurations. The adjusted dimension configuration of VCDGs is shown in Figure 4.5 (b). Here a metal attachment of 30nm is considered, and the vertical gap g' is defined as the distance from the tip of the metal attachment to the top of the bottom Al grating. The period and thickness of Al are 210nm and 80nm, and the vertical gap g' is 30nm, with a duty cycle of 50%. Simulated transmission and LPER of adjusted dimension are shown in Figure 4.5 (c); a dramatic decrease in efficiency is observed due to metal attachment, corresponding to an efficiency of ~23% at red color (650nm), while LPER does not get affected. Figure 4.5(d) shows the measured device transmission and LPER, which agrees well with the FDTD simulation, measured efficiency at 650nm is 24% with LPER over 100 from 520nm to 750nm.

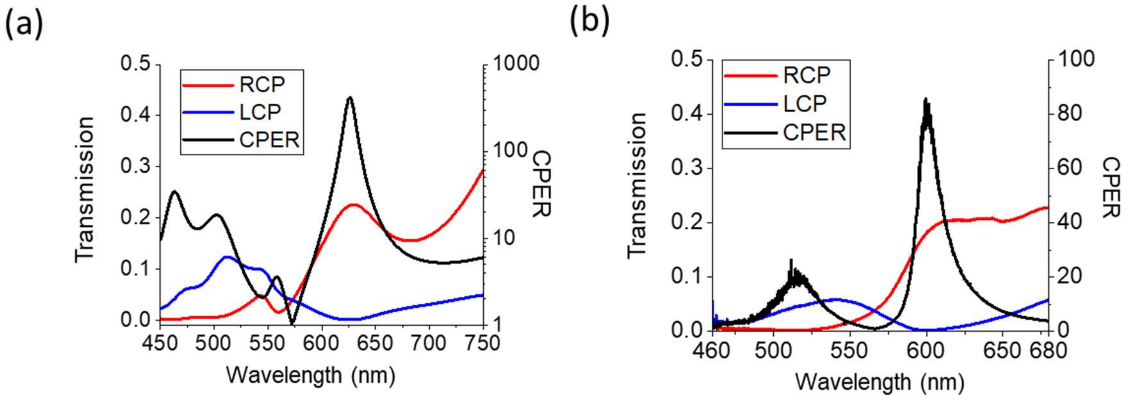

Figure 4.5: Simulation and characterization of the chiral metasurface fabricated by NIL. (a) FDTD simulated transmission and LPER of design A fabricated by NIL. (b) Measured transmission and LPER of design A fabricated by NIL.

Figure 4.5(a) shows the FDTD simulated transmission and LPER of design A fabricated by NIL. The spacer layer thickness is adjusted to 520nm, and VCDG settings is consistent with the settings described above. Although the efficiency is reduced due to metal attachment, it is clear the CPER is not degraded. Figure 4.5(b) shows the characterization results of the chiral metasurface (design A). As a result of surface planarization, the optical performance of the chiral metasurface fabricated by NIL shows a 4 times improvement at red color (600nm) and 10 times at green (~520nm) compared to ones fabricated by EBL as shown in chapter 3.3. This is because the improved spacer layer roughness increases the LPER of VCDG fabricated on top, thereby increasing the CPER of the chiral metasurface. The next stage of work should focus on characterizing the optical performance of MPFA to check the uniformity of LPER, CPER, etc.

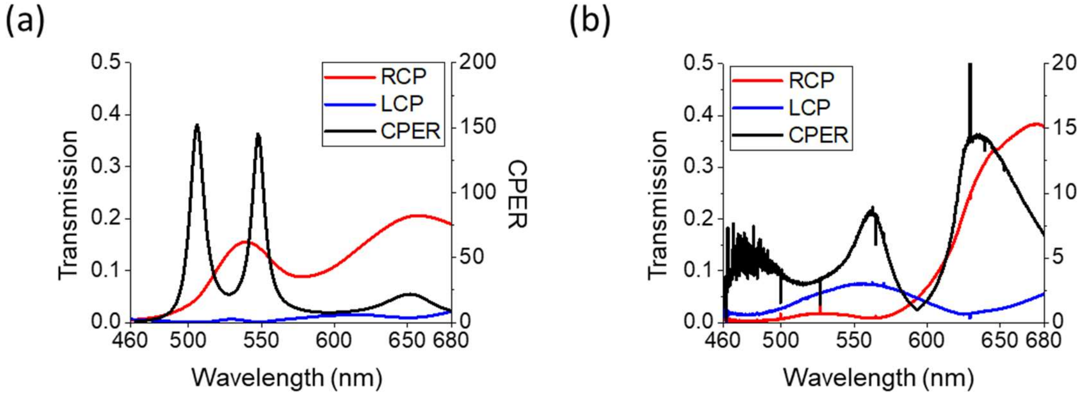

Figure 4.6: Simulation and characterization of design B fabricated by NIL process. (a) FDTD simulated transmission and CPER of design B. (b) Measured transmission and CPER of design B.

Figure 4.6 (a) shows the FDTD simulated transmission and CPER of the chiral metasurface target at green color design (design B). The spacer thickness is adjusted to 520nm to reflect the real thickness of UV resists spin-coated. As for bottom layer VCDGs, the vertical gap is considered to be 30nm with 30nm metal attachment to the sidewall too. Still, the efficiency is diminished due to the metal attachment of bottom layer VCDGs while CPER is not highly affected, as CPER at green color remains higher than ten from 500nm to 570nm. However, the measured CPER is two orders lower in green color and remains the same at 650nm, as shown in Figure 4.6(b). One possible reason for such degradation is that the smaller period design tends to be more sensitive to parameter differences, such as spacer layer thickness and Si grating width differences. Nevertheless, the reason for the degradation at green color remains unclear and requires further investigation.

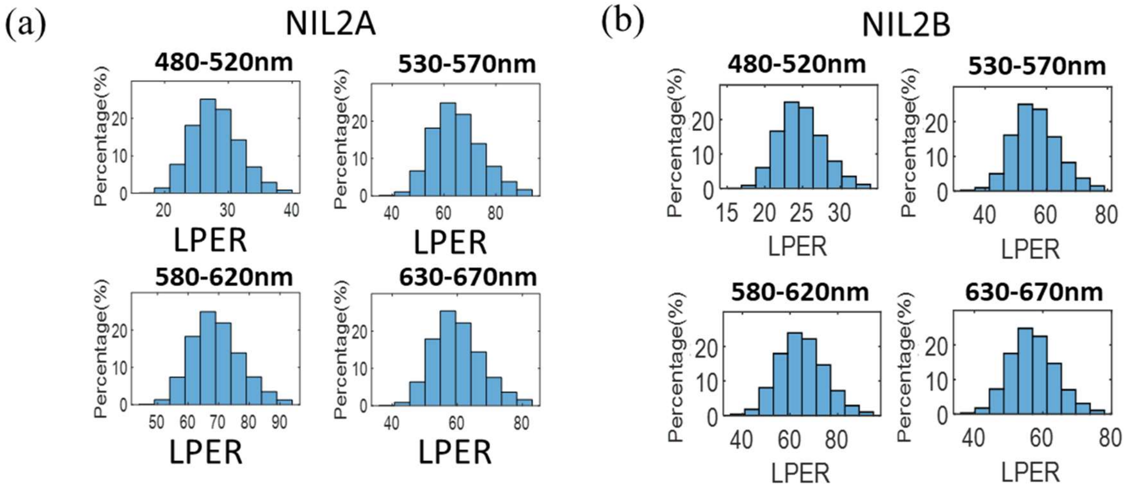

Figure 4.7: Distribution of LPER of micro-scale LP filters integrated onto CMOS imaging sensor. (a,b) Distribution for chip names NIL2A and NIL2B, respectively.

To verify the reproducibility, we fabricated and integrated 2 MPFAs onto the CMOS imaging sensor in one batch and exam their consistency. Figure 4.6 (a)(b) shows the LPER distribution of devices named NIL2A and NIL2B, respectively. The LPER distribution shows good consistency between the two devices, the averaged LPER at 650nm and 500nm are 60 and 27, respectively, which is sufficient for qualitatively measuring the S1 and S2, a more rigorous calibration process is still needed to provide high accuracy full Stokes polarization detection and imaging.

The measurement of CPER of micro-scale CP filters is ongoing, requiring further investigation.

4.6. Conclusion and Discussion

This chapter presents a scalable fabrication method for a full Stokes polarimetric imaging sensor based on NIL. Thanks to the layer-by-layer nature of the NIL process, not only the fabrication throughput is greatly increased compared to EBL-based fabrication, but the fabrication procedures are also simplified. More importantly, the surface planarization of the 2nd NIL process improved the optical performance of chiral metasurfaces up to 10 times compared to a device fabricated based on EBL.

This demonstration strongly implied that the NIL-based metasurface fabrication process demonstrated in this chapter is paving a new way toward producing novel optical components based on metasurfaces, such as metalens and holograms at high throughput and low cost.

CHAPTER 5

APPLICATIONS OF POLARIMETRIC IMAGING SENSORS

This chapter presents several applications using polarimetric imaging sensors. Firstly, a dual-camera full-Stokes underwater polarization imaging system is demonstrated; the system is capable of automatically imaging the whole sky with variable exposer time, high accuracy, high repeatability, and high SNR. A demonstration of polarization mapping under a clear sky in the air and clean water in the swimming pool is presented to show the potential applications in underwater navigation and Geolocation. Secondly, polarization imaging of objects through turbid water is demonstrated to enhance underwater visibility. Thirdly, polarization imaging of silver dendrites is demonstrated to reveal the unique material properties of the dendrites.

5.1. Introduction of Underwater Polarization Navigation

Automated underwater navigation and positioning system are vital to nearly all underwater applications because Global Positioning System (GPS) is limited to usage in very shallow seawater (~within a few meters) due to water absorption [71]. Alternatively, acoustic navigation systems [72, 73] can be applied in the deep ocean; yet they require predetermined reference locations and are not suitable for long-distance navigation. In addition, underwater magnetic or gyro compass [74, 75] can be used in the deep ocean; yet they require references for error correction and geolocation and are also not suitable for long-distance navigation. Recently Underwater polarization light patterns [76, 77] have been proved to serve as a solar compass and can also be used in the marine environment to determine global location [76].

Table 5.1: A comparison of different underwater navigation techniques

Navigation method	**Acoustic Positioning**	**Magnetic or Gyro compass**	**Polarization Mapping**
Require reference for navigation	Yes	No	No
Operation depth	Up to 10km	No Limitation	Up to >200m in theory;20m (demonstrated)
Position Accuracy	0.3~2.0 m	Angle accuracy 1~3°	60km(geolocalization) or 6m for every 1km traveled
Suitable for long-range geolocalization	Require reference locations	Require reference locations	Yes
System compactness	Accurate position requires complex systems with pre-installed transponder array	Compact	Compact

Table 5.1 provides a comparison of different underwater navigation methods. Among these techniques, polarization navigation is the least well-studied. Yet, it has attractive advantages over other techniques in the potential long-range geolocation requiring no reference locations and complex systems [76, 77]. Moreover, a compact polarization-based navigation device can also be combined with other technologies to mitigate the limitations (e.g., operation depth), improve positioning accuracy and expand overall system capability.

Skylight polarization has been applied for navigation since ancient times, especially among insects such as ants and beetles [78, 79]. In recent decades, there have been few demonstrations of skylight polarization-based navigation in terrestrial environments [80-85]. Yet, polarization navigation in marine environments is much more challenging than skylight polarization navigation in the terrestrial environment. The progress of polarization-based navigation in the marine environment is left behind both by skylight navigation in the terrestrial environment and other marine navigation techniques. In one of the recent demonstrations [76], using a manual rotation polarization camera mounted on a tripod in water depth within 2 to 20m, sun azimuth and elevation angle determination with RMS error of 8.57° and 5.82° respectively, and global position error of 817Km (when the sun elevation was more than 40°) is reported. Further processing of the data with the kNN regression model reduced the error to 6.02°, 2.92°, and 422 km, respectively. When sun elevation was below 40°, they obtained an RMS error of 5.46°, 6.23°, and 1970Km, respectively, for sun azimuth, elevation, and global positioning (with kNN regression). Continuous measurement showed their ability to distinguish between two consecutive global positions at around 61 km on average (or 6m error for every 1 km travel). They used a theoretical model considering sunlight refraction and single Rayleigh scattering inside the water to determine the sun's global positions from the measurement. In another more recent demonstration [77], continuous measurements were done inside a pool of clean water (depth 1.5m, instrument height unknown) using an underwater system composing a linear polarization (LP) camera assembled with a fisheye lens. RMS error of the solar zenith and azimuth angle tracking was 0.3° and 1.3°, respectively, obtained using a theoretical model considering single-Rayleigh scattering of sunlight in air and refraction of the skylight into water. However, the performance of state-of-art polarization-based navigation systems [76, 77], especially in position accuracy and operation speed, is insufficient for practical applications. Besides, these systems all require manual operation to perform polarization mapping, either by manually rotating the polarization camera or putting on a mask to block the sun’s direct incidence. Moreover, these systems often apply

LP cameras for navigation, leading to lost information related to incoming light's circular polarization (CP) component. Yet, CP components may exit in the turbid water environment due to the existence of Phytoplankton [86] and have not been studied in previous works.

In this chapter, we first demonstrate an automated underwater imaging system. The advantage of our system can be summarized in three folds: First, our system has a dual polarization camera, which can detect full Stokes parameters simultaneously. Secondly, our system has high polarization detection accuracy as we employed a small angle-of-view imaging lens to reduce polarization aberration. Thirdly, our system is fully automated; The camera exposure can be automatically adjusted during mapping. Therefore, no manual operation is required to block the sun’s direct incidence. We then present a demonstration of polarization mapping under a clear sky in air and clean water in a swimming pool to show the potential applications in underwater navigation and Geolocation.

5.2. Underwater Polarization Navigation System Concept

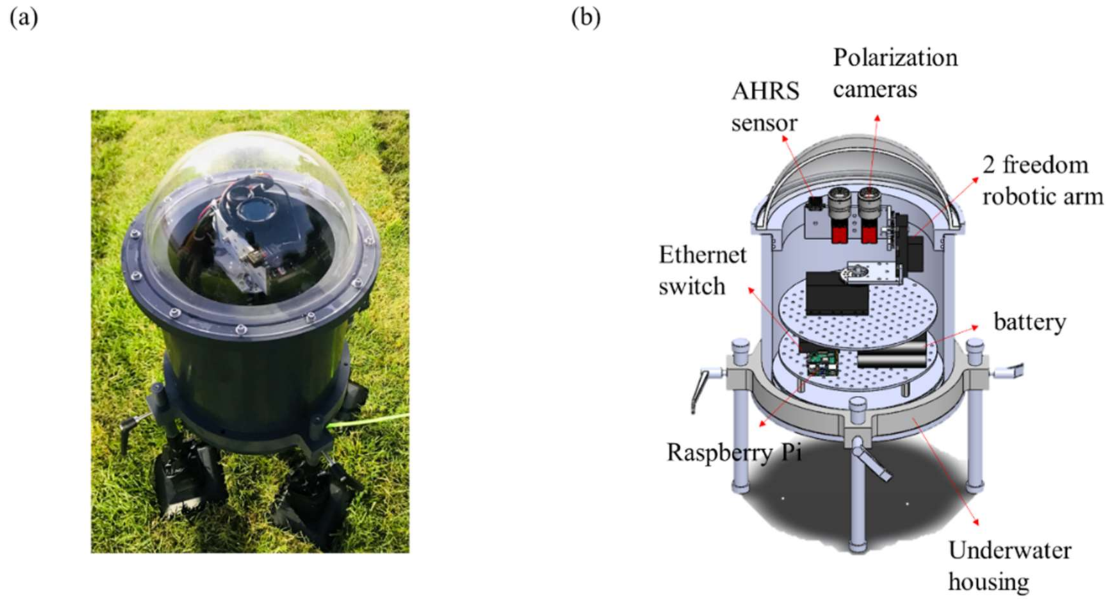

Figure 5.1: Full Stokes polarization navigation system configuration. (a). Photo of an underwater polarization imaging system (b). 3D Schematic of the underwater polarization imaging system. (Setup built by Jiawei Zuo, Jiayu Liu, and Jing Bai).

Figure 5.1 (a) shows the image of the underwater polarization imaging system. It consists of an underwater housing that has a 14-inch diameter transparent half-sphere dome for upwards imaging. A full Stokes polarization mapping system is assembled inside the housing, which consists of a robotic arm with 2 degrees of freedom, an AHRS sensor mounted on the top holding plate, and two DoFP polarization cameras mounted side-by-side, as shown in Figure 5.1(b). A Raspberry Pi is used as a local controller to precisely control the rotation of the robotic arms and measure the exact pointing direction. The local controller is controlled by a remote controller which is outside of the housing. The cameras, local controller, and remote controller communicate with each other through ethernet cables.

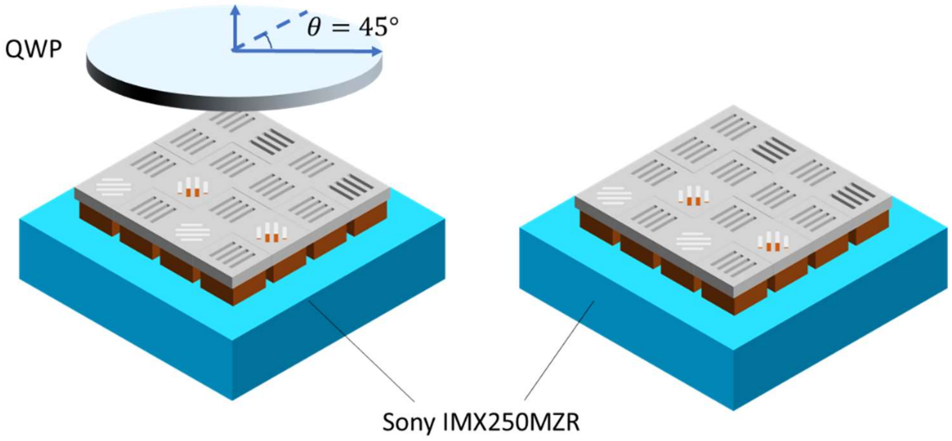

Figure 5.2: Settings of dual DoFP polarization cameras for full Stokes polarization imaging

A 3D schematic of dual DoFP polarization camera settings is shown in Figure 5.2. Pixelated Al nanowires array are directly integrated into CMOS imaging sensor to measure S_0, S_1, and S_2. An achromatic quarter waveplate is assembled in front of one sensor, with a fast axis aligned at 45° to measure S_3 of incoming light. The imaging speed, resolution, and exposure of the two DoLP polarization cameras are kept the same during measurement.

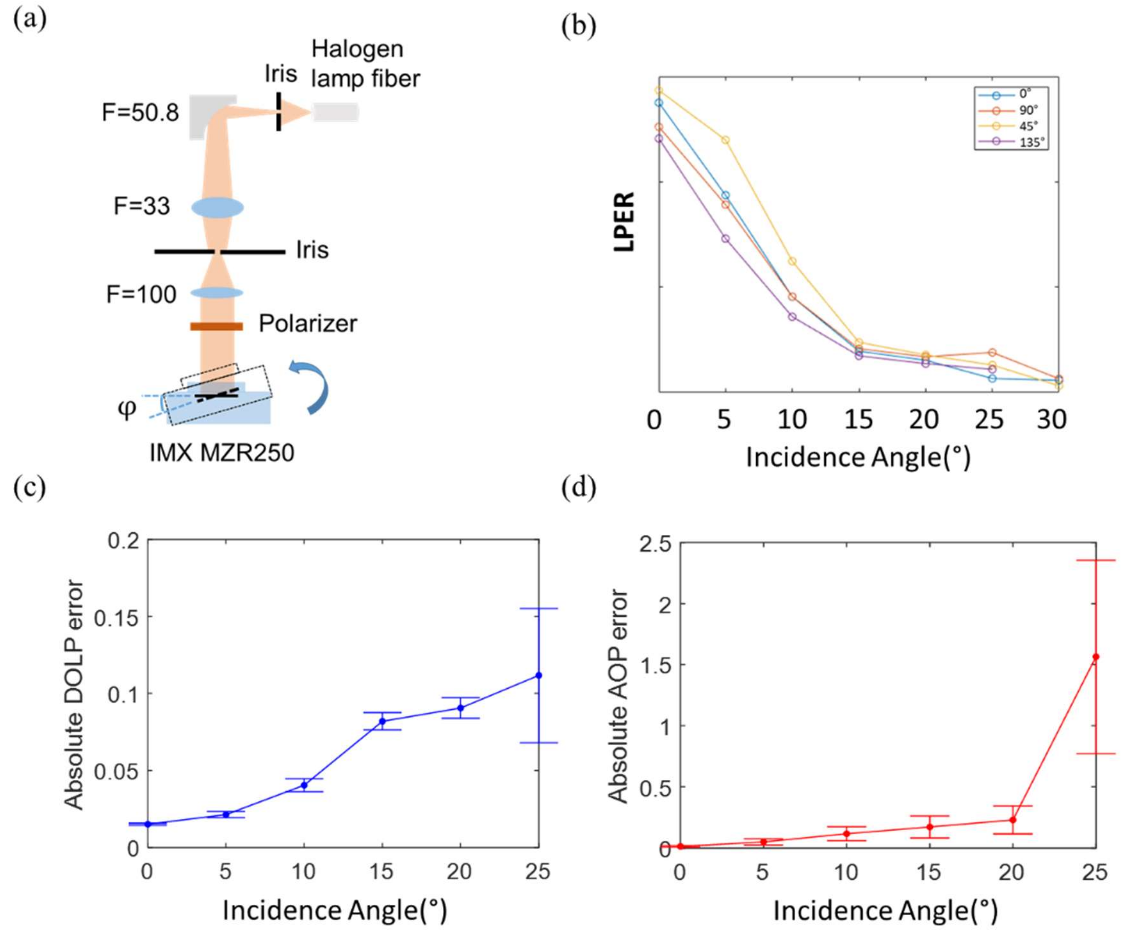

Figure 5.3: Linear polarization extinction ratio (LPER) measurement for IMX 250MZR under different incidence angles. (a). Schematic of an experimental setup for measuring Linear polarization extinction ratio (LPER) of Sony IMX MZR250 under oblique incidence. (b) LPER vs. incidence angle (c) Degree of linear polarization (DOLP) detection error vs. incidence angle. (d) Angle of polarization (AoP) detection error vs. incidence angle. (acknowledged Jing Bai for performing the measurement).

Another important aspect of polarization mapping accuracy is the measurement accuracy of the polarization detector. Here we performed LP detection measurement using

IMX 250 MZR under different incidence angles; the experimental setup is shown in Figure 5.3(a). A uniform, collimated beam with sufficient spot size is incident onto the sensor with the lens removed; a rotational stage is applied to control the light incidence angle φ. IMX MZR 250 has the best performance and LPER above 100 with normal incidence. However, the performance degraded fast with increasing incidence angle, as shown in Figure 5.3(b). The LPER becomes smaller than 50 when the incident angle is larger than 10 degrees. The LPER of the imaging system directly determines the measurement accuracy of the Stokes parameters. The measurement error for DOLP (Figure 5.3(c)) and AOP (Figure 5.3(dc))) increases as the LPER decreases and is sensitive to the input polarization state. To reduce DOLP/ AOP measurement error to <5% and <0.2°, LPER better than 50 or an incident angle smaller than 10 degrees is required. Due to this performance degradation, it would be desirable to use a lens with a smaller angular field of view (AFOV), limiting the incident angle of light and improving the measurement accuracy of the polarization states.

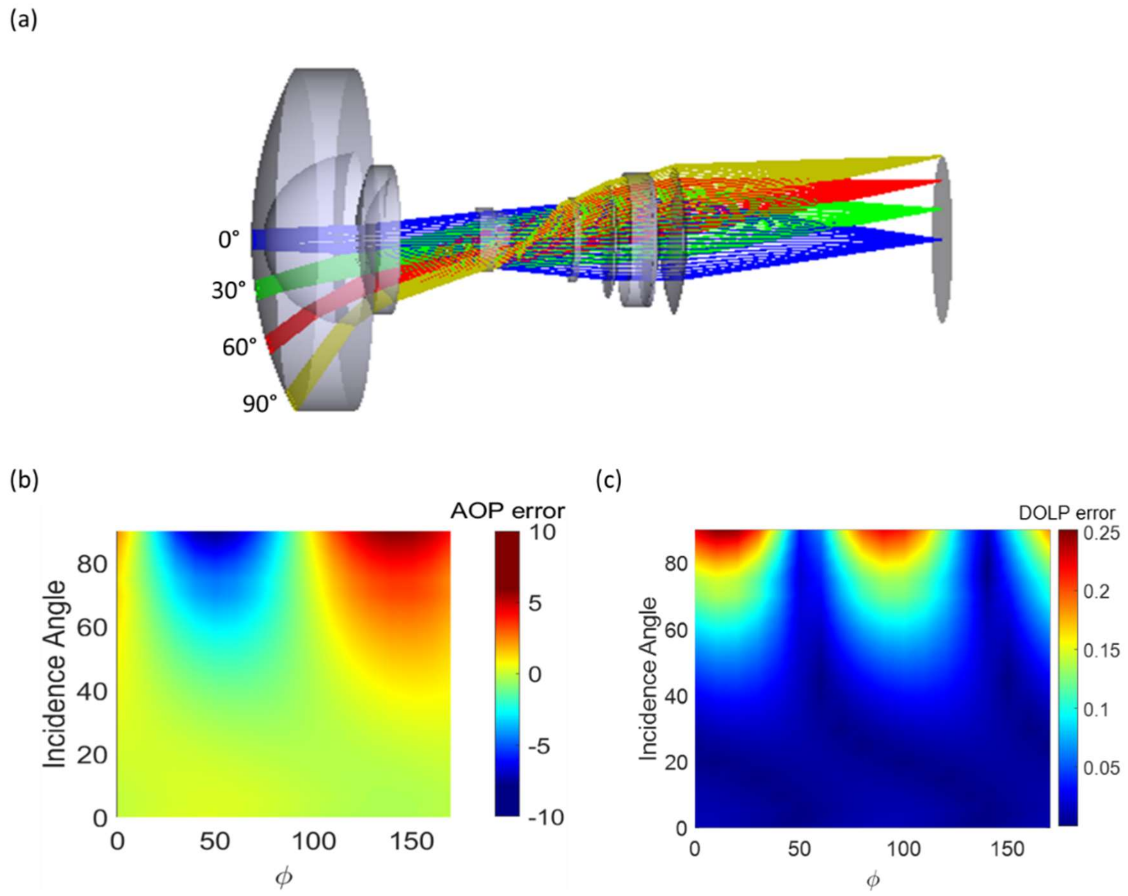

Figure 5.4: Simulation of polarization aberration introduced using polarization ray tracing. (a) Ray diagram of a fisheye lens. (b) AOP error is introduced by the fisheye lens (AFOV=180°) at the focal plane as a function of incidence angle and AOP of linearly polarized incident light. (c) DOLP error introduced by a fisheye lens (AFOV=180°) at the focal plane as a function of incidence angle and AOP of linearly polarized incident light.

Another advantage of using a small AFOV lens is its low polarization aberration. Previous works on sky polarization mapping systems generally use large AFOV lenses, such as the fisheye lens, for polarization mapping [1]. However, the polarization aberration introduced by fisheye lenses is often ignored. Figure 5.4(a) shows the 3D ray diagram of a fisheye lens (No. US07161746-1, downloaded from lens library website) with an AFOV of 180°. The effective focal length and the f-number of the fisheye lens are 10mm and 2.9 for this fisheye lens. The Mueller matrix of the fisheye lens is calculated using the built-in polarization ray tracing function in Zemax. Then, polarization aberration is estimated using linearly polarized light (LPL) as input with changing polarization axis angle ϕ to assimilate skylight polarization. Details about the simulation settings and calculation of polarization aberration are included in Appendix C. Figure 5.4 (b) shows the AOP error mapping as a function of ray incidence angle θ and AOP of incident LPL. AOP error is defined as :

$$\varDelta_{AOP} = Calculated\ AOP\ - Reference\ AOP \tag{4.1}$$

Overall, AOP error increases as the incidence angle increases. Specifically, AOP is less than 1° for $\theta < 40°$ and increases quickly to ~8° at $\theta = 90°$. Figure 4.1© shows the DOLP error as a function of θ and ϕ; DOLP error is defined as :

$$\varDelta_{DOLP} = Calculated\ DOLP\ - Reference\ DOLP \tag{4.2}$$

For the fisheye lens, DOLP error at the focal plane is less than 5% at θ <40° and increases to 25% at $\theta = 90°$. Such high polarization aberration fundamentally limits polarization navigation accuracy.

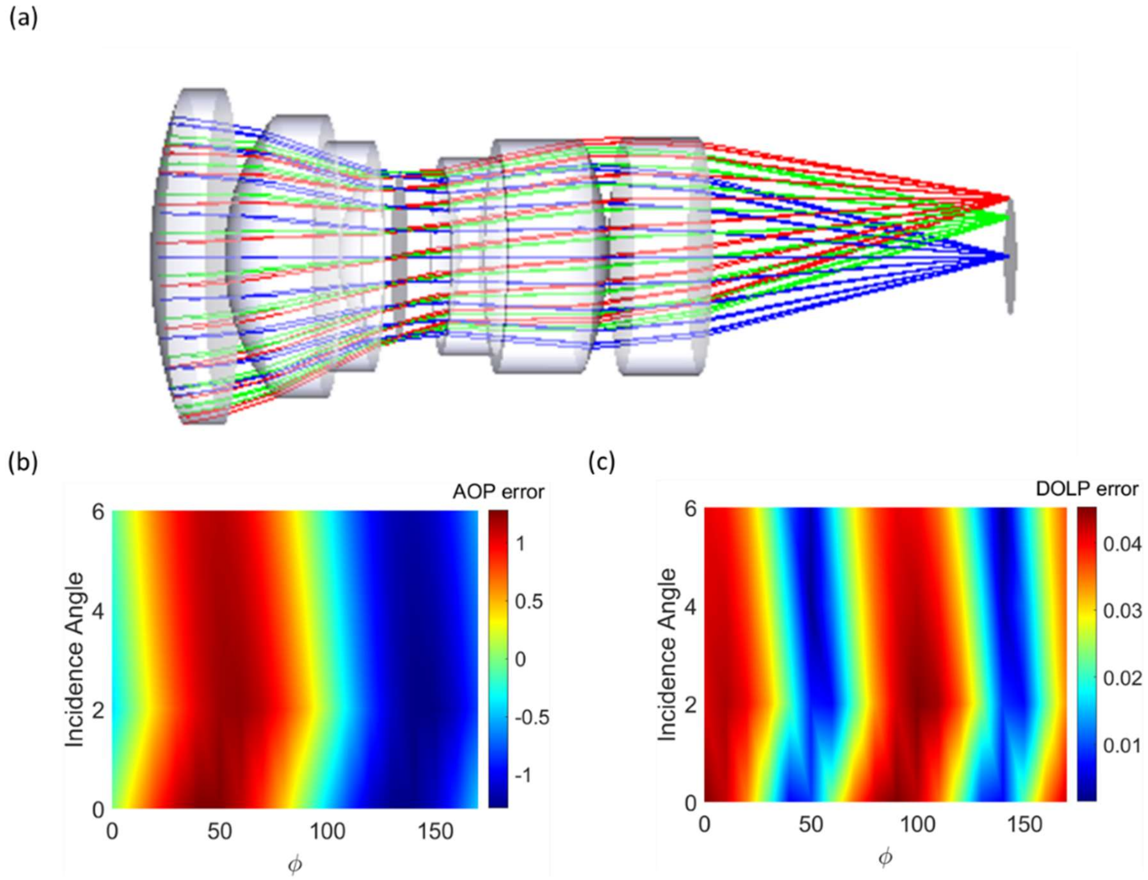

Figure 5.5: Simulation of polarization aberration introduced using polarization ray tracing. (a) Ray diagram of a small AFOV=12° lens. (b) AOP error introduced at focal plane as a function of incidence angle and AOP of linearly polarized incident light. (c) DOLP error introduced at focal plane as a function of incidence angle and AOP of linearly polarized incident light.

Figure 5.5(a) shows the 3D ray diagram of an AFOV=12° lens (No. US02601805-1 downloaded from lens library website [87]). The effective focal length and the f-number of the fisheye lens are 25mm and 4.3 for AFOV=12° lens, respectively. The AOP error and DOLP of it are shown in Figures 5.5(b) and 5.5(c), respectively. AOP error is less than 1° while the DOLP error is less than 5% over the whole incidence angle and LP azimuth angles. Compared to the fisheye lens, the AFOV=12° has a much smaller AOP error range.

Thus, it is favored for high-accuracy polarization mapping of the sky. Besides, a small object is often needed to manually block the sun in the imaging scene when using the fisheye lens to avoid overexposure issues[77] due to strong brightness along the sun’s direct incidence direction. The object location must be adjusted according to the sun’s location, which makes fully automatic polarization mapping difficult. This issue can also be addressed by using a narrow AFOV lens, as now the mapping can be done through spatial scanning mode. During the scanning, the exposure close to the sun can be adjusted accordingly to minimize the impact of the sun's direct incidence on polarization mapping.

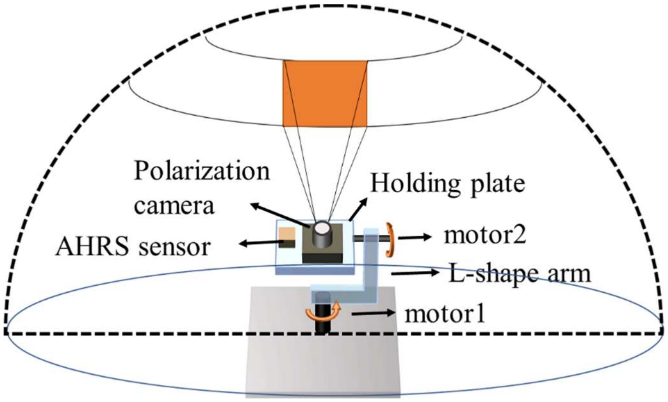

Figure 5.6: Schematic of underwater polarization imaging system mapping the sky polarization by spatial scanning mode.

Figure 5.6 shows the operation of our system during full-sky mapping. The polarization camera is carried by the elevation robot arm, whose rotation movement covers the zenith angle from 0° to 90°. Beneath the elevation arm lies a rotation base for 360° azimuth scanning. During full-sky mapping, a raspberry pi 4B first commands the rotation base and continuously scans 360° in azimuth while fixing the zenith angle. Meanwhile, the camera operates in ‘video mode,’ i.e., lively capturing the polarization image during rotation, and each image exposure is automatically adjusted to obtain the highest signal-to-noise ratio (SNR). Images are saved during imaging and later stitched to full-sky polarization mapping. An industrial attitude and heading reference system (AHRS) 3DM-GX5-25 is applied to indicate geographic (true) North with an accuracy of ±1° in azimuth.

5.3. Sky Light Polarization Mapping

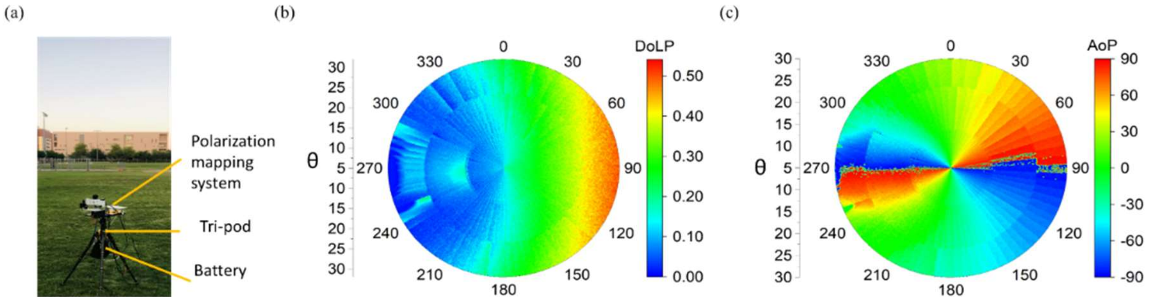

Figure 5.7: Clear sky light polarization mapping using mono DoFP polarization camera. (a). Measurement setup for mapping sky polarization in air. (b). DoLP mapping of the sky from a zenith angle of 5~30° (y-axis). (c) AOP mapping of the sky from a zenith angle of 5~30° (y-axis). (Measurement done by Jiawei Zuo, Jing Bai, and Hossain Mansur Resalat Faruque)

We measure the sky polarization state under sunny, cloudless, or few cloud conditions to verify the system’s polarization navigation accuracy. All the measurements were collected in the air at Arizona State University, in which latitude and longitude are 33.4204362°, -111.9310406°, respectively. To reduce the weight, we mounted the polarization mapping system onto a tripod. A single DoFP polarization camera is applied because the clear sky is mostly linearly polarized and has no obvious DOCP[85]. The measured DOLP and AOP patterns are shown in Figure 5.7(b) and Figure 5.7(c), respectively, as measured in the entire visible spectrum range. The measurement results show two indications of the sun's location: (i) The DOLP pattern shows a minimum at the sun location (azimuth 270°), then gradually increases and reaches a maximum at azimuth 90°, as opposed to the sun. (ii) an evident symmetrical distribution of AOP values can be found along the solar meridian line in azimuth. The uneven and abrupt change of AOP measurement around the sun's position due to overexposure to the sun's direct incidence, even at the minimum exposure time the camera can give. (ii) Fringes are often seen in the measured AOP and DOLP pattern, mainly due to in-perfect image stitching.

5.4. Underwater Polarization Mapping in Swimming Pool

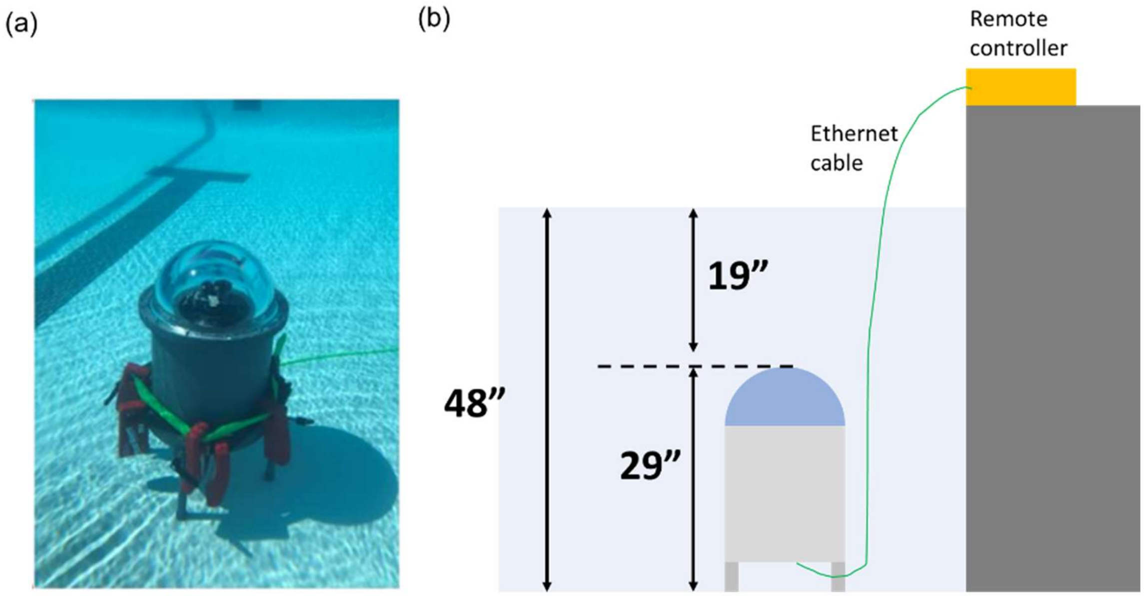

Figure 5.8: Underwater polarization mapping. (a) Image of Measurement setup inside swimming pool. (b) Configuration of underwater mapping. (acknowledged *Md Zubair Ebne Rafique* for processing the mapping results and measurement done by Jiawei Zuo, Mo Tian, Jing Bai, Md Zubair Ebne Rafique, and Hossain Mansur Resalat Faruque).

Figure 5.8(a) shows a configuration for underwater polarization mapping in a swimming pool. The total water depth was around 48 inches, as shown in Figure 5.8(b). The underwater housing was first leveled manually. Then we performed automatic polarization image mapping over 0˚-360˚ azimuth angle and 0˚-50˚ zenith angle to cover the whole sky mapping results inside snell’s window.

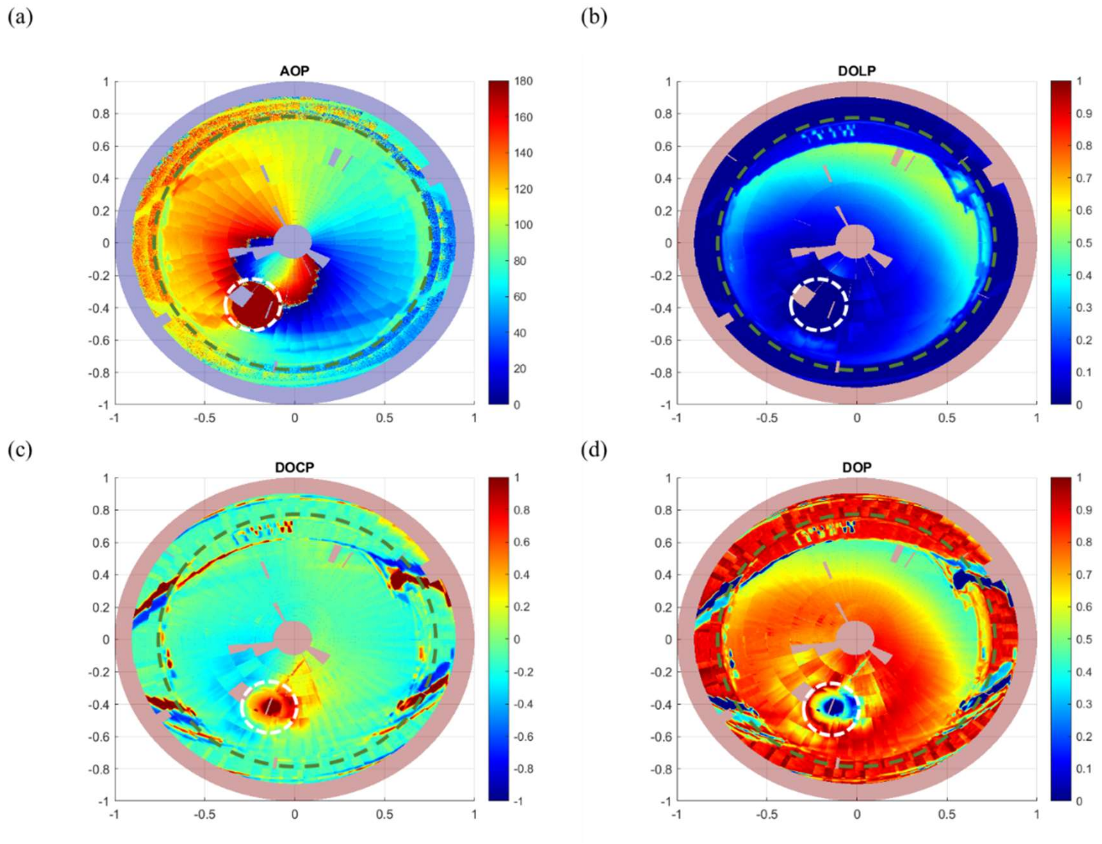

Figure 5.9: Underwater polarization mapping in swimming pool. (a) AOP, (b) DOLP, (c) DOCP, and (d) DOP image mapping. White circles indicate the locations of the sun. The Snell's window is indicated with a dark green dashed circle.

Figure 5.9 shows the full Stokes polarization mapping of the clear sky. Similar to the sky polarization mapping in section 5.3, we observed an asymmetric AOP pattern near the solar meridian inside and outside the Snell's window (Figure 5.9(a)). Increasing DOLP and DOP values are observed as azimuth angles become away from the solar meridian, as shown in Figure 5.9 (b) and Figure 5.9(d). As for DOCP patterns, we expect close-to-zero DOCP value due to the lack of the Mie scattering in the clear water. However, the measured DOCP pattern shown in Figure 5.9(c) shows clear DOCP values nearby the sun location, the source of DOCP could come from light scattered by the surrounding objects and buildings nearby the swimming pool. Another factor is the sun light direction incidence, causing over exposure issues even with minimum exposure. Therefore, large DOCP mapping should be considered as noises and be removed from the mapping.

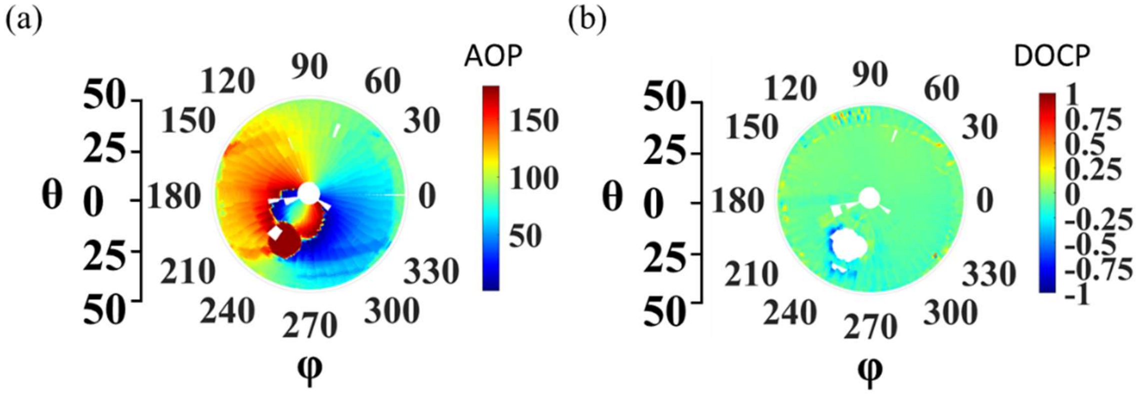

Figure 5.10: Underwater polarization mapping in swimming pool with high DOCP locations removed. (a) AOP. (b) DOCP. (Acknowledged Md Zubair Rafique for plotting mapping figures with over-exposure removed)

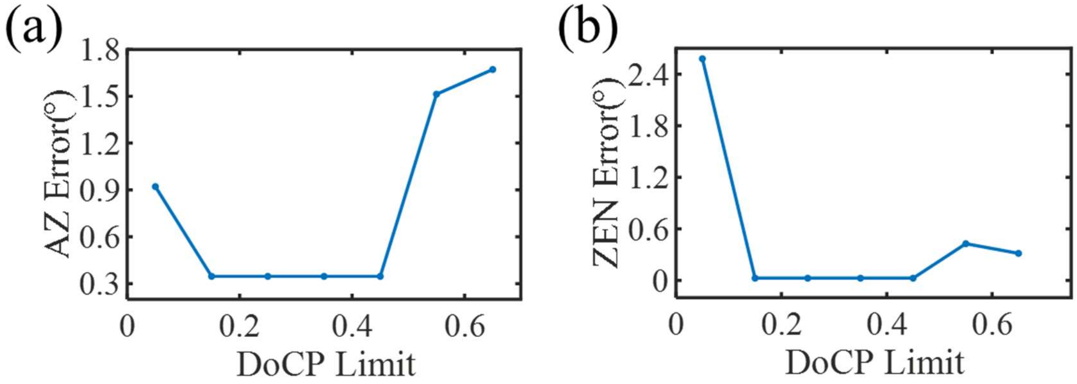

Figure 5.11: Solar tracking accuracy by setting different DOCP limits. (Acknowledged Md Zubair Rafique for data processing and analyzing the solar tracking)

Polarization mapping after the overexposure region being removed is shown in Figure 5.10. A summary of solar tracking based on data after high DOCP values are removed is shown in Figures 5.11(a) and 5.11(b), which corresponds to the tracking error of the Azimuth angle and Zenith angle of sun location, respectively. It is seen that when removing mappings with DoCP over 0.45, solar tracking error is high for both azimuth and zenith angles. When lowering the DoCP threshold down to 0.15~0.4, the azimuth angle tracking error is less than 0.4°, and the zenith angle tracking error is close to 0. However, it is seen that when setting the DOCP threshold too low (<0.15), solar tracking error increases again. This is because too much data is being removed, so the analysis becomes inaccurate due to insufficient data amount.

5.5. Polarization Imaging of Objects through Turbid Water

Another interesting application of polarization imaging is enhancing the imaging contrast of objects under the water, especially turbid water containing organic pollutants and sands. In this section, we apply the CMOS LP and CP polarization imaging camera to inspect different types of objects through turbid water.

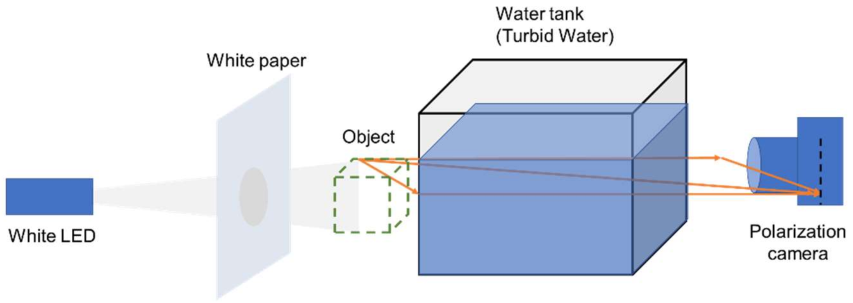

Figure 5.12: Polarization imaging of sunglasses through turbid water.

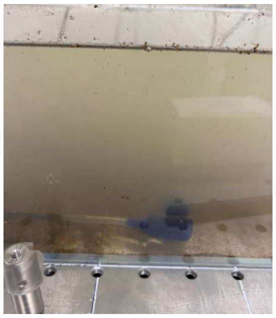

Figure 5.13: Side view of the water tank after adding the milk and sand.

The experimental setup is shown in Figure 5.12; 8L of clean water was first poured into the water tank, followed by a mixture of around 100mL milk and 50g sands to make the water turbid. The turbidity of the water body is shown in Figure 5.13.

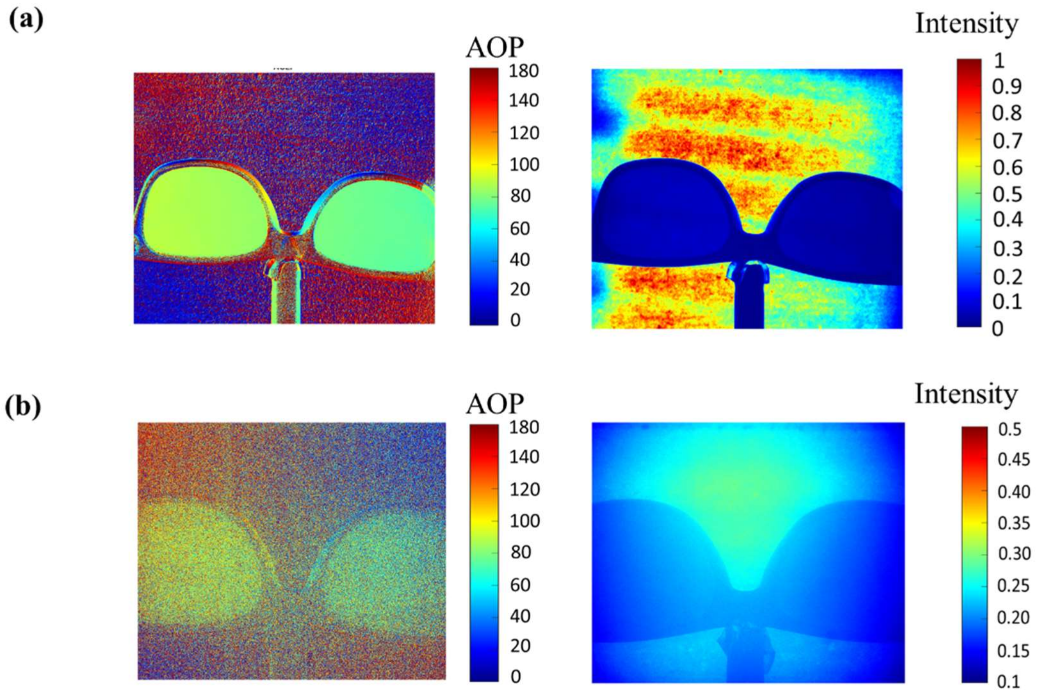

Figure 5.14: Polarization imaging of sunglasses through the turbid water.

A sunglass is positioned at the opposite side of the water tank. The polarization image of sunglass was taken without the water tank for comparison, as shown in Figure 5.14(a); both the AOP image and normalized intensity image show a clear contrast between the glass frame and glass piece. When imaged through the turbid water, the contrast between the glass frame and the glass piece is lost completely, while the AOP image still preserves this feature information, as shown in Figure 5.14(b). This indicates that the polarization information of the sunglass still keeps under an ambient environment.

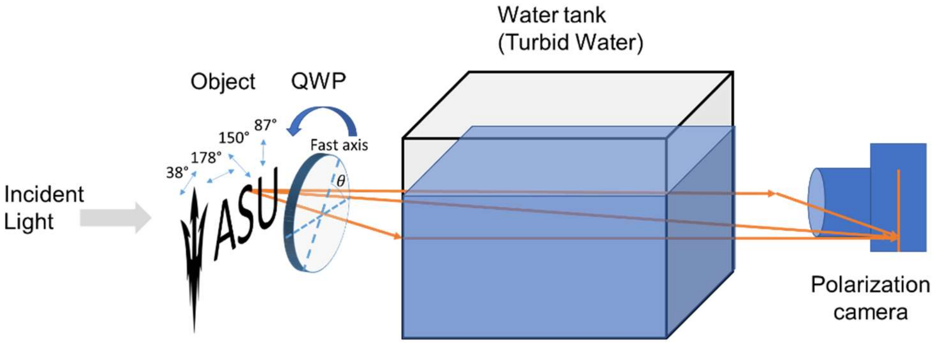

Figure 5.15: Polarization imaging of the 'ASU' letter through the turbid water.

We then exam the polarization imaging of the same object with controlled polarization information. The experimental setup is shown in Figure 5.15. An LP 'ASU' letter is positioned at the focal point with a white unpolarized LED light source positioned behind. The description of the object "ASU" letter has been discussed in detail in chapter 3. A QWP is positioned between the 'ASU letter and the polarization camera to convert the transmitted LP light into elliptically polarized light (EPL). An LP CMOS polarization camera and a CP CMOS polarization camera are positioned at the same position to image the DOLP and DOCP images, respectively. The camera setting is discussed in detail in section 5.2.

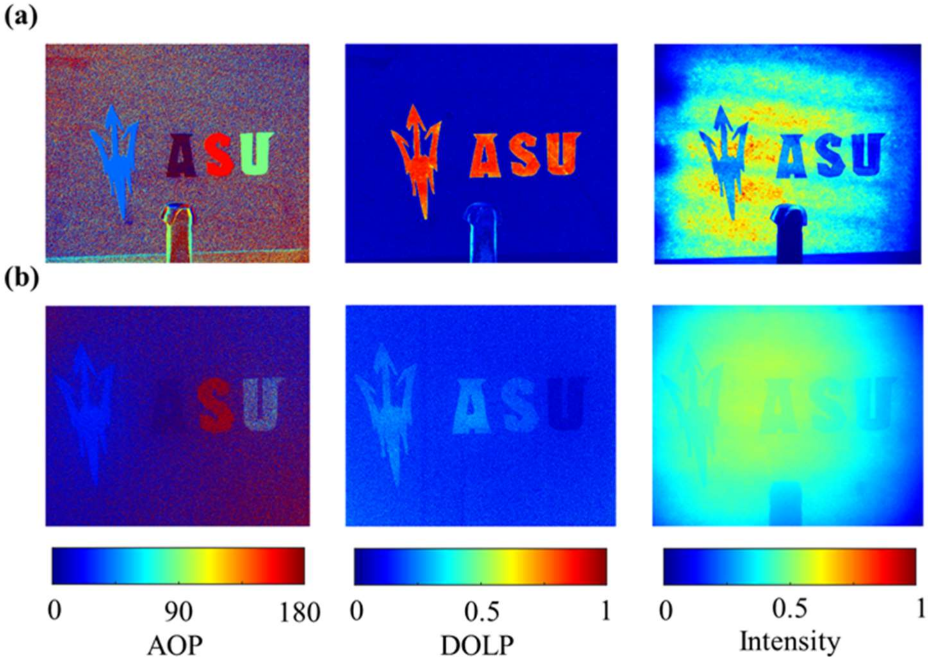

Figure 5.16: Polarization image of "ASU" letter without QWP attachment. Images were taken by an LP CMOS polarization camera. (a) Taken in the air. (b). Taken through turbid water.

Figure 5.16(a) shows the polarization image of the "ASU" letter taken in the air; in this case, no QWP was attached. Thus, DOLP images of the "ASU" letter are close to 1, indicating it is highly linearly polarized. Both the intensity and polarization image shows good contrast of the letters. Figure 5.14(b) shows the polarization image of the "ASU" letter taken through the turbid water; the intensity image of letters 'A', and'S' shows low contrast; this is because of the backscattering of the light, which causes a strong veiling effect[88]. Nevertheless, it is clear that the difference of letters is still well preserved in

DOLP images, although the DOLP value was greatly decreased due to multiple backscattering of the water body.

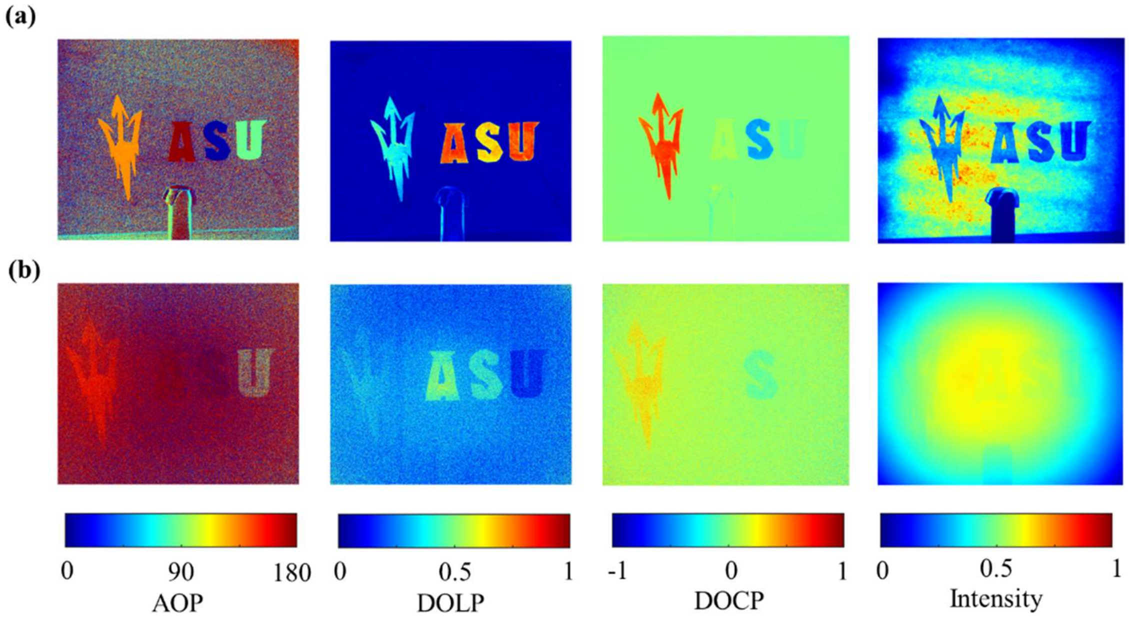

Figure 5.17: Polarization image of "ASU" letter with QWP attachment. Images were taken by a CP CMOS polarization camera. (a) Taken in the air. (b). Taken through turbid water.

Next, a QWP with a fast axis positioned at 90° is attached to the letter; in this case, the transmitted LP light is converted to EPL. The polarization image of the letter in the air is shown in Figure 5.16(a); the DOLP and DOCP images were taken by LP and CP CMOS polarization cameras, respectively. The "fork" letter shows high DOCP and lowers DOLP, indicating the EPL conversion, while 'A' 'S' letter converted into EPL with small ellipticity with a major polarization axis rotated, as shown in DOLP and AOP images, respectively. Still, the intensity and polarization images both preserves the clear contrast of letters. Figure 5.15(b) shows the polarization images taken through the turbid water. Both "fork" and 'S' letter shows clear contrast to turbid water body, which is almost unpolarized. 'A' and 'S' letter shows a higher value in DOLP, of ~0.4 to 0.5, which is 2 times higher than DOLP images taken without QWP, indicating either EPL helps improve the preservation of polarization information or the polarization contrast is dependent on polarization axis and needs to be further investigated.

5.6. Polarization Imaging of Dendritic Particles

Dendritic silver nanoparticles (AgNPs) are a type of fractal-shaped conjugated metallic particles that can be fabricated via electrochemical[89], photochemical[90], organic reducing agents[91, 92] methods, etc. Its porous and metallic material property of Ag dendrites determines it is highly optically scattering and absorptive. Thus, it can be applied as a plasmonic sensor for chemical sensing[93] and chemical catalysis[94]. Since the growth process of AgNPs dendrite follows random Brownian motion, the fracture shape of formed Ag dendrites is intrinsically unclonable[90]; the unique topological characteristics of Ag dendrites make them an ideal physical tag for anti-counterfeiting[90, 95]. Though promising, applying the unique material property of Ag dendrites for anti-counterfeiting has not yet been discussed.

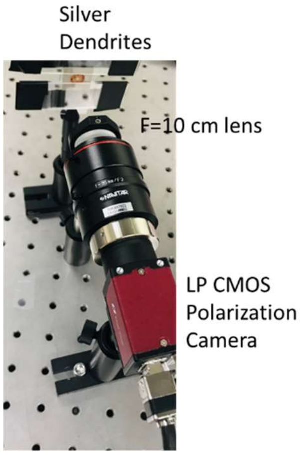

Figure 5. 18: Experimental setup of the polarization imaging of silver dendrites.

In this section, we apply the LP CMOS polarization camera to inspect the polarization characteristics of the Ag dendrites. Figure 5.18 shows the experimental setup for imaging the silver dendrites in air. An F=100mm achromatic lens is added in front of the camera to increase the image magnification by twice. The dendrites were then taken at room light, which is unpolarized.

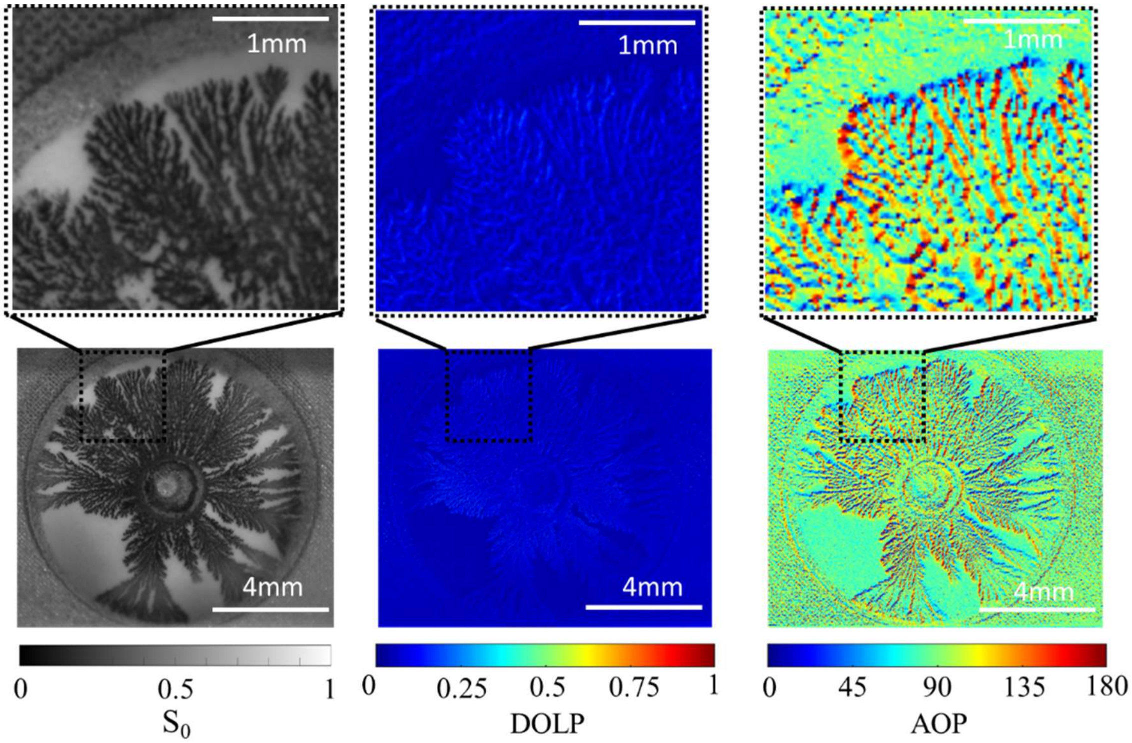

Figure 5.19: Polarization image of silver dendrites.

Figure 5.19 shows the polarization image of the silver dendrites. The insets show the zoomed-in images. The dendrites appear darkish in intensity image (S0) because Ag dendrites are highly porous, leading to a strong optical absorption due to the scattering of metal particles. The DOLP image of the dendrites shows a pseudo-3D shape of the branch, as the edge of the dendrites shows a higher DOLP of 0.15 and lower at the center (<0.1), leading to a shading effect visually. This is because the edge of the dendrites tends to have less discontinuity of metal particles, leading to a stronger scattering than the connected metals positioned at the branch center. A strong contrast between the branch edge and the center is also shown in the AOP values; the left side of the branches tends to have AOP values around 150 while the right side of the branch tends to have AOP values of 30 to 45, such a big difference in AOP values is because of the Mie scattering angle difference, causing a rather different AOP at scattered light[96].

5.7. Conclusion and Outlook

This chapter demonstrates several polarization imaging applications based on LP and CP CMOS polarization imaging cameras. Firstly, we presented a dual-camera full-stokes underwater polarization imaging system capable of automatically imaging the whole sky with variable exposer time, high accuracy, high repeatability, and high signal-to-noise ratio (SNR). Polarization mapping of clear sky and clear water is demonstrated, with help from DOCP noise analysis. The solar tracking error is reduced to less than 0.4° in azimuth angles and close to 0° for the zenith angle.

We then performed imaging of objects with polarization information through turbid water; the polarization information of sunglasses and "ASU" letters can maintain its contrast much better than intensity images. Finally, we imaged silver dendrites with an LP CMOS polarization camera, and a pseudo-3D-shaped branch was observed due to the Mie scattering of metallic particles of silver dendrites.

More importantly, our metasurface-based full Stokes polarimetric imaging sensor mentioned in chapter 3 can also be applied to the applications discussed above, especially for the underwater navigation system, as it requires high detection accuracy. Our polarimetric imaging sensor can not only fulfill the requirements but also make the system much more compact, thanks to the mini-size of the sensor developed.

CHAPTER 6

COMPACT MUELLER MATRIX MICROSCOPE BASED ON CHIP-INTEGRATED FULL-STOKES POLARIMETRIC IMAGING SENSOR

Polarization techniques have been widely used to inspect sample material scattering, optical birefringence, etc. [97]. Among them, the Mueller matrix microscope (MMM) has distinctive advantages as it quantitatively provides abundant polarization information of specimens, such as linear retardance and depolarization, etc. Therefore, MMM is often preferred when observing complex media in biomedical and clinical research [2]. However, most existing MMMs only operate in a single mode with narrow operation bandwidth and require bulky rotating retarders for polarization state analyzers (PSA) [98]. In this chapter, we report a compact, dual-wavelength and dual-working mode polarization microscope and MMM with satisfactory Mueller matrix (MM) measurement accuracy (measurement error$\leq$ 2.1%) based on chip-integrated metasurface-based full Stokes polarimetric imaging sensor (MPIS). We then applied Mueller matrix polar decomposition (MMPD) to extract optical birefringence of Honeybee wing veins, Human Lung tissues, Si metasurface and depolarization of silver dendritic particles. Our MMM is compact and versatile in its functionality, promising various applications in industry surveillance and biomedical imaging.

6.1. Introduction

Polarization microscopy (PM) can reveal the unique microscale features of specimens due to scattering, emission, birefringence, etc. Therefore, PM has been widely applied in industrial inspections[5], biomedical imaging[2], and chemical analysis[99]. Though highly useful, one of PM's major limits is that it evaluates sample polarization properties qualitatively because PM reveals only part of the polarization information. MMM can be treated as an upgrade of PM because it can quantitatively determine the MM of sample, which naturally contains comprehensive polarization information of specimens, such as depolarization, linear birefringence, linear diattenuation, etc. [24]. In practice, applying MMM or both MMM and PM is often preferred in many applications involving the inspection of complex media such as biological tissues [100].

Most of the non-polarizing microscope or imaging setups can be modified for MM measurement by adding a polarization states generator (PSG) and PSA appropriately. These modification approaches generally can be summarized into several categories according to the types of experimental approach for obtaining MM: division of time (DoT), division of amplitude (DoA), and division of focal plane (DoFP). Among them, DoT-based methods are the most common approach, in which PSGs and PSAs are achieved by dual rotating retarders (DRR)[101-105], photoelastic modulators (PEM) [106, 107], and liquid crystal retarders(LCR)[108, 109], etc. MM calculated by DRRs or LCRs method can achieve high accuracy MM image after systematic calibration. However, image number N≥16 is required to obtain full MM for sufficient noise-to-ratio, which fundamentally limits its measurement speed[104, 108]. Some of LCRs are based on organic materials, which have stability issues. PEM has demonstrated high-speed MM detection by leveraging the advantage of its high modulation speed. Yet, implementing PEM on MM imaging is more difficult as it requires complex demodulation. On the other hand, DoA based MM measurement setup divides a high-frequency laser beam reflected off the sample into four photodetectors, MM can be obtained at tens of µS after systematic calibration. However, such measurement setup requires complex optical components, and operation bandwidth is limited due to narrow laser bandwidth. Recently, a DoFP approach applying PSAs based on DoFP LP cameras and rotating retarders for PSGs has been demonstrated for full MM characterization[110] and partial MM measurement[111]. During measurement, a DoFP polarimeter integrated with a microscale LP filters array was applied for LP detection. For full MM characterization, another DoFP LP camera integrated with a fixed retarder is added for CP detection. The advantage of such a DoFP approach over other techniques is it only requires image number N≥4 for full MM measurement and no rotating components, thus the measurement setup is more compact, stable and measurement speed is higher.

In this chapter, we present a compact, dual mode, dual operation wavelength MMM based on MPIS (MPIS-MMM). MPIS is a full Stokes DoFP polarimeter working at red

(630 to 670nm) and cyan color (480 to 520nmnm), enabling CP and LP imaging simultaneously at a single snapshot. Therefore, it does not require another camera for full MM measurement, making our system much more compact compared to the dual DoFP LP camera conFigureuration[110]. To improve the measurement accuracy, we measured the MM of the beam splitter in reflection mode as well as the instrument matrix of the system at both reflection and transmission mode to achieve high polarization state measurement accuracy (averaged Stokes parameter measurement error < 4% at all modes and colors). After calibration, the measurement accuracy of MM is verified by measuring the MM of linear polarizers (average MM measurement error <2.1% at transmission mode). We then applied our MPIS-MMM to inspect Si metasurfaces, and silver dendrites, and Honeybee wing veins, Human Lung tissues to demonstrate the potential of our system. The advantages of our MPIS-MMM can be summarized in several folds: Firstly, our MMM is based on MPIS, which is compact in size for full Stokes polarization imaging. Secondly, our MMM can be operated at both reflection and transmission modes, allowing for a much broader range of applications compared to a single working mode. Thirdly, our system provides high MM measurement accuracy and high full Stokes polarization detection after calibration. MPIS-MMM proposed in this paper can be applied for numerous applications, such as industrial inspection, biological and clinical research, optical characterizations of novel photonic devices, etc.

6.2. System Concept

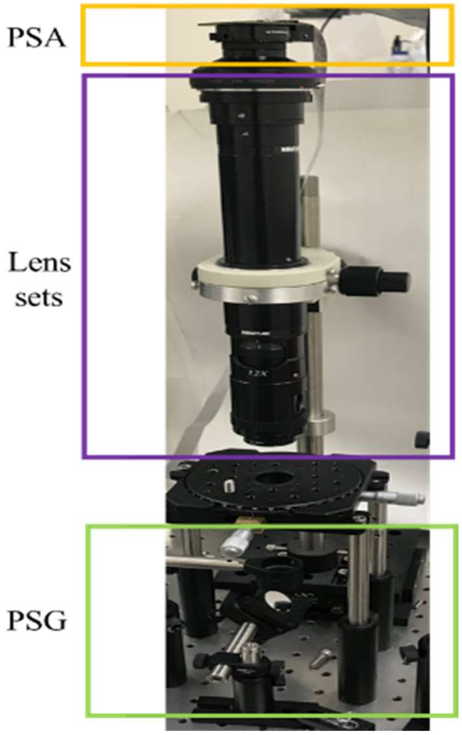

Figure 6.1: Photograph of Mueller matrix microscope showing polarization state generator (PSG) in transmission mode, lens sets, and full Stokes polarimetric CMOS imaging sensor as polarization state analyzer (PSA).

In this section, we demonstrate a chip-integrated metasurface-based full Stokes polarimetric imaging sensor (MPIS) based MMM (MPIS-MMM), which is compact in polarization imaging. It is established by adding LPs and rotating QWPs as PSG and MPIS as PSA onto a commercial Zoom lens system for machine vision (MVL12X12Z, etc., Thorlabs Co. Ltd., USA), as shown in Figure 6.1.

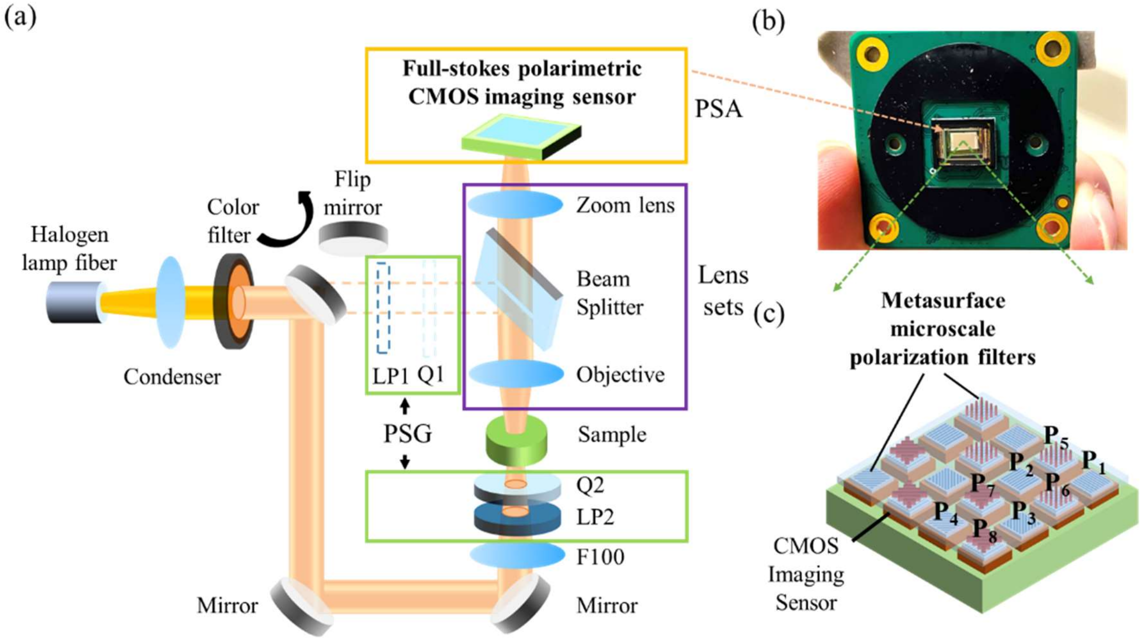

Figure 6.2: Schematic of Mueller matrix microscope and chip-integrated polarimetric CMOS imaging sensor. (a) Illustration of the optical path of Mueller matrix microscope, here LP1, and LP2 represent linear polarizer (LP), and Q1, Q2 represents QWPs. (b,c) Image and schematic of chip-integrated metasurface-based full Stokes polarimetric imaging sensor (MPIS). P_1-P_4 denotes the microscale LP filters with transmission axes at 0° 90° 45° 135°, respectively. P_5, P_7 and P_6, P_8 denote microscale chiral metasurfaces transmitting right-handed circularly polarized light (RCP) and left-handed circularly polarized light (LCP), respectively.

Figure 6.2(a) illustrates the complete optical path of MPIS-MMM. Light from mercury lamp fiber is firstly collimated by a condenser and filtered by bandpass filters with 40nm spectral bandwidth centered at 650 and 500nm, respectively. Then the collimated light is guided into either transmission or reflection light path at will by a flip mirror and modulated by PSG to generate fully polarized light with arbitrary polarization states. The incoming polarized light is then focused onto specimen by an achromatic lens (F=100) or ×2 objective lens in transmission and reflection mode respectively. Light transmitted through or reflected off the specimen is then collected by Zoom lens system with tunable magnification (×1.16 to ×28) and is imaged by MPIS. Here, MPIS is a division of a focal plane (DoFP) based full Stokes polarimeter composed of 336×224 microscale subwavelength metasurfaces polarization filter array (MPFA) integrated into a commercial CMOS imaging sensor (IMX477). Figure 6.2(b) shows the photo of MPIS, the whole imaging sensor (including PCB board) is less than 4×4 cm^2, which is ultra-compact in size. Figure 6.2(c) shows the 3D illustration of the MPIS, which consisted of over 9400 super-pixels. Each super-pixels contain two pairs of metasurface circular polarization (CP) filters (P_5, P_6 and P_7, P_8) and four linear polarization (LP) filters (P_1 to P_4) for full Stokes polarization states analyzation at a single snapshot. The corresponding field of view and microscopic imaging resolution are 1.16mm×0.82mm, 3.66μm at lowest magnification (×1.16). and 96 μm×67.9 μm, 0.83 μm at the highest magnification (×28). Here 0.83 μm is limited mainly by the highest numerical aperture (0.202) of Zoom lens system can achieve. The full Mueller matrix (MM) of samples can be obtained when combined MPIS with PSG after $N \geq 4$ measurements[110].

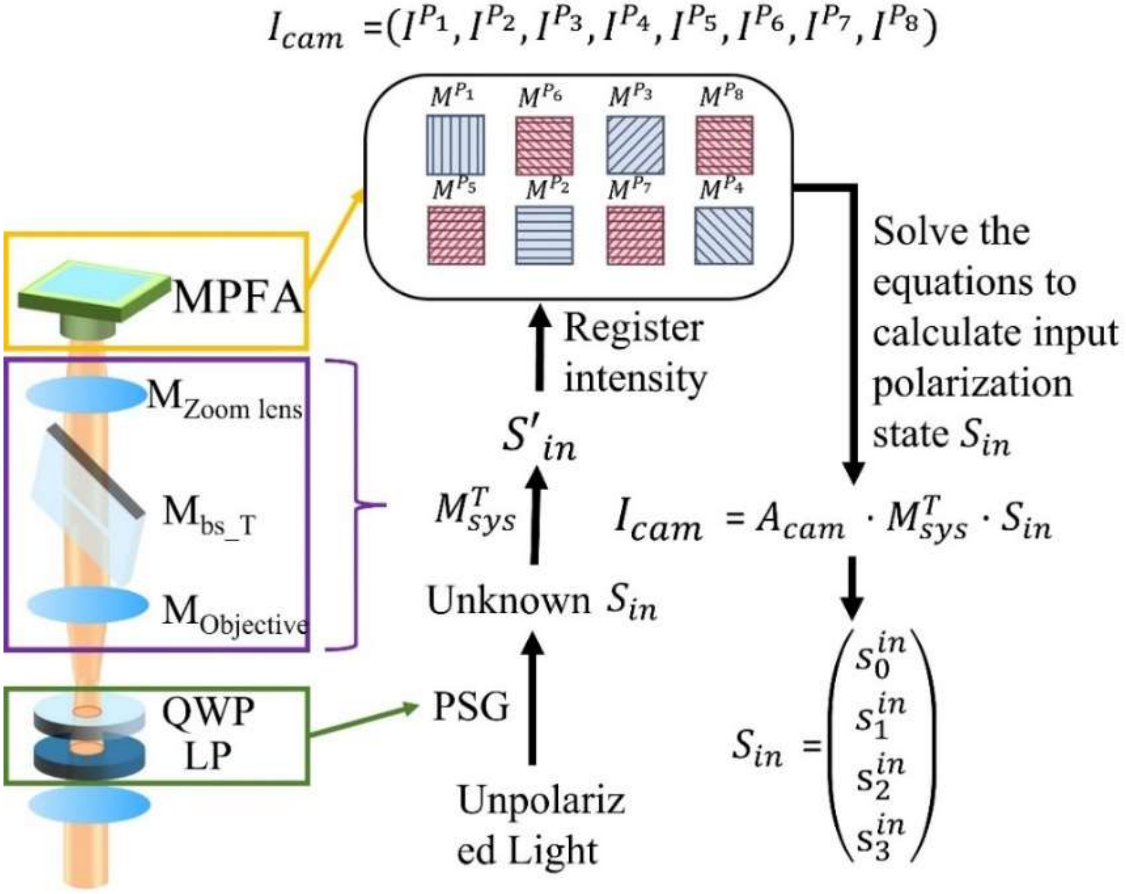

Figure 6.3: Flowchart of full Stokes polarization detection at transmission mode based on instrument matrix method. Light transmitted through the specimen with unknown

polarization states can be measured by MPFA. Then based on the instrument matrix of MPFA and MM of the Zoom lens system, we can calculate the input polarization states.

Traditional polarization microscopes often apply PSAs with LP and CP filters for full Stokes parameters detection using the direct subtraction method:

$$S_0 = I_0 + I_{90} = I_{45} + I_{135} = I_{RCP} + I_{LCP} \tag{6.1}$$

$$S_1 = I_0 - I_{90} \tag{6.2}$$

$$S_3 = I_{45} - I_{135} \tag{6.3}$$

$$S_3 = I_{RCP} - I_{LCP} \tag{6.4}$$

Where I_0 , I_{45} , I_{90} , I_{135} , I_{RCP} , I_{LCP} denotes intensity of light transmitting through LPs with azimuth angles along 0°, 45°, 90°, 135° and RCP, LCP filters. The measurement accuracy achieved by such method is normally limited by the extinction ratio (ER) of PSA. Moreover, the polarization aberration introduced by the optical components in the optical path is often ignored, leading to a further decrease in polarization state detection accuracy. To address those issues, we first go through a calibration procedure to obtain the instrument matrix [41, 68] of the polarization microscope, denoted as A_{PSA}^{T} in transmission mode and A_{PSA}^{R} in reflection mode. In addition, MM M_{PSG}^{R} of components between the sample and PSG in reflection mode is also measured. The advantage of such calibration process is it accounts for both limited ER of the PSA and the polarization aberration of the optical path, thus the measurement accuracy after calibration can be greatly improved [41, 68].

The flow chart for measuring the unknown polarization states at transmission mode based on system instrument matrix is shown in Figure 6.3. Unknown polarization states $S_{in} = \left(S_0^{in}, S_1^{in}, S_2^{in}, S_3^{in}\right)$ generated by PSG firstly gets modified to S'_{in} due to polarization aberration introduced by beam splitter and Zoom lens system according to Fresnel equations, this process can be written as:

$$S'_{in} = M_{zoom\_lens} \cdot M_{bs\_T} \cdot M_{Objective} \cdot S_{in} = M_{PSA}^{T} \cdot S_{in} \tag{6.5}$$

where $M_{Objective}$ is the MM of 2.0× magnifying lens attachment (MVL12X20L), M_{bs_T} is MM of beam splitter at transmission mode and M_{zoom_lens} is the MM of Zoom lens and extension tube. M_{PSA}^{T} represents combined MM of the three modules menteiond above. The relationship between transmitted light intensity vector I_{cam} =$(I^{P_1}, I^{P_2}, I^{P_3}, I^{P_4}, I^{P_5}, I^{P_6}, I^{P_7}, I^{P_8})$ recorded by 8 polarization filters of MPFA and unknown input polarization state $S_{in} = \left(s_0^{in}, s_1^{in}, s_2^{in}, s_3^{in}\right)$ can then be written as the equation below.

$$\begin{pmatrix} I^{P_1} \\ I^{P_2} \\ I^{P_3} \\ I^{P_4} \\ I^{P_5} \\ I^{P_6} \\ I^{P_7} \\ I^{P_8} \end{pmatrix} = I_{cam} = A_{cam,8\times4} \cdot M_{PSA}^{T} \cdot \begin{pmatrix} s_0^{in} \\ s_1^{in} \\ s_2^{in} \\ s_3^{in} \end{pmatrix} \tag{6.6}$$

Where M_{PSA}^{T} is the MM accounting for the polarization effect of the optical path in transmission mode, including beam splitter and zoom lens system, $A_{cam,8\times4}$ is the instrument matrix of one super-pixel of MPIS, which includes 8 polarization filters for detecting linearly polarized light (LPL) and circularly polarized light (CPL):

$$A_{cam,8\times4} = \begin{bmatrix} M_{00}^{P_1} & M_{01}^{P_1} & M_{02}^{P_1} & M_{03}^{P_1} \\ M_{00}^{P_2} & M_{01}^{P_2} & M_{02}^{P_1} & M_{03}^{P_1} \\ M_{00}^{P_3} & M_{01}^{P_3} & M_{02}^{P_3} & M_{03}^{P_4} \\ M_{00}^{P_4} & M_{01}^{P_4} & M_{02}^{P_4} & M_{03}^{P_4} \\ M_{00}^{P_5} & M_{01}^{P_5} & M_{02}^{P_5} & M_{03}^{P_5} \\ M_{00}^{P_6} & M_{01}^{P_6} & M_{02}^{P_6} & M_{03}^{P_6} \\ M_{00}^{P_7} & M_{01}^{P_7} & M_{02}^{P_7} & M_{03}^{P_7} \\ M_{00}^{P_8} & M_{01}^{P_8} & M_{02}^{P_8} & M_{03}^{P_8} \end{bmatrix} \tag{6.7}$$

For simplicity, the instrument matrix of MMM in transmission mode can then be written as A_{PSA}^{T}:

$$A_{PSA}^{T} = A_{cam,8\times4} \cdot M_{PSA}^{T} \tag{6.8}$$

During the calibration process, we first characterized 10 polarization states $S_{4\times10}^{in}$ generated by PSG using a PSA and register their corresponding MPFA transmitted intensity matrix $I_{8\times10}^{in}$. A_{PSA}^{T} is then obtained by solving the equation $I_{8\times10}^{in} = A_{PSA}^{T} \cdot S_{4\times10}^{in}$. After calibration, the unknown input polarization states can then be calculated using the equation:

$$S_{in} = {A_{PSA}^{T}}^{-1} \cdot I_{cam} \tag{6.9}$$

Where I_{cam} $=(I^{P_1}, I^{P_2}, I^{P_3}, I^{P_4}, I^{P_5}, I^{P_6}, I^{P_7}, I^{P_8})$ is the transmitted light intensity vector recorded by a super-pixel of MPFA as mentioned before, and $S_{in} = \left(s_0^{in}, s_1^{in}, s_2^{in}, s_3^{in}\right)$ is unknown input polarization state to be measured.

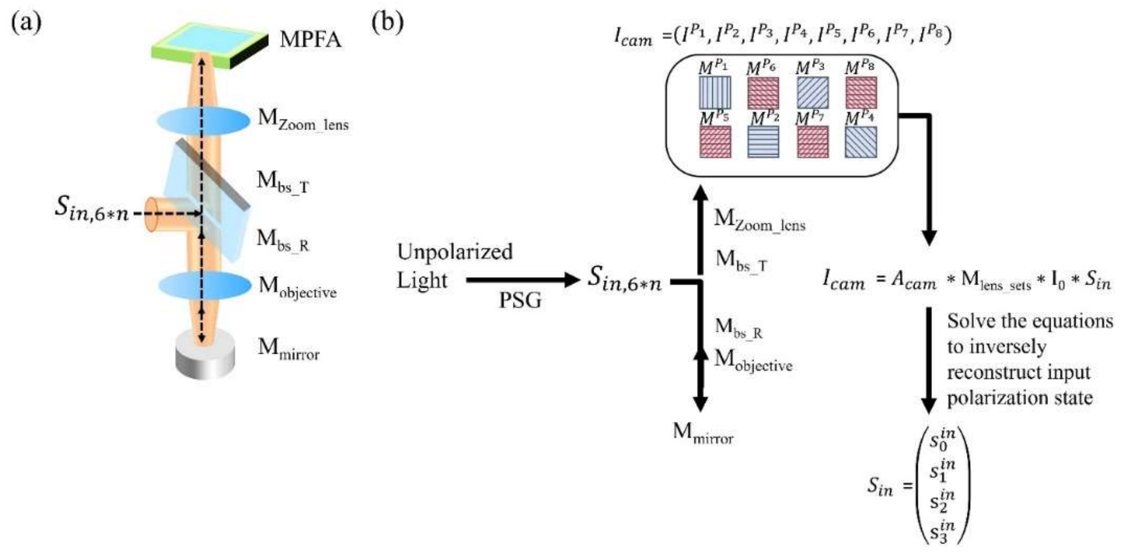

Figure 6.4: Schematic and flowchart of full-Stokes polarization detection at reflection mode based on instrument matrix method. (a). Optical path for reflection mode. (b). Flow chart for measuring unknown input polarization state in reflection mode.

Next, we demonstrate high accuracy full Stokes polarization detection and MM measurement can be achieved in reflection mode with proper calibration procedures. The flow chart of measuring unknown input polarization states S_{in} generated by PSG in reflection mode is shown in Figure 6.4. Light reflected off the mirror with unknown polarization states can be measured by MPFA. Then based on the instrument matrix of MPFA and MM of the light path, we can calculate the input polarization states. Firstly, S_{in} gets modified to S'_{in} due to reflection of beam splitter and focusing of objective, the process can be written as:

$$S'_{in} = M_{Objective} \cdot M_{bs\_R} \cdot S_{in} \tag{6.10}$$

Where M_{bs_R} denotes the MM of beam splitter in refletion mode and $M_{Objective}$ is the MM of the objective lens.

Light with polarization state S'_{in} is then reflected by the mirror and re-collected by the objective, and gets further modified to S''_{in} after transmitting through beam splitter and Zoom lens system:

$$S''_{in} = M_{zoom\_lens} \cdot M_{bs\_T} \cdot M_{Objective} \cdot M_{mirror} \cdot M_{Objective} \cdot M_{bs\_R} \cdot S_{in} \quad (6.11)$$

Where M_{mirror} is the MM of an ideal mirror, M_{bs_T} is the MM of the beam splitter in transmission mode and M_{zoom_lens} is the MM of the zoom lens system.

The relationship between the intensity vector I_{cam} recorded by MPIS and unknown polarization states S_{in} can be written as:

$$I_{cam} = A_{cam,8\times4} \cdot M_{zoom\_lens} \cdot M_{bs\_T} \cdot M_{Objective} \cdot M_{mirror} \cdot M_{Objective} \cdot M_{bs\_R} \cdot S_{in} \quad (6.12)$$

Here for simplicity, we can combine values after M_{mirror} as $A^R_{PSA} = A_{cam,8\times4} \cdot M_{zoom\_lens} \cdot M_{bs\_T} \cdot M_{Objective}$, representing the instrument matrix of PSA in reflection mode. Similarly, $M_{Objective} \cdot M_{bs\_R}$ can be combined as M^R_{PSG}, representing the polarization effects introduced before light is focused onto the specimen. The unknown input polarization states can then be calculated using the equation:

$$S_{in} = (A^R_{PSA} \cdot M_{mirror} \cdot M^R_{PSG})^{-1} \cdot I_{cam} \quad (6.13)$$

Where M_{mirror} is MM of an ideal mirror, written as a diagonal matrix $diag(1,1,-1,-1)$. A^R_{PSA} is the instrument matrix in reflection mode, M^R_{PSG} is the combined MM of the objective lens and beam splitter in reflection mode to account for the polarization effects introduced before light is focused onto the specimen.

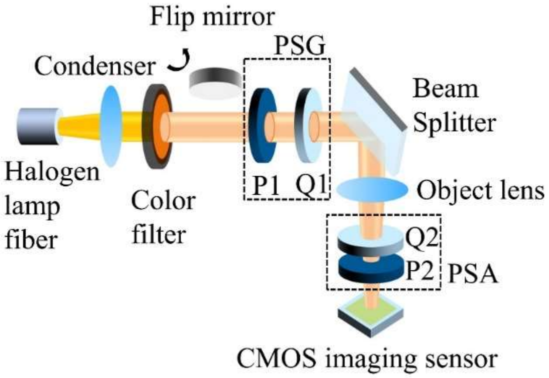

Figure 6.5: Schematic of experimental setup for measuring M_{PSG}^{R} , which describes polarization aberration before light is focused onto the sample.

To measure M_{PSG}^{R} , a PSA composed of a rotating QWP, and a LP fixed at 0° and a CMOS imaging sensor as a photo detector is applied, as shown in Figure 6.5. The measurement details are included in Appendix B. A_{PSA}^{R} can then be obtained using 10 pre-measured polarization states $S_{4\times10}^{in}$ and their corresponding intensity matrix $I_{8\times10}^{in}$ using the equation:

$$A_{PSA}^{R}=I_{8\times10}^{in}\cdot(M_{mirror}\cdot M_{PSG}^{R}\cdot S_{4\times10}^{in})^{-1} \tag{6.14}$$

After calibration, the unknown input polarization states in reflection mode can then be calculated using the equation:

$$S_{in}=(A_{PSA}^{R}\cdot M_{mirror}\cdot M_{PSG}^{R})^{-1}\cdot I_{cam} \tag{6.15}$$

Where M_{mirror} is MM of an ideal mirror, written as a diagonal matrix $diag(1,1,-1,-1)$. A_{PSA}^{R} is the instrument matrix in reflection mode, M_{PSG}^{R} is the combined MM of the objective lens and beam splitter in reflection mode to account for the polarization effects introduced before light is focused onto the specimen.

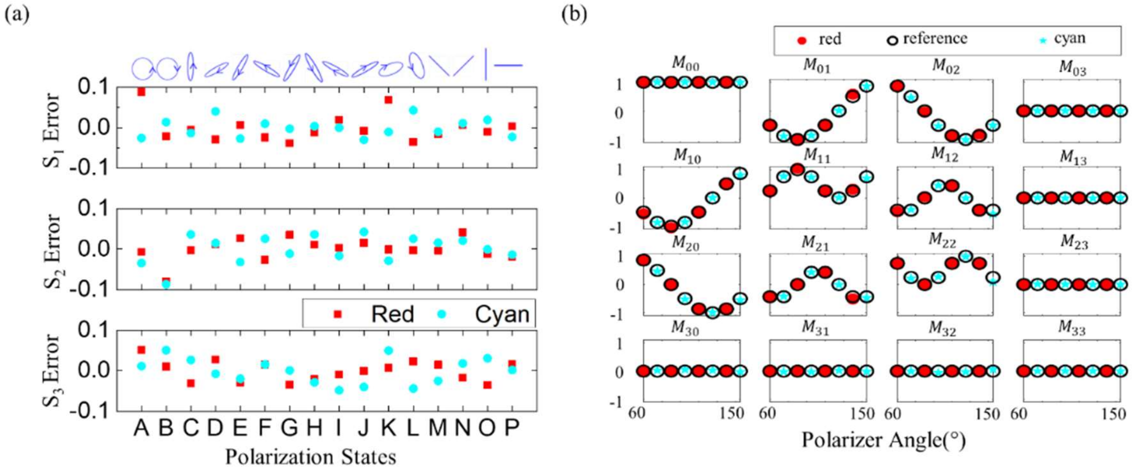

Figure 6.6: Full Stokes polarization detection of 16 arbitrary polarization states, and Mueller matrix measurement of a standard linear polarizer in transmission mode. (a) Measurement error for measuring 16 arbitrary polarization states. (b). Mueller matrix measurement of a standard linear polarizer at different polarization axis angles. Black hollowed circle: theoretical values as reference. Red circle: measured results under 630-670nm input; Cyan star: measured results under 480 to 520nmnm input.

To evaluate polarization state measurement accuracy, we measured 16 arbitrary polarization states using a PSA at red (630 to 670nm) and cyan color input (480 to 520nm), respectively (see Appendix A for more details). Figure.6.6(a) shows the Stokes parameter measurement error ΔS_i^j, defined as: $\Delta S_i^j = S_i^j - {S_R}_i^j$(i=1, 2, 3, j=1,2… 16), where S_i^j is the Stokes parameter measured by MPIS-MMM and ${S_R}_i^j$ is the Stokes parameter measured by PSA as a reference. The mean absolute error (MAE) for S_1, S_2, S_3, defined as $\overline{\Delta_s} = \frac{\sum_{j=1,}^{16}\left|\Delta S_i^j\right|}{16}$ (i=1,2,3) are 2.15%,1.85%,2.45% for red and 2.61%, 2.76%, 1.76% for cyan.

We then measured the MM of a standard commercial linear polarizer (LP) at different polarization axis angles with 15° per step at transmission mode. Detailed information about the experimental setup and methods for obtaining MM images in transmission mode is included in Materials and Methods. Figure 6.6(b) shows the comparison between the MM value taken by MPIS-MMM and the theoretical value of an ideal LP, which is in good agreement. The measurement error of each MM element is defined as $\Delta M_{ij}^{k} = M_{ij}^{k} - {M_R}_{ij}^{k}$ (i=0,1,2,3, j=0,1,2,3, k=1,2,3,4), where M_{ij}^{k} is the measured MM value of kth measurement for red color or cyan color input, respectively and ${M_R}_{ij}^{k}$ is the calculated reference. The MAE of the measured MM of LP defined as $\overline{\Delta_M} = \frac{\sum_{i=1,j=1,}^{4,4,4}\left|\Delta\ _{ij}^{k}\right|}{4\times4\times4}$ are 1.6% for red color and 2.1% for cyan color, respectively.

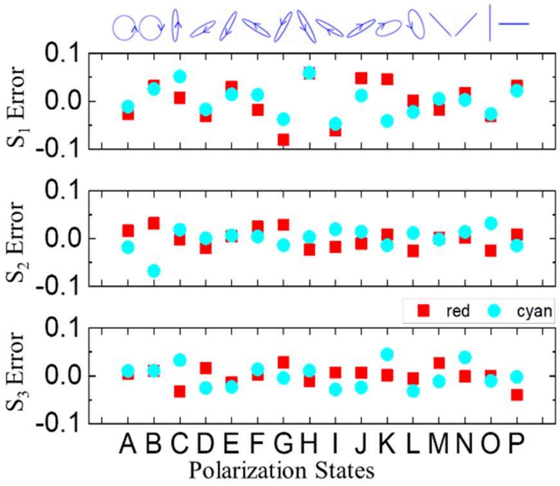

Figure 6.7: Full Stokes polarization detection of 16 arbitrary polarization states in reflection mode after system calibration.

After calibration, we again measured 16 arbitrary polarization states in reflection mode with red and cyan color input, respectively, to determine the accuracy of polarization state detection. The MAE of measurements is 1.52%,1.52%, and 3.66% for red (630 to 670nm) and 2.02%, 1.59%, and 2.56% for cyan (480 to 520nm), as shown in Figure 6.7.

6.5. Polarization and Mueller Matrix Imaging Analysis of Si Metasurface

Optical metasurfaces (OM) are optically thin artificial metamaterials capable of engineering the amplitude and phase of incoming light that are unattainable from materials existing in nature[112]. OM has advantages in a high degree of freedom in design and compatibility with cleanroom fabrication technologies, enabling novel flat optical devices with high performance and low cost for numerous applications, such as polarization control [35, 37, 38, 41], beam steering[113] and metalens[114] .etc. In this chapter, we apply MIPS-MMM to characterize subwavelength scale Si nanogratings with artificial birefringence designed for polarization control.

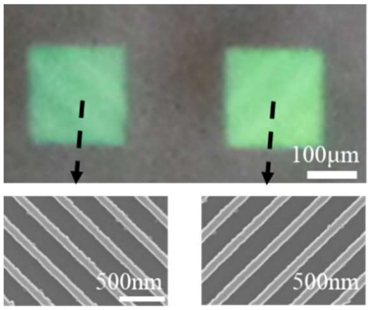

Figure 6.8: Optical microscope and scanning electron microscope (SEM) image of fabricated Si metasurface.

Microscopic and SEM images of fabricated Si nanogratings are shown in Figure 6.8. The width, period, and thickness of Si nanogratings are ~100nm, 297nm and 130nm respectively. Fabrication procedures of Si nanogratings are included in Appendix B.

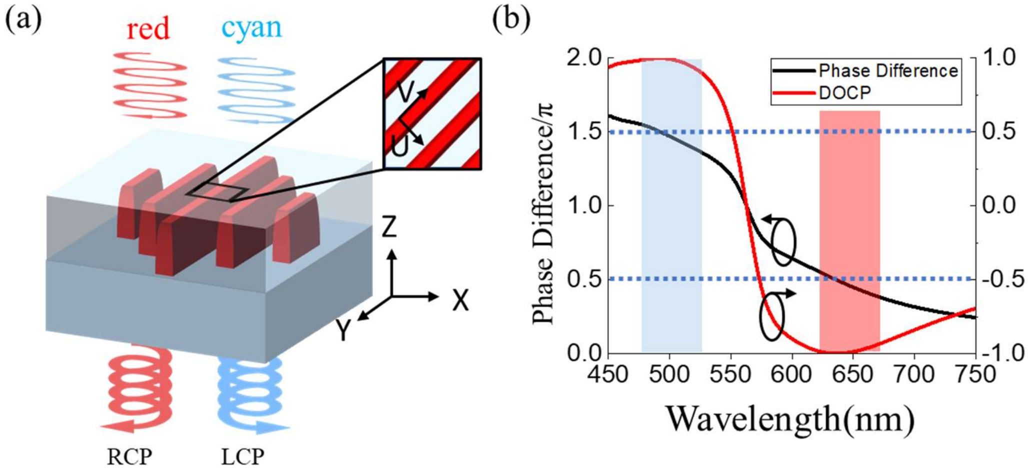

Figure 6.9: Illustration of Si metasurface and simulation of optical birefringence introduced by Si metasurface (a) 3D schematic of the Si metasurface (b) Finite-Difference Time-Domain (FDTD) simulated phase difference between fast (U) and slow(V) axes, left axis, and degree of circular polarization (DOCP) of CPL converted from 0° LPL input, right axis.

The optical function of Si nanogratings is similar to a multi-order QWP [45] consisting of a fast optical axis (U axis) and slow axis (V axis), as shown in Figure 6.9 (a). When incoming LPL is polarized at 0°, which is 45° with respect to the fast axis, the transmitted light will be converted into RCP at cyan color and LCP at red input, respectively. Opposite CP handedness conversion at red and cyan color is because the phase difference $\Delta\varphi$

between fast and slow axis are $\frac{3}{2}\pi$ at cyan color and $\frac{1}{2}\pi$ at red color, as shown in Figure 3.9 (b).

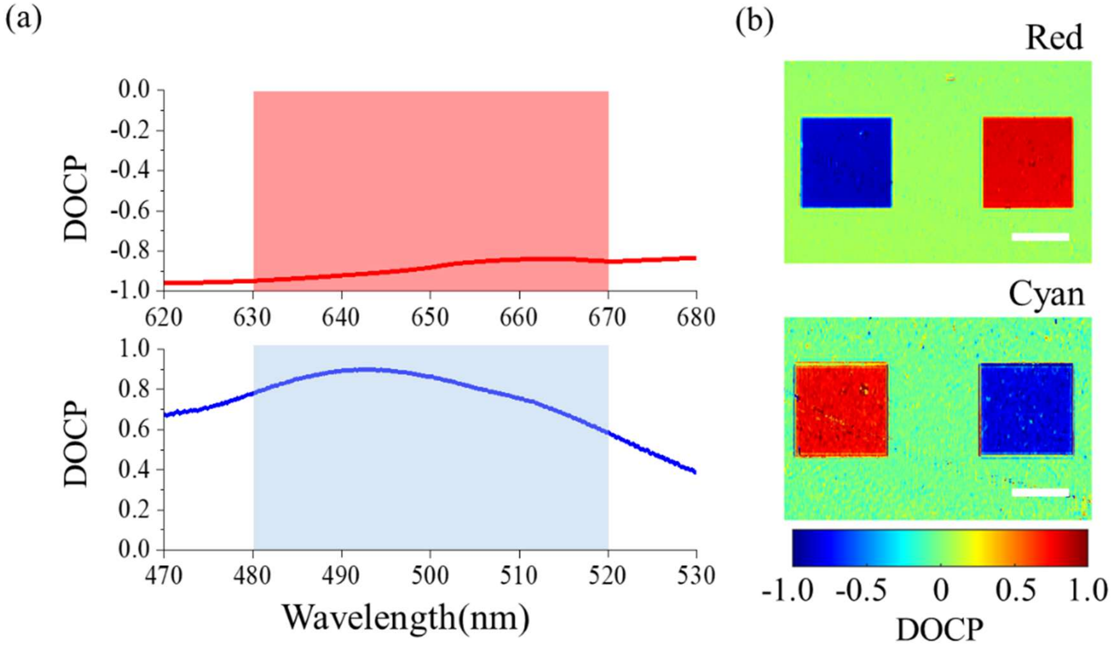

Figure 6.10: Quantitative comparison of circular polarization conversion measured by traditional PSA and MPIS-MMM. (a). Degree of circular polarization (DOCP) is measured by conventional PSA at red and cyan color (b). DOCP image measured by polarization microscopy under red and cyan color input, respectively. Scale bar: 100µm.

To evaluate measurement accuracy, we used 0° LPL as input and measured the converted DOCP of Si metasurface (device at the left side as shown in Figure.6.8) with a PSA (see Appendix C). Figure 6.10(a) shows the measured DOCP at red (630 to 670nm) and cyan (480 to 520nm), respectively. The averaged converted DOCP values at red and cyan colors are -0.885 and 0.805. Figure 6.10(b) shows the DOCP images taken by MPIS-MMM using 0° LPL as input in transmission mode. The spatially averaged DOCP values of Si nanogratings on the left side are -0.872, and 0.813, respectively, which agrees well with results measured by PSA.

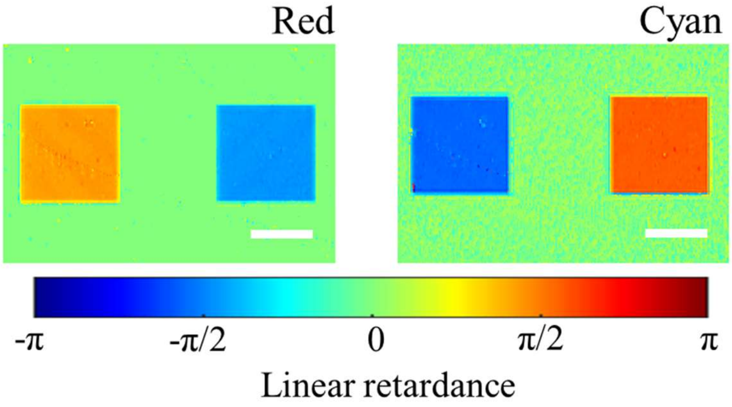

Figure 6.11: Si metasurface linear retardance image extracted from Mueller matrix under red and cyan color input, respectively. Scale bar: 100μm. Image Magnification: ×10.

Complete MM images of the Si metasurface under red and cyan color are shown in Appendix B. Figure 6.11 further shows the linear retardance image extracted from the MM of Si nanogratings by Mueller matrix polar decomposition (MMPD). The spatially averaged linear retardance of Si nanogratings on the left side is 0.436π in red color and -0.557π in cyan color. The difference in linear retardance at cyan color between results extracted from MPIS-MMM and FDTD simulation is because MM does not contain absolute phase information of light. Nevertheless, the MMM still reveals the fundamental reason Si nanograting works as a multi-order QWP.

6.6. Polarization and Mueller Matrix Imaging Analysis of Silver Dendrites

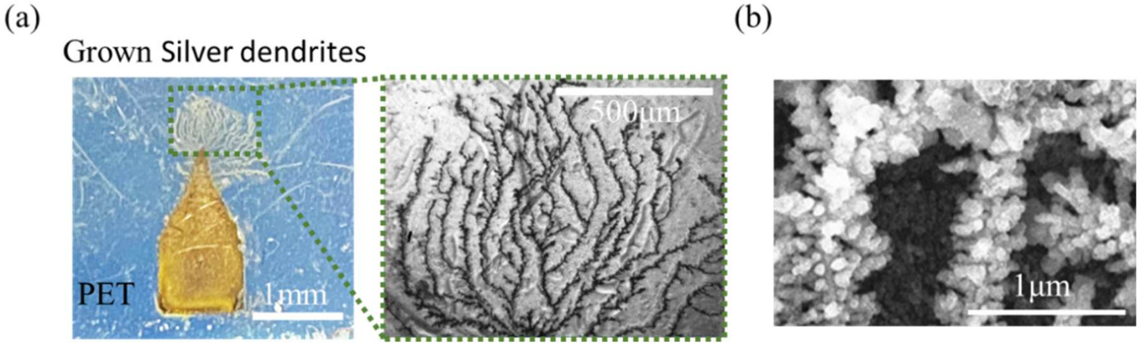

Figure 6.12: Electro-chemically grown silver dendrites. (a). Photo and microscopic image of grown silver dendrites. (b). Scanning electron microscopic (SEM) image of grown silver dendrites. (acknowledged *Dr. Michael Kozicki* for providing SEM images)

In this section, we applied MMM to inspect the material properties of Ag dendrites, an Ag dendrite grown by an electrochemical method, is shown in Figure 6.12. The conjugated Ag dendrites are typically a few µm thick, and Ag nanoparticles are ~ 30-50nm in diameter. Many empty holes exist between the Ag nanoparticles, leading to a highly porous structure.

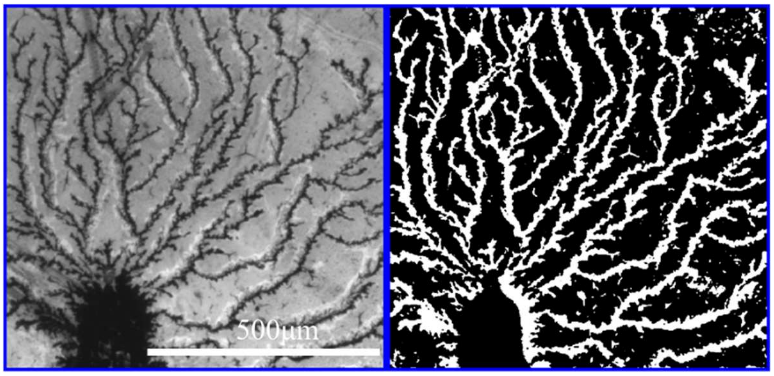

Figure 6.13: Topology duplication using image processing algorithms. Left: The original grayscale images of silver dendrites. Right: Binarized mask of silver dendrites

To reveal the unique material properties of the grown silver dendrites, we duplicated of the topology of Ag dendrites using an image processing algorithm and fabricated the silver dendrite with the same topology in a cleanroom based on UV lithography technique. The microscopic image of silver dendrites was first taken using a large field-of-view microscope (MVL12X12Z, etc., Thorlabs Co. Ltd., USA). The grayscale image is then binarized using Matlab's adaptive threshold method[114], as shown in Figure 6.13. The binarized mask was then converted into.GDSII files by open source software GDoesII[115]. Note that there are some unwanted residual particles between the branches of the dendrites, which are manually removed in the GUI panel of the layout editor.

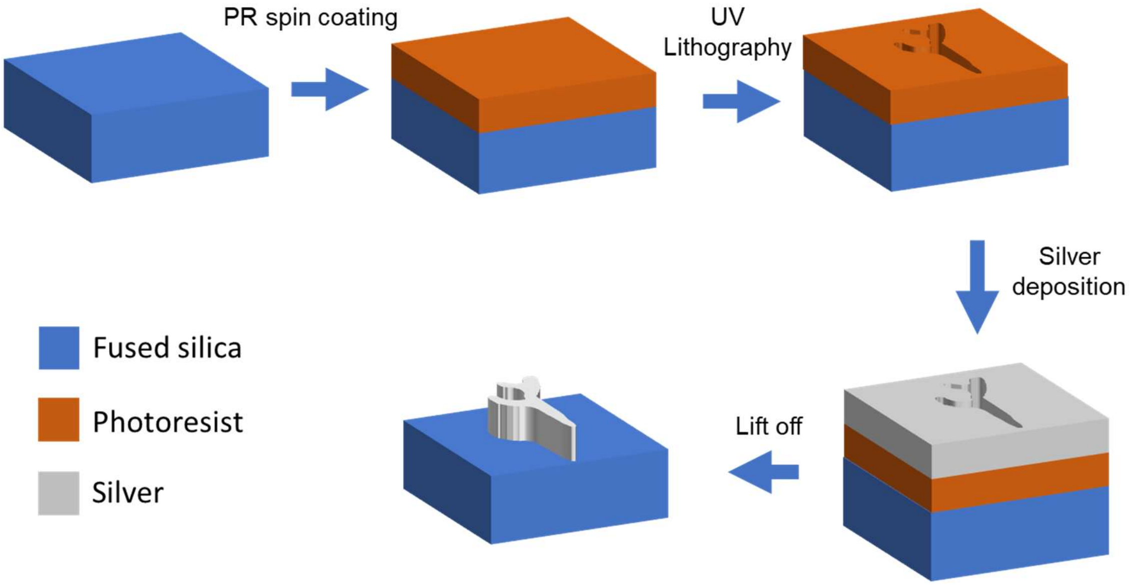

Figure 6.14: Fabrication flow chart of duplicating silver dendrites by UV lithography and metal deposition.

The fabrication process is shown in Figure 6.14. A thin layer of Photoresist was spin-coated on the fused silica substrate, then the duplicated Ag dendrite was patterned using a UV laser writer, followed by Ag thermal deposition and lift-off.

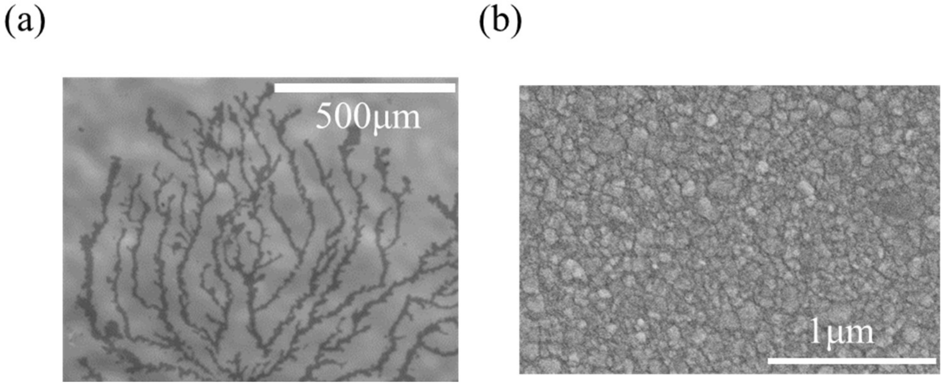

Figure 6.15: Images of duplicated silver dendrites. (a) microscopic image of duplicated silver dendrites. Sample photo is taken with an white paper under the substrate to increase contrast. (b) SEM image of duplicated silver dendrites fabricated by UV lithography.

Fabricated Ag dendrite structure is shown in Figure 6.15(a). Since the duplicated Ag dendrite is achieved by Ag thermal deposition, the formed Ag material is uniformly distributed with Ag seed size at scale of ~30-50nm, as shown in SEM image in Figure 6.15(b).

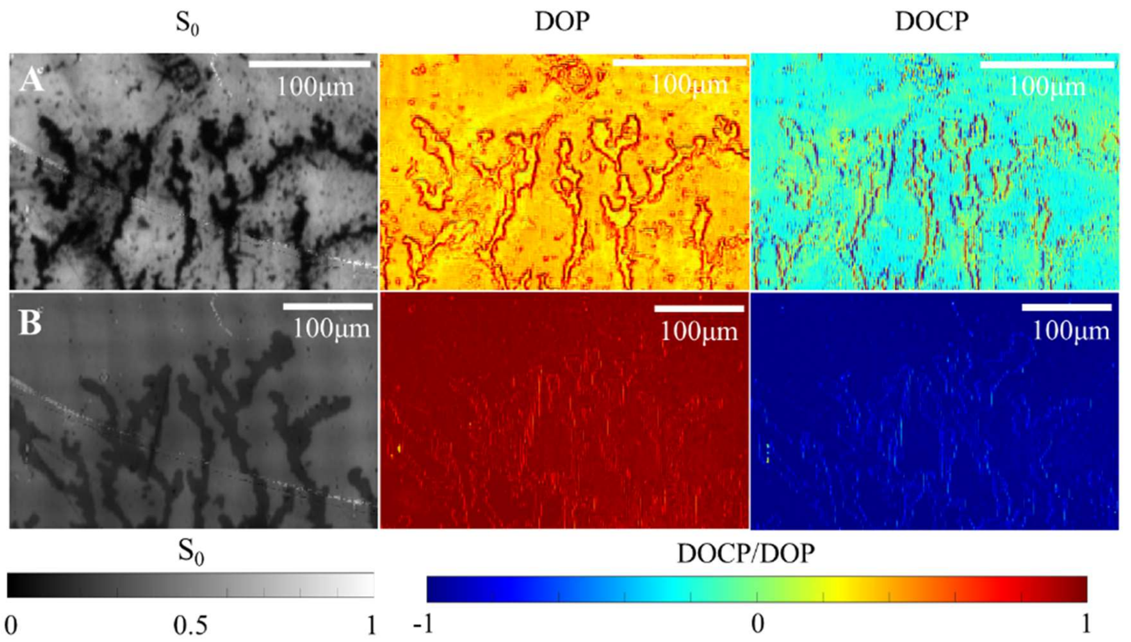

Figure 6.16: Full Stokes polarization image of grown silver dendrites and duplicated silver dendrites.

Next, we compare polarization microscope images of silver dendrites fabricated by UV lithography with electro-chemically grown. Session A corresponds to polarization image of dendrites grown on electrodes with RCP input, the grown Ag shows DOP<0.5, and low DOCP, indicating a highly depolarizing nature. On the other hand, session B corresponds to duplicated Ag dendrites, the DOP of reflected light is still close to 1 and DOCP is still close to -1, indicating the duplicated Ag dendrites acts as a mirror, which does not have much scattering.

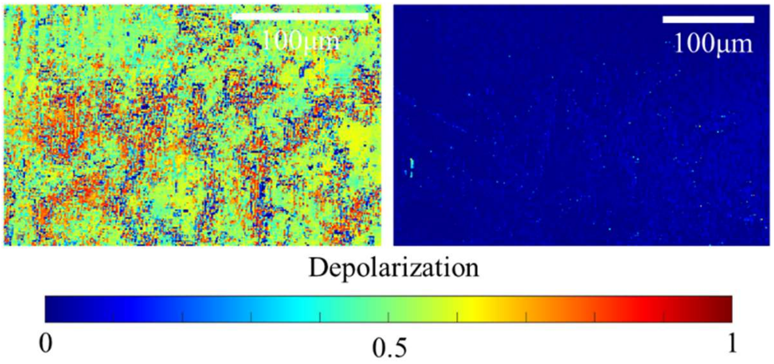

Figure 6.17: Depolarization image of grown and duplicated silver dendrites derived from their Mueller matrix image.

The depolarization image of both the grown and the duplicated sample is shown in Figure 6.17. For grown samples, depolarization values at the dendrite regions range from 0.4~0.9, indicating that the Ag dendrites, as grown, are highly depolarizing. While the duplicated sample has a depolarization value of less than 0.02, indicating rather different material properties due to differences in their porosity and material characteristics.

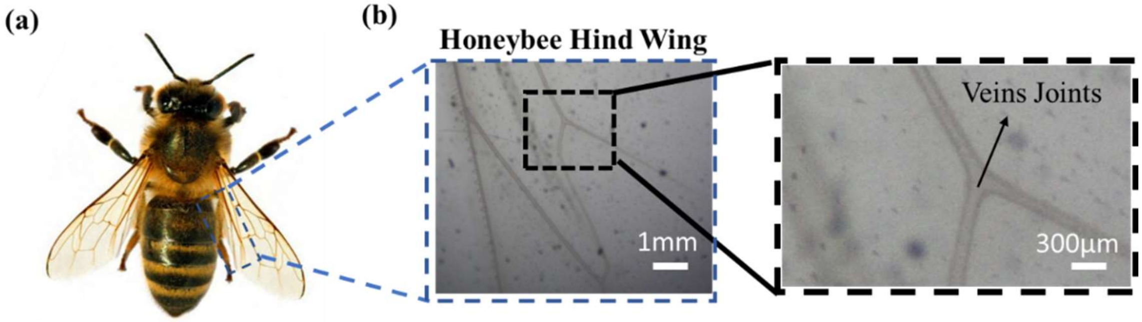

Figure 6.18: Photos and microscopic images of Honeybee wings. (a). Images of Honeybee wings, the location of the hind wing is marked. (b) Microscopic image of honeybee hind wing.

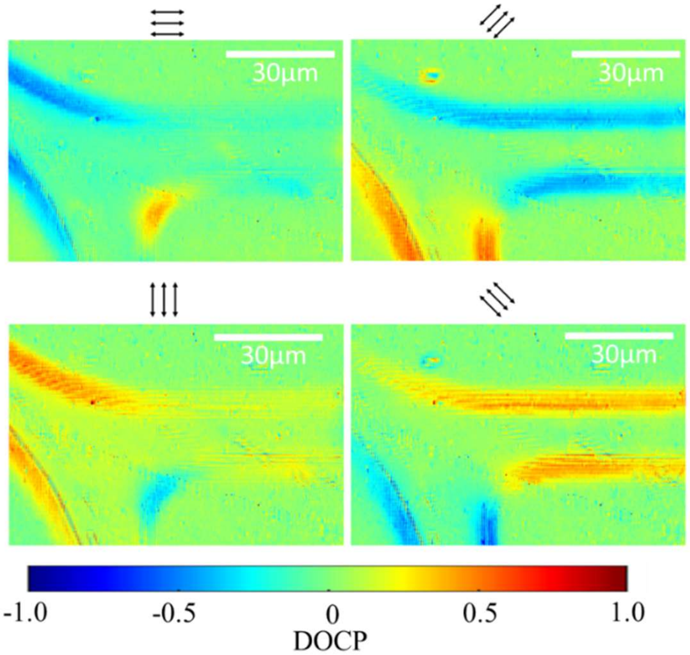

Figure 6.19: Polarization microscopic images of Honeybee wings. (a). Images of Honeybee wings, location of hind wing is marked. (b) Microscopic image of honeybee hind wing.

Next, we demonstrate exemplary applications of our MPIS-MMM in biological research. Figure 6.18 shows the image of the hind wing of a Honeybee, which is composed of wing cells and veins.

Among them, polarization images and MM of one of the vein joints were taken using MPIS-MMM. Figure 6.19 shows the DOCP images of vein joints under LP input with polarization axis along 0°,45°,90°, and 135° respectively. When input light is polarized along or orthogonal to the vein joints, the transmitted light shows a small DOCP. When input light is ~±45° concerning the vein joints, the transmitted light exhibits a positive value of DOCP ~=±0.2. Such DOCP response suggests the tissues connecting bee wing cells and the vein joints have linear birefringence.

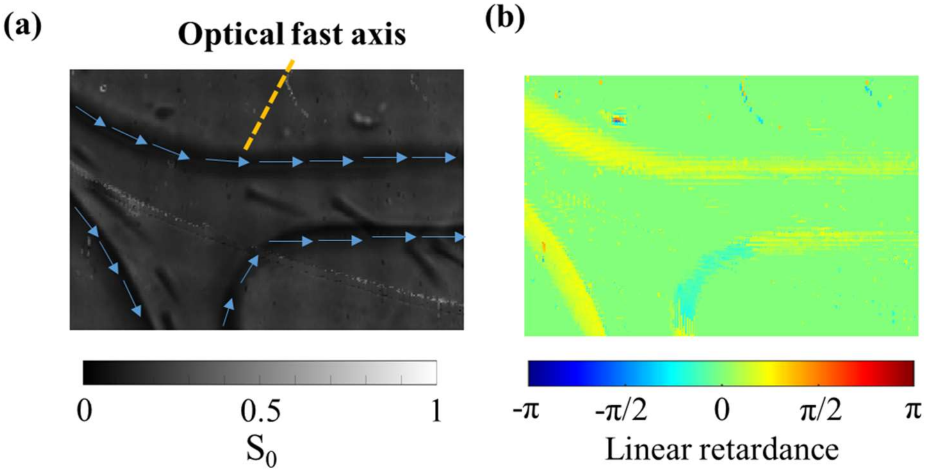

Figure 6.20: Optical fast axis and linear retardance of honeybee wing. (a) Intensity image of vein joints, the optical fast axis of vein joints is marked using blue arrow. (b) Linear retardance image extracted from MM.

The optical fast axis of vein joints is along the joints length direction, as shown by the arrows drawn in Figure 6.20(a). The linear retardance value of the vein joints extracted from the MM is shown in Figure 6.20(b). The opposite signs of linear retardance at the right and bottom branches indicate the flipping of the optical fast axis with the optical slow axis.

6.8. Polarization and Mueller Matrix Imaging Analysis of Human Lung Tissues

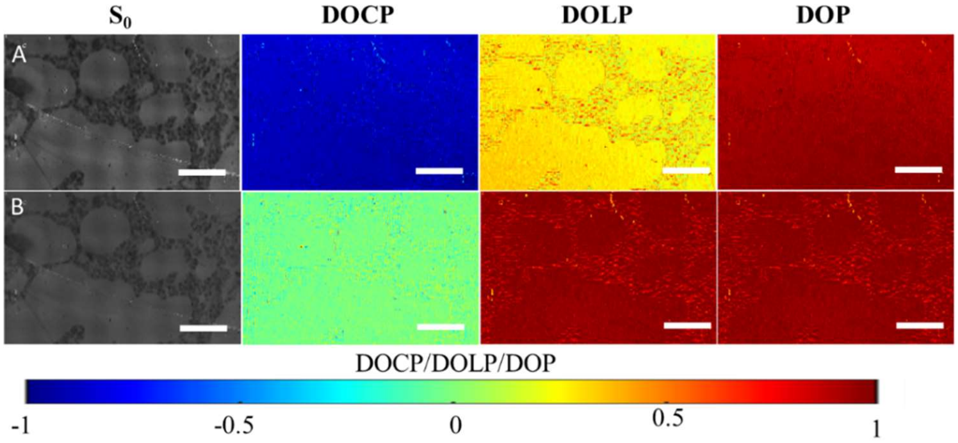

Figure 6.21: Full Stokes polarization image of Human lung tissues. Image Magnification: ×5.

Next, we took polarization images and MM images of healthy human lung tissues using MPIS-MMM. Figure 6.21 shows the polarization images of lung tissues under 90° LP input and LCP input. DOP values of lung tissues are decreased compared to clean substrate regions due to tissue scattering, which depolarizes incoming polarization light upon transmission. An CPL to LPL and COLP to LPL conversion is observed, indicating the lung tissues exhibits optical birefringence effect.

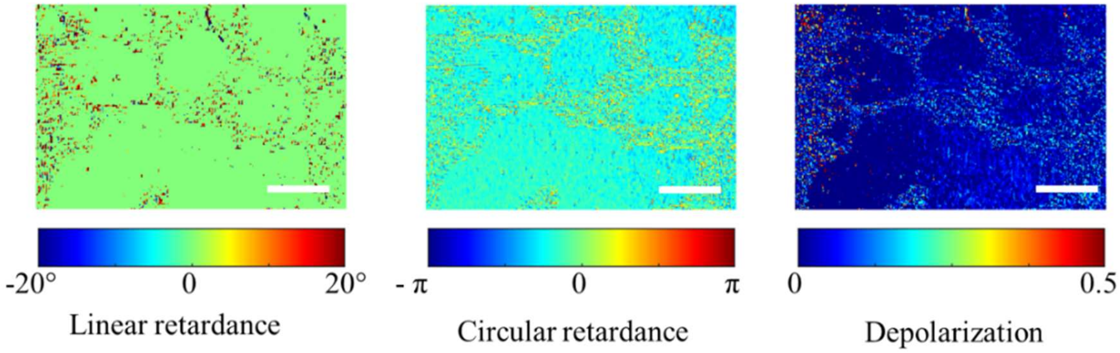

Figure 6.22: Linear, circular retardance and depolarization image extracted from MM of human lung tissue.

Linear, circular retardance, and depolarization images were then extracted from the MM images of the lung tissue, as shown in Figure 6.22. Full MM images are included in Appendix B. Compared to small linear retardance, circular retardance values of lung tissues are much higher. Moreover, depolarization images of lung tissues show depolarization values between 0~0.4, indicating the depolarizing nature of the lung tissues.

6.9. Conclusion and Discussion

In this chapter, we have demonstrated an MPIS-based MMM, the system compactness is improved because of the compactness of MPIS. We performed a systematic calibration process and achieved high accuracy full Stokes polarization detection with average error less than 4% for both transmission and reflection mode. We then applied the calibrated polarization microscope to measure MM of linear polarizer, the measurement result shows MM measurement error is less than 2.1% for both transmission and reflection mode. Then we demonstrated polarization and MM imaging of Si metasurface, silver dendrites, Honeybee hind wings and the human lung tissues. Our MPIS-MMM has advantages in system compactness, dual operation wavelength, high measurement accuracy, and flexible dual mode, promising its applications in industrial inspection, biological and clinical research.

CHAPTER 7

CONCLUSION AND OUTLOOK

My research focuses on solving practical engineering problems during my Ph.D. life. Therefore, it has been changing at different stage of PhD study, from the device fabrication, optical characterization, system development for full Stokes polarization imaging sensor to the firmware development for the underwater polarization mapping system. This chapter gives a summary of my past works in my Ph.D. life and lay out an outlook of future works.

7.1. Conclusion

So far, I have completed three projects related to polarization imaging and their applications. In this dissertation, I firstly demonstrated a pixelated ultra-compact full Stokes polarization imaging sensor through simulation, device fabrication, polarization detection experiment and polarization imaging. The dual working wavelength device demonstrated has the highest compactness among the works demonstrated so far with high polarization detection accuracy under operation angles up to 40°. We then proposed a scalable fabrication process of MPFAs for Chip integrated full Stokes polarization imaging sensor based on NIL. The demonstrated NIL based method successfully lowers the fabrication cost and simplifies the fabrication procedures. Moreover, fabricated chiral metasurface shows optical performance (CPER) being improved up to 10 times using NIL thanks to the planarization process of 2^{nd} layer NIL.

We then applied the full Stokes polarization imaging sensor we developed to built a compact Mueller matrix polarization microscope working in both reflection and transmission mode. Through systematic calibration, the Mueller matrix microscope demonstrated shows high Stokes parameter measurement accuracy with S1,S2,S3 measurement error less than 4% and Mueller matrix measurement error less than 2.1%. We then applied the Mueller matrix microscope to demonstrate applications in imaging optical birefringence of Si metasurface, retardance of biological tissues and depolarization information of silver dendrites.

On the other hand, an underwater polarization mapping system based on compact LP polarization imaging sensors are built for polarization navigation underwater. We performed systematic analysis to explain the advantage of spatial scanning method this system adopted and performed mapping in both clear sky and clean water environments. The mapping results is analyzed qualitatively and require further analysis to demonstrate navigation and geolocation.

7.2. Outlook on Full Stokes Polarization Imaging Sensor

A full Stokes polarization imaging sensor based on metasurface array is demonstrated in the chapter 2. It is shown that the designed chiral metasurface and vertically coupled double layered gratings has serious degradation in optical performance compared to the design in full wave simulation. It is found that surface planarization is a critical step of bi-layer chiral metasurface proposed. Besides, the EBL writing is time consuming and expensive, these issues can be resolved via nanoimprint lithography (NIL), a project which we are working on.

7.3. Outlook on Polarization Imaging Applications

Polarization imaging as a novel method of imaging light, still shows a bright potential in various applications. With the compactness and high measurement accuracy of the full Stokes polarization imaging sensor demonstrated in chapter 2, it is believed that this device can potentially be used for a broad range of applications, such as industrial surveillance of defective samples[5], augmented visions for defense [29], etc.

Using the Mueller matrix microscope discussed in chapter 3, it is possible to extend its applications in biology and clinic applications, such as early cancer diagnosis[101], biology studies of animal bodies[111] and microorganisms [116], it can also be applied to material science studies to evaluate material characteristics[101] , or extracting 3D profiles of objects [117].

Another interesting field is the imaging through water with different water body, especially for turbid water[26] and navigation[77]. It is shown that with the help of polarized light source and polarization imaging, the imaging scene distance of object could be greatly extended and image contrast is greatly improved[118].

REFERENCES

1. Tyo, J., et al., *Target detection in optically scattering media by polarization-difference imaging.* Applied optics, 1996. **35**(11): p. 1855-1870.

2. He, C., et al., *Polarisation optics for biomedical and clinical applications: a review.* 2021. **10**(1): p. 1-20.

3. Li, G. *Recent advances in coherent optical communication*. Advances in optics and photonics, 2009, 1(2), 279-307.

4. Tyo, J.S., et al., *Review of passive imaging polarimetry for remote sensing applications.* Applied optics, 2006. **45**(22): p. 5453-5469.

5. Meriaudeau, F., et al. *Polarization imaging for industrial inspection*. in *Image Processing: Machine Vision Applications*. (Vol. 6813, pp. 72-81). SPIE.2008

6. Kim, N., et al., *3D display technology.* 2014. **1**(1): p. 73-95.

7. Shipman, J.D., et al. *An introduction to physical science*. 2012: Cengage Learning.

8. Balanis, C.A. *Antenna theory: analysis and design*. 2015: John wiley & sons.

9. Stokes, G.G. *On the composition and resolution of streams of polarized light from different sources.* 1851. **9**: p. 399.

10. Collett, E. *Field guide to polarization*. 2005. Spie Bellingham, WA.

11. Jones, R.C, et al. *A new calculus for the treatment of optical systemsiii. the sohncke theory of optical activity.* 1941. **31**(7): p. 500-503.

12. Savenkov, S.N., *Jones and Mueller matrices: structure, symmetry relations and information content*, in *Light Scattering Reviews 4*. 2009, Springer. p. 71-119.

13. Bass, M., *Handbook of optics: volume I-geometrical and physical optics, polarized light, components and instruments*. 2010: McGraw-Hill Education.

14. Fujiwara, H., *Spectroscopic ellipsometry: principles and applications*. 2007: John Wiley & Sons.

15. Schaefer, B., et al., *Measuring the Stokes polarization parameters.* 2007. **75**(2): p. 163-168.

16. Vedel, M., et al. *Full Stokes polarization imaging camera*. in *Polarization Science and Remote Sensing V*. 2011. International Society for Optics and Photonics.

17. Tu, X., et al., *Division of amplitude RGB full-Stokes camera using micro-polarizer arrays.* 2017. **25**(26): p. 33160-33175.

18. Tu, X., et al., *Division of focal plane red–green–blue full-Stokes imaging polarimeter.* Applied optics, 2020. **59**(22): p. G33-G40.

19. Sony. *Sony Polarsens* 2022; Available from: https://www.sony-semicon.com/en/technology/industry/polarsens.html.

20. Myhre, G., et al., *Liquid crystal polymer full-stokes division of focal plane polarimeter.* Optics express, 2012. **20**(25): p. 27393-27409.

21. Gruev, V., et al. *CCD polarization imaging sensor with aluminum nanowire optical filters.* Optics express, 2010. **18**(18): p. 19087-19094.

22. Shabat, G., et al., *Randomized LU decomposition.* 2018. **44**(2): p. 246-272.

23. Betzler, K.J.F.P.U.O., *Fitting in Matlab.* 2003.

24. Lu, S.-Y. , R.A. Chipman, *Interpretation of Mueller matrices based on polar decomposition.* 1996. **13**(5): p. 1106-1113.

25. Garren, D.A., et al., *Full-polarization matched-illumination for target detection and identification.* IEEE Transactions on Aerospace and Electronic Systems, 2002. **38**(3): p. 824-837.

26. Lu, H., et al., *Underwater optical image processing: a comprehensive review.* 2017. **22**(6): p. 1204-1211.

27. Demos, S.G., et al, *Deep subsurface imaging in tissues using spectral and polarization filtering.* Optics Express, 2000. **7**(1): p. 23-28.

28. Jacques, S.L., J.R. Roman, and K. Lee, *Imaging superficial tissues with polarized light.* Lasers in surgery and medicine, 2000. **26**(2): p. 119-129.

29. Duan, J., et al. *Review of polarization imaging for international military application*. in *International Symposium on Photoelectronic Detection and Imaging 2013: Imaging Sensors and Applications*. 2013. International Society for Optics and Photonics.

30. Kuhn, J.R., D. Potter, et al. *Imaging polarimetric observations of a new circumstellar disk system.* The Astrophysical Journal Letters, 2001. **553**(2): p. L189.

31. Papakostas, A., et al., *Optical manifestations of planar chirality.* 2003. **90**(10): p. 107404.

32. Krasavin, A., et al., *Polarization conversion and "focusing" of light propagating through a small chiral hole in a metallic screen.* 2005. **86**(20): p. 201105.

33. Wu, C., et al., *Spectrally selective chiral silicon metasurfaces based on infrared Fano resonances.* 2014. **5**(1): p. 1-9.

34. Hsu, W.-L., et al., *Polarization microscope using a near infrared full-Stokes imaging polarimeter.* 2015. **23**(4): p. 4357-4368.

35. Khorasaninejad, M., et al., *Multispectral chiral imaging with a metalens.* 2016. **16**(7): p. 4595-4600.

36. Rubin, N.A., et al., *Polarization state generation and measurement with a single metasurface.* Optics express, 2018. **26**(17): p. 21455-21478.

37. Arbabi, E., et al., *Full-Stokes imaging polarimetry using dielectric metasurfaces.* Acs Photonics, 2018. **5**(8): p. 3132-3140.

38. Rubin, N.A., et al., *Matrix Fourier optics enables a compact full-Stokes polarization camera.* Science, 2019. **365**(6448).

39. Yang, Z., et al., *Generalized Hartmann-Shack array of dielectric metalens sub-arrays for polarimetric beam profiling.* Nature communications, 2018. **9**(1): p. 1-7.

40. Zhang, C., et al., *High efficiency all-dielectric pixelated metasurface for near-infrared full-Stokes polarization detection.* Photonics Research, 2021. **9**(4): p. 583-589.

41. Bai, J. , Y. Yao. *Highly efficient anisotropic chiral plasmonic metamaterials for polarization conversion and detection.* ACS nano, 2021. **15**(9): p. 14263-14274.

42. Wu, P.C., et al., *Visible metasurfaces for on-chip polarimetry.* Acs Photonics, 2017. **5**(7): p. 2568-2573.

43. Mueller, J.B., K. Leosson, et al. *Ultracompact metasurface in-line polarimeter.* Optica, 2016. **3**(1): p. 42-47.

44. Jung, M., et al., *Polarimetry using graphene-integrated anisotropic metasurfaces.* ACS Photonics, 2018. **5**(11): p. 4283-4288.

45. Basiri, A., et al., *Nature-inspired chiral metasurfaces for circular polarization detection and full-Stokes polarimetric measurements.* Light: Science & Applications, 2019. **8**(1): p. 1-11.

46. Afshinmanesh, F., et al., *Measurement of the polarization state of light using an integrated plasmonic polarimeter.* Nanophotonics, 2012. **1**(2): p. 125-129.

47. Lee, K., et al., *Ultracompact broadband plasmonic polarimeter.* Laser & Photonics Reviews, 2018. **12**(3): p. 1700297.

48. Li, L., et al., *Monolithic Full-Stokes Near-Infrared Polarimetry with Chiral Plasmonic Metasurface Integrated Graphene–Silicon Photodetector.* ACS nano, 2020. **14**(12): p. 16634-16642.

49. Rubin, N.A., et al., *Polarization state generation and measurement with a single metasurface.* Optics express, 2018. **26**(17): p. 21455-21478.

50. Chen, X., et al., *Plasmonic vertically coupled complementary antennas for dual-mode infrared molecule sensing.* ACS nano, 2017. **11**(8): p. 8034-8046.

51. Wang, C., et al., *Plasmonic bar-coupled dots-on-pillar cavity antenna with dual resonances for infrared absorption and sensing: Performance and nanoimprint fabrication.* Acs Nano, 2014. **8**(3): p. 2618-2624.

52. Fan, S. , J.D. Joannopoulos, *Analysis of guided resonances in photonic crystal slabs.* Physical Review B, 2002. **65**(23): p. 235112.

53. Wang, S., et al., *Guided-mode resonances in planar dielectric-layer diffraction gratings.* JOSA A, 1990. **7**(8): p. 1470-1474.

54. Wang, S. and R. Magnusson, *Theory and applications of guided-mode resonance filters.* Applied optics, 1993. **32**(14): p. 2606-2613.

55. Pezzaniti, J.L. and D.B. Chenault. *A division of aperture MWIR imaging polarimeter*. in *Polarization Science and Remote Sensing II*. 2005. International Society for Optics and Photonics.

56. Andreou, A.G. and Z.K. Kalayjian, *Polarization imaging: principles and integrated polarimeters.* IEEE Sensors journal, 2002. **2**(6): p. 566-576.

57. Tokuda, T., et al., *Polarisation-analysing CMOS photosensor with monolithically embedded wire grid polariser.* Electronics letters, 2009. **45**(4): p. 228-230.

58. Zhao, X., et al., *Thin photo-patterned micropolarizer array for CMOS image sensors.* IEEE Photonics Technology Letters, 2009. **21**(12): p. 805-807.

59. Gruev, V., et al., *Fabrication of a dual-tier thin film micropolarization array.* Optics express, 2007. **15**(8): p. 4994-5007.

60. Gruev, V., J. Van der Spiegel, and N.J.O.e. Engheta, *Dual-tier thin film polymer polarization imaging sensor.* 2010. **18**(18): p. 19292-19303.

61. Altaqui, A., et al., *Mantis shrimp–inspired organic photodetector for simultaneous hyperspectral and polarimetric imaging.* Science Advances, 2021. **7**(10): p. eabe3196.

62. Nordin, G.P., et al., *Micropolarizer array for infrared imaging polarimetry.* 1999. **16**(5): p. 1168-1174.

63. Coleman, D., et al., *Polarization-modulated smectic liquid crystal phases.* Science, 2003. **301**(5637): p. 1204-1211.

64. Shopsowitz, K.E., et al., *Free-standing mesoporous silica films with tunable chiral nematic structures.* Nature, 2010. **468**(7322): p. 422-425.

65. Sánchez-Carnerero, E.M., et al., *Circularly polarized luminescence by visible-light absorption in a chiral O-BODIPY dye: unprecedented design of CPL organic molecules from achiral chromophores.* Journal of the American Chemical Society, 2014. **136**(9): p. 3346-3349.

66. Wang, J.J., et al., *30-nm-wide aluminum nanowire grid for ultrahigh contrast and transmittance polarizers made by UV-nanoimprint lithography.* Applied physics letters, 2006. **89**(14): p. 141105.

67. Wang, J.J., et al., *High-performance, large area, deep ultraviolet to infrared polarizers based on 40 nm line/78 nm space nanowire grids.* Applied physics letters, 2007. **90**(6): p. 061104.

68. Azzam, R., *Instrument matrix of the four-detector photopolarimeter: physical meaning of its rows and columns and constraints on its elements.* JOSA A, 1990. **7**(1): p. 87-91.

69. Berry, H.G., G. Gabrielse, and A. Livingston, *Measurement of the Stokes parameters of light.* Applied optics, 1977. **16**(12): p. 3200-3205.

70. Ren, H., et al., *Sensor Modeling and Calibration Method Based on Extinction Ratio Error for Camera-Based Polarization Navigation Sensor.* 2020. **20**(13): p. 3779.

71. Mysak, L.A. and K. Hamilton, *ATMOSPHERIC AND OCEANOGRAPHIC SCIENCES LIBRARY.*

72. Singh, S., et al. *Underwater acoustic navigation with the WHOI micro-modem*. in *OCEANS 2006*. 2006. IEEE.

73. Webster, S.E., et al., *Advances in single-beacon one-way-travel-time acoustic navigation for underwater vehicles.* 2012. **31**(8): p. 935-950.

74. Kinsey, J.C., R.M. Eustice, and L.L. Whitcomb. *A survey of underwater vehicle navigation: Recent advances and new challenges*. in *IFAC conference of manoeuvering and control of marine craft*. 2006. Lisbon.

75. Stutters, L., et al., *Navigation technologies for autonomous underwater vehicles.* 2008. **38**(4): p. 581-589.

76. Powell, S.B., et al., *Bioinspired polarization vision enables underwater geolocalization.* 2018. **4**(4): p. eaao6841.

77. Pengwei, H., et al., *Solar-tracking methodology based on refraction-polarization in Snell's window for underwater navigation.* 2022. **35**(3): p. 380-389.

78. Labhart, T., E.P.J.M.r. Meyer, and technique, *Detectors for polarized skylight in insects: a survey of ommatidial specializations in the dorsal rim area of the compound eye.* 1999. **47**(6): p. 368-379.

79. el Jundi, B., et al., *Diurnal dung beetles use the intensity gradient and the polarization pattern of the sky for orientation.* 2014. **217**(13): p. 2422-2429.

80. Sun, S., et al., *Improved models of imaging of skylight polarization through a fisheye lens.* 2019. **19**(22): p. 4844.

81. Zhao, H., et al., *Polarization patterns under different sky conditions and a navigation method based on the symmetry of the AOP map of skylight.* 2018. **26**(22): p. 28589-28603.

82. Wang, X., J. Gao, and N.W.J.O.E. Roberts, *Bio-inspired orientation using the polarization pattern in the sky based on artificial neural networks.* 2019. **27**(10): p. 13681-13693.

83. Tang, J., et al., *Novel robust skylight compass method based on full-sky polarization imaging under harsh conditions.* 2016. **24**(14): p. 15834-15844.

84. Fan, C., et al., *Multicamera polarized vision for the orientation with the skylight polarization patterns.* 2018. **57**(4): p. 043101.

85. Ma, T., et al., *An evaluation of skylight polarization patterns for navigation.* 2015. **15**(3): p. 5895-5913.

86. Sparks, W.B., et al., *Detection of circular polarization in light scattered from photosynthetic microbes.* 2009. **106**(19): p. 7816-7821.

87. *Lens designs*. Available from: https://sites.google.com/site/danreiley/PhotoPrime.

88. Schechner, Y.Y. and N.J.I.J.o.o.e. Karpel, *Recovery of underwater visibility and structure by polarization analysis.* 2005. **30**(3): p. 570-587.

89. Socol, Y., et al., *Suspensive electrode formation in pulsed sonoelectrochemical synthesis of silver nanoparticles.* 2002. **18**(12): p. 4736-4740.

90. Zhao, Z., et al., *Photochemical synthesis of dendritic silver nano-particles for anti-counterfeiting.* 2019. **7**(20): p. 6099-6104.

91. Wang, X., et al., *Synthesis of silver dendritic nanostructures protected by tetrathiafulvalene.* 2002(12): p. 1300-1301.

92. Imai, H., et al., *Anisotropic growth of silver crystals with ethylenediamine tetraacetate and formation of planar and stacked wires.* 2005. **5**(3): p. 1073-1077.

93. Majidi, M.R., et al., *Synthesis of dendritic silver nanostructures supported by graphene nanosheets and its application for highly sensitive detection of diazepam.* 2015. **57**: p. 257-264.

94. Cheng, Z.-Q., et al., *Morphology-controlled fabrication of large-scale dendritic silver nanostructures for catalysis and SERS applications.* 2019. **14**(1): p. 1-7.

95. Zhou, Y., et al., *Multiplexed SERS barcodes for anti-counterfeiting.* 2020. **12**(25): p. 28532-28538.

96. Kim, J.H., et al., *Polarized light scattering by dielectric and metallic spheres on silicon wafers.* 2002. **41**(25): p. 5405-5412.

97. Sheppard, C.J., et al. *Characterization of the Mueller Matrix: Purity Space and Reflectance Imaging*. in *Photonics*. 2022. MDPI.

98. He, H., et al., *Mueller matrix polarimetry—an emerging new tool for characterizing the microstructural feature of complex biological specimen.* 2019. **37**(11): p. 2534-2548.

99. Stutz, Aaron Jonas. *Polarizing microscopy identification of chemical diagenesis in archaeological cementum.* Journal of Archaeological Science. 2002. **29**(11): p. 1327-1347.

100. Jiao, S., G. Yao et al, *Depth-resolved two-dimensional Stokes vectors of backscattered light and Mueller matrices of biological tissue measured with optical coherence tomography.* Applied Optics. 2000. **39**(34): p. 6318-6324.

101. Wang, Y., et al., *Mueller matrix microscope: a quantitative tool to facilitate detections and fibrosis scorings of liver cirrhosis and cancer tissues.* Journal of biomedical optics. 2016. **21**(7): p. 071112.

102. Liu, T., et al., *Comparative study of the imaging contrasts of Mueller matrix derived parameters between transmission and backscattering polarimetry.* Biomedical Optics Express. 2018. **9**(9): p. 4413-4428.

103. Zhou, J., et al., *Modulus design multiwavelength polarization microscope for transmission Mueller matrix imaging.* Journal of Biomedical Optics. 2018. **23**(1): p. 016007.

104. Arteaga, O., et al., *Mueller matrix microscope with a dual continuous rotating compensator setup and digital demodulation.* Applied Optics 2014. **53**(10): p. 2236-2245.

105. Dong, Y., et al., *Deriving polarimetry feature parameters to characterize microstructural features in histological sections of breast tissues.* 2020. **68**(3): p. 881-892.

106. Arteaga, O., et al., *Mueller matrix polarimetry with four photoelastic modulators: theory and calibration.* 2012. **51**(28): p. 6805-6817.

107. Alali, S. and I. A. Vitkin, *Optimization of rapid Mueller matrix imaging of turbid media using four photoelastic modulators without mechanically moving parts.* Optical Engineering 2013. **52**(10): p. 103114.

108. De Martino, A., et al., *Optimized Mueller polarimeter with liquid crystals.* Optics letters. 2003. **28**(8): p. 616-618.

109. Laude-Boulesteix, B., et al., *Mueller polarimetric imaging system with liquid crystals.* Applied optics 2004. **43**(14): p. 2824-2832.

110. Huang, T., et al., *Dual division of focal plane polarimeters-based collinear reflection Mueller matrix fast imaging microscope.* Journal of Biomedical Optics 2022. **27**(8): p. 086501.

111. Gottlieb, Dale, and Oriol Arteaga. *Mueller matrix imaging with a polarization camera: Application to microscopy.* Optics Express 2021. **29**(21): p. 34723-34734.

112. Su, V.-C., et al., *Advances in optical metasurfaces: fabrication and applications.* Optics express 2018. **26**(10): p. 13148-13182.

113. Lin, S., Y. Chen, and Z.J.J.N. Wong, *High-performance optical beam steering with nanophotonics.* Nanophotonics 2022. **11**(11): p. 2617-2638.

114. Khorasaninejad, M. and F.J.S. Capasso, *Metalenses: Versatile multifunctional photonic components.* Science 2017. **358**(6367): p. eaam8100.

115. Dharmavarapu, R., S. Bhattacharya, and S.J.S. Juodkazis, *GDOESII: software for design of diffractive optical elements and phase mask conversion to GDSII lithography files.* SoftwareX 2019. **9**: p. 126-131.

116. Mazumder, N., et al., *Mueller matrix signature in advanced fluorescence microscopy imaging.* Journal of Optics 2017. **19**(2): p. 025301.

117. Garcia-Caurel, E., et al., *Advanced Mueller ellipsometry instrumentation and data analysis*, in *Ellipsometry at the Nanoscale*. 2013, Springer. p. 31-143.

118. Cronin, T.W. and Justin Marshall, *Patterns and properties of polarized light in air and water.* Philosophical Transactions of the Royal Society B: Biological Sciences . 2011. **366**(1565): p. 619-626.

APPENDIX A

SIMULATION, FABRICATION AND CHARACTERIZATION DETIALS OF CHIP-INTEGRATED FULL-STOKES POLARIMETRIC CMOS IMAGIN SENSOR

Simulations

FDTD simulations from Lumerical Inc. FDTD solver were applied to calculate the transmission efficiency, CPER of the chiral metasurface, and LPER of double-layer gratings. The real optical material refractive index of Si and Aluminum measured by UV-NIR spectroscopic ellipsometry (J.A. Woollam, M-2000) was applied to FDTD material explorer to calculate the device performance precisely. Specifically, for the simulation of double-layer gratings, the plane wave along the grating width and grating length direction was applied to calculate the LPER and efficiency of double-layer gratings. For the chiral metasurface, a tilt angle of 6° of the Si grating obtained from SEM images was considered in the simulations. Two orthogonally linearly polarized plane waves with a phase difference of $\pm\pi / 2$ were superpositioned to represent LCP/RCP light input, respectively. In all FDTD simulations, we simulate one unit cell and apply periodic boundary conditions along the in-plane direction. The simulation convergence auto shut-off level was set to 10^{-5}. The mesh size was set to 2nm for higher simulation accuracy. For oblique incidence, we use the BFAST plane wave type to maintain the oblique incidence angle the same for all wavelengths.

Fabrication

1) Si nanograting: Fused silica wafer was cleaned by RCA-1 cleaning, then amorphous silicon (α-Si) of 130 nm was deposited by plasma-enhanced chemical vapor deposition (PECVD) (Oxford Plasmalab 100, 350 °C/ 15W) on fused silica wafer, followed by deposition of 60 nm SiO_x (350°C/ 20W) without breaking vacuum as a hard mask layer. 10 nm Cr layer was then deposited by thermally evaporating (Denton benchtop turbo) as the discharge layer during 1st EBL exposure. Double-layer polymethyl

methacrylate (PMMA) resists (70 nm 2.5% 495k followed with 50 nm 2% 950k) were coated, followed by 2-minute post-baking at 180℃. A pattern composed of 96 by 64 meta-pixels array was written with a JEOL JBX-6000FS EBL machine working at 50keV with a current of 500pA. After exposure, the sample was developed for 2 minutes. The developer is a mixture of methyl isobutyl ketone (MIBK) and isopropanol (IPA) with a mixing ratio of 1:3. Next, the sample is cleaned with 30 seconds of Oxygen plasma (PIE Scientific Plasma cleaner, immersion mode O_2 10sccm /20W) to remove PMMA residue on the exposure region. Next, 3nm Cr adhesive layer and 12nm SiO_x were deposited by electron beam evaporating (lesker #3). Cr and SiO_x were lifted off by soaking in warm acetone (60℃) for more than 12 hours, followed by acetone gun cleaning. After the lift-off process, a SiO_x nanostructures array was formed, which masked Cr discharge layer etching by Reactive Ion Etching (RIE) (OXFORD PLASMALAB 80PLUS, Cl2/O2: 9/3 sccm, 10mTorr, D.C. bias/power 18V/70W). An isolated Cr/SiO_x layered nanostructure mask were thus formed, which then masked anisotropic etching of 60nm SiO_x hard mask by RIE (Plasmatherm RIE 790, CHF_3/ O_2 40/3 sccm, 40 mTorr, 250 W). The dry etching of SiO_x stopped at the α-Si layer; during the dry etching procedure, 12nm SiO_x on SiO_x/Cr layered structure was consumed. Then the Cr was removed by CR-4s (Cyantek) etchant, and the α-Si layer was etched by ICP-RIE (ICP/bias power of 250/140 W, 10 mTorr, Cl_2:Ar=100/5 sccm) using the SiOx mask to complete Si nanograting fabrication.

2) Spacer deposition: The samples were brought into the sputtering chamber (Lesker PVD 75) and covered with a 520 nm SiO_x spacer layer (250W) at a rate of 0.6 Å/s.

3) Vertically coupled aluminum (Al) gratings: After spacer layer deposition, double-layer PMMA (70 nm 2.5% 495k followed with 50 nm 2% 950k) were coated again, post-

baked, and exposed by EBL aligned to the first layer. Then the sample was cleaned with Oxygen plasma to remove residual PMMA on the exposed region. Next, 3nm Cr and 12nm SiO_x were deposited and lifted off, as mentioned above, to form a SiO_x mask for Cr discharge layer etching. Next, Cr discharging layer is etched by RIE to form Cr/SiO_x layered nanostructures, which masked 80nm SiO_x RIE etching to form SiO_x nano-gratings. Then 2nm Cr and 60nm Aluminum is deposited by E-beam evaporation, forming vertically coupled Aluminum (Al) gratings.

4) U.V. bonding: After sample fabrication is completed and essential device characterization, the sample was then cutted into 3mm*4mm by a dicing saw. A CMOS sensor IMX477 was customized to remove the cover glass, micro lens, and Bayer pattern. Then it was spin-coated with 90% UV at a spin speed of 3000rpm/S; the sample was then visually aligned by a homemade transfer setup detailed schematic illustrated in supplementary figure S9. and bonded onto the CMOS sensor. Afterward, U.V. resists cured by a 365nm U.V. lamp(100W) for 20 minutes of illumination.

Measurement

Device Transmission and Extinction Ratio Characterization. For the chiral metasurface, the unpolarized laser was first polarized by linear polarizer (WP25M-UB by Thorlabs, Inc.) and super achromatic QWP (SAQWP05M-700 by Thorlabs, Inc.) to generate LCP, RCP input, respectively. The CP light is then focused onto the sample with a focal spot size of 15um in diameter. The transmission efficiency was then measured using Olympus BX53 fluorescent microscope and Horiba iHR320 visible spectrometer. The CPER of LCP chiral metasurface was calculated using the formula:$E = T_{LCP}/T_{RCP}$, where T_{LCP} ,T_{RCP} denotes the transmission efficiency of LCP and RCP input, respectively. As for double-layer gratings, the transmission efficiency of s-polarized and p-polarized input was measured respectively to calculate LPER.

Instrument matrix calibration for polarization Imager. Eight polarization states were induced with a broadband linear polarizer (WP25M-UB by Thorlabs, Inc.) and super achromatic QWP (SAQWP05M-700 by Thorlabs, Inc.). The induced polarization states are then normally incident onto the polarization imager. Images were taken with sufficient exposure time to ensure a high enough signal-to-noise ratio (SNR). The instrument matrix of each super-pixel was then calculated in Matlab according to the transmitted intensities of each metasurface filter.

Full Stokes polarization detection measurement. Light coming from a High-Intensity Fiber coupled Halogen lamp light source (Thorlabs OSL2) is firstly collimated using a parabolic mirror (Thorlabs MPD129-P01), and the iris is applied to control the beam divergence angle. The bandpass filter (red: FBH650-40 cyan: FBH500-40) is applied for wavelength selection. Lens with F=30(AC254-030-AB) and F=100(AC254-100-AB) are applied for beam expansion. The final beam divergence is controlled to be 0.5 degrees with a spot size of 9mm in diameter. Arbitrary polarization states were generated using a broadband linear polarizer (WP25M-UB by Thorlabs, Inc.) and super achromatic QWP (SAQWP05M-700 by Thorlabs, Inc.) A list of Stokes parameters was first designed, then each polarization state was normally incident onto the polarization imager. These polarization states were firstly measured by the rotation of a linear analyzer (LPIREA100-C); the transmitted intensity was then fitted to obtain the polarization states. Afterward, the polarization states were captured by the polarization imager at a normal incidence angle.

The images were then transferred onto a computer to calculate polarization states according to the transmitted intensities and the calibrated instrument matrix of each metasurface filter. The code for extracting polarization states for all super-pixels as well as Stokes parameter measurement, is performed in a Matlab environment.

Full Stokes polarization imaging. A camera zoom lens is applied for imaging purposes. A color filter is attached in front of the lens. The field of view of the camera lens applied is ~ ±20 degrees for imaging demonstration.

Instrument matrix calibration process. The transmitted intensity of a linear grating which transmits LP light oriented in a horizontal direction, can be described by the input polarization state $\vec{s}$ And the first row of its Mueller matrix:

$$s_0^{HG\_out} = [m_{11}^{HG} \quad m_{12}^{HG} \quad m_{13}^{HG} \quad m_{14}^{HG}] \times \begin{bmatrix} s_0^{in} \\ s_1^{in} \\ s_2^{in} \\ s_3^{in} \end{bmatrix} \tag{A.1}$$

Likewise, the output intensity of linear gratings responsible for detection of 90°, 45°, 135° LP light, and chrial metasurface responsible for detection of LCP and RCP light can also be described by the input polarization state and their first row of mueller matrix:

$$I = \begin{bmatrix} s_0^{0G\_out} \\ s_0^{90G\_out} \\ s_0^{135G\_out} \\ s_0^{45G\_out} \\ s_0^{LCPG\_out} \\ s_0^{RCPG\_out} \end{bmatrix} = \begin{bmatrix} m_{11}^{0G} & m_{12}^{0G} & m_{13}^{0G} & m_{14}^{0G} \\ m_{11}^{90G} & m_{12}^{90G} & m_{13}^{90G} & m_{14}^{90G} \\ m_{11}^{135G} & m_{12}^{135G} & m_{13}^{135} & m_{14}^{135G} \\ m_{11}^{45} & m_{12}^{45G} & m_{13}^{45G} & m_{14}^{45} \\ m_{11}^{LCPG} & m_{12}^{LCPG} & m_{13}^{LCPG} & m_{14}^{LCPG} \\ m_{11}^{RCPG} & m_{12}^{RCPG} & m_{13}^{RCPG} & m_{14}^{RCPG} \end{bmatrix} \times \begin{bmatrix} s_0^{in} \\ s_1^{in} \\ s_2^{in} \\ s_3^{in} \end{bmatrix} = A \times S \tag{A.2}$$

The matrix A here is denoted as the instrument matrix of the metasurface filter array. For any unknown polarization state $\vec{s}'$, it can be inversely calculated via the transmission intensity and the instrument matrix:

$$\vec{s}' = A^{-1} \times I \tag{A.3}$$

The measurement of the instrument matrix A can be done by inputting more than four pre-known polarization states measured by traditional angle-resolved measurements:

$$A = \begin{bmatrix} S_0^{0G\_1} & S_0^{0G\_2} & S_0^{0G\_3} & S_0^{0G\_4} \\ S_0^{90G\_1} & S_0^{90G\_2} & S_0^{90G\_3} & S_0^{90G\_4} \\ S_0^{135G\_1} & S_0^{135G\_2} & S_0^{135G\_3} & S_0^{135\ \ \_4} \\ S_0^{45G\_1} & S_0^{45G\_2} & S_0^{45G\_3} & S_0^{45G\_4} \\ S_0^{LCPG\_1} & S_0^{LCPG\_2} & S_0^{LCPG\_3} & S_0^{LCPG\_4} \\ S_0^{RCPG\_1} & S_0^{RCPG\_2} & S_0^{RCPG\_3} & S_0^{RCPG\_4} \end{bmatrix} \times \begin{bmatrix} S_0^1 S_0^2 S_0^3 S_0^4 \\ S_1^1 S_1^2 S_1^3 S_1^4 \\ S_2^1 S_2^2 S_2^3 S_2^4 \\ S_3^1 S_3^2 S_3^3 S_3^4 \end{bmatrix}^{-1} = I \times S^{-1} \tag{A.4}$$

To guarantee a more stable calculation of the instrument matrix, eight polarization states are used for real measurements.

APPENDIX B

ERROR DISTRIBUTION FOR FULL STOKES POLARIZATION DETECTION

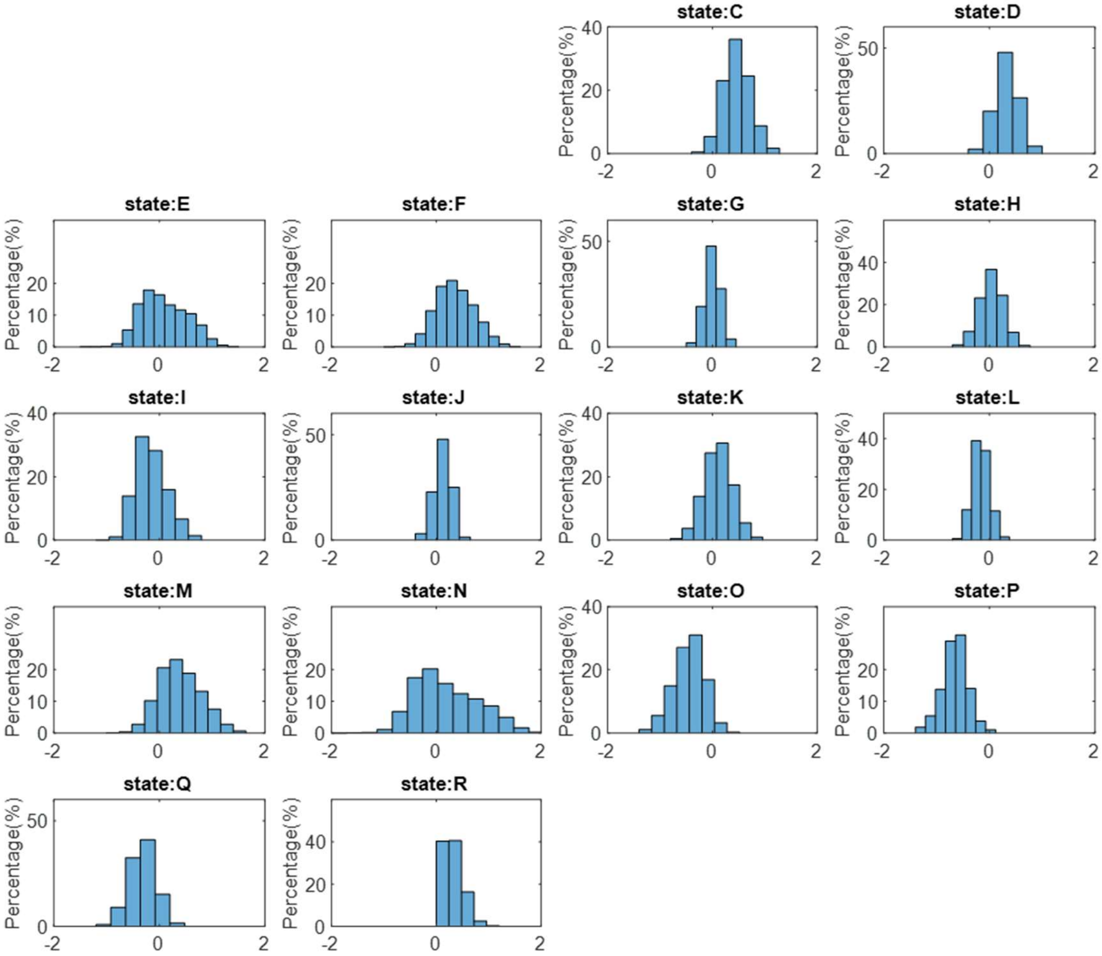

Figure B. 1: AOP measurement error distribution of MPFA under red color input, $\varphi = 0°$.

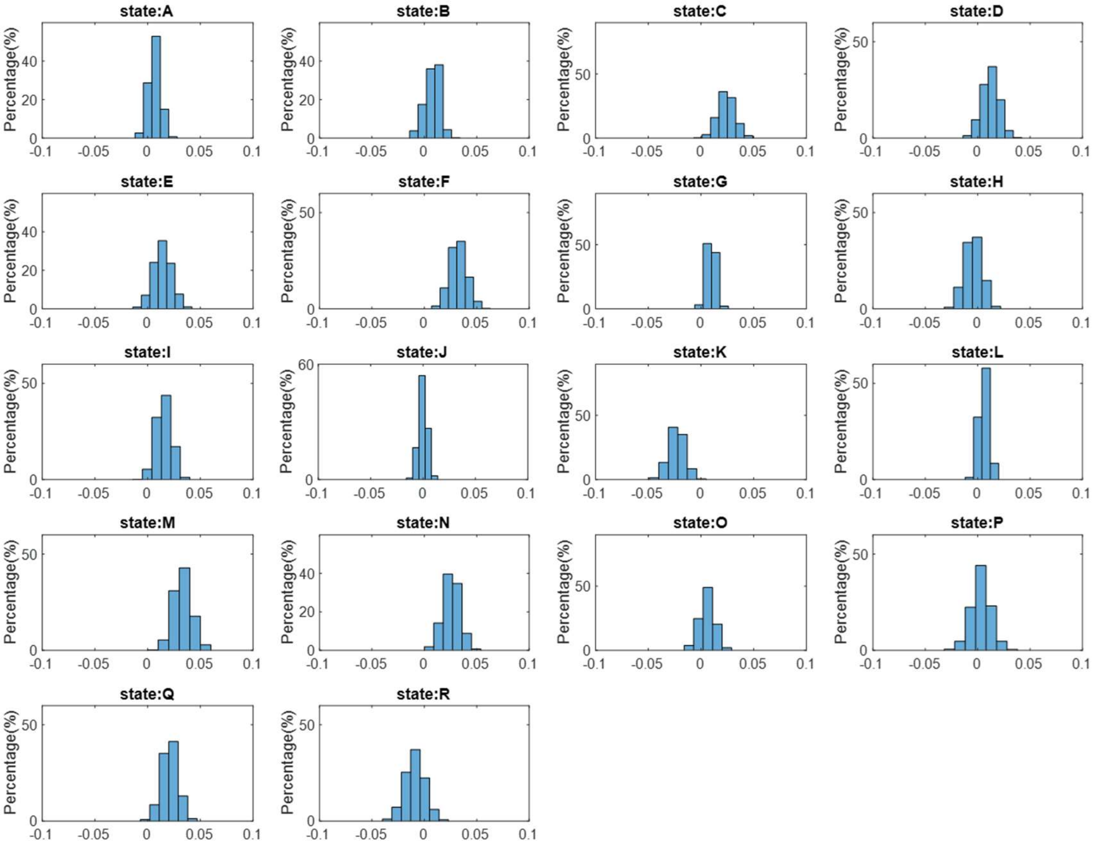

Figure B. 2: DOLP measurement error distribution of MPFA under red color input, $\varphi = 0°$.

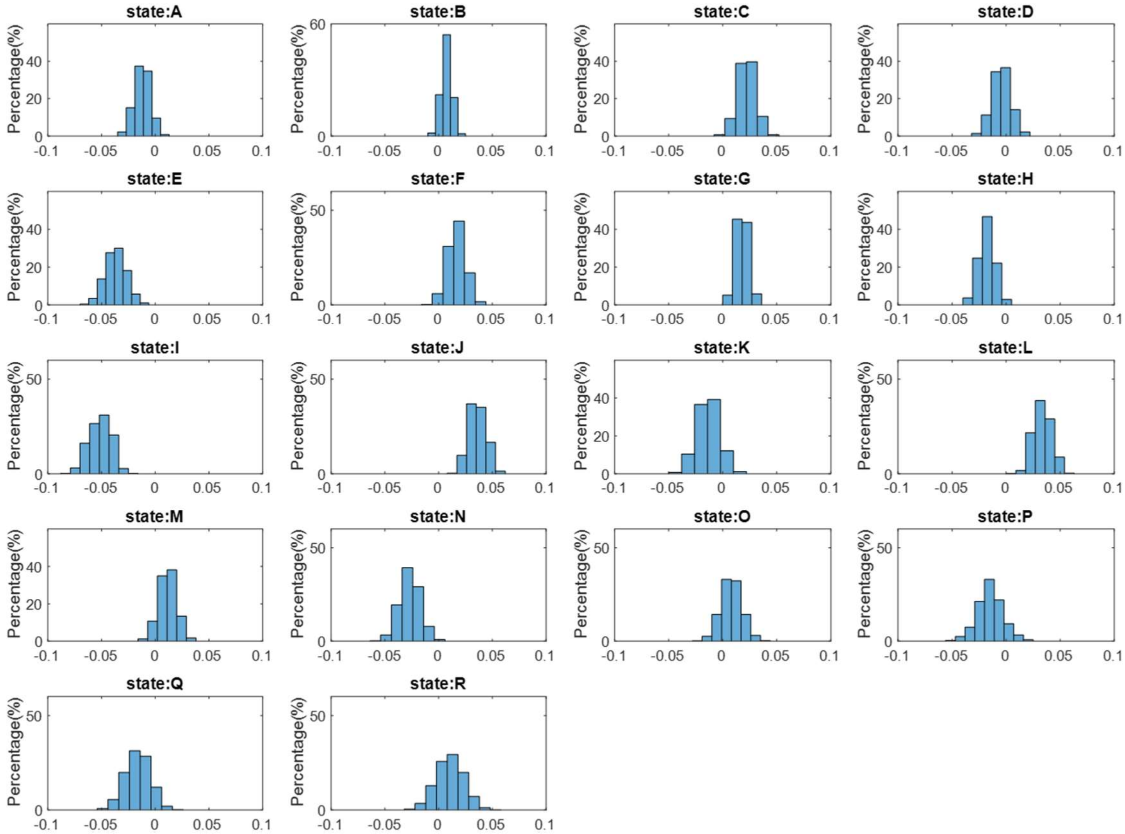

Figure B. 3: DOCP measurement error distribution of MPFA under red color input, $\varphi = 0°$.

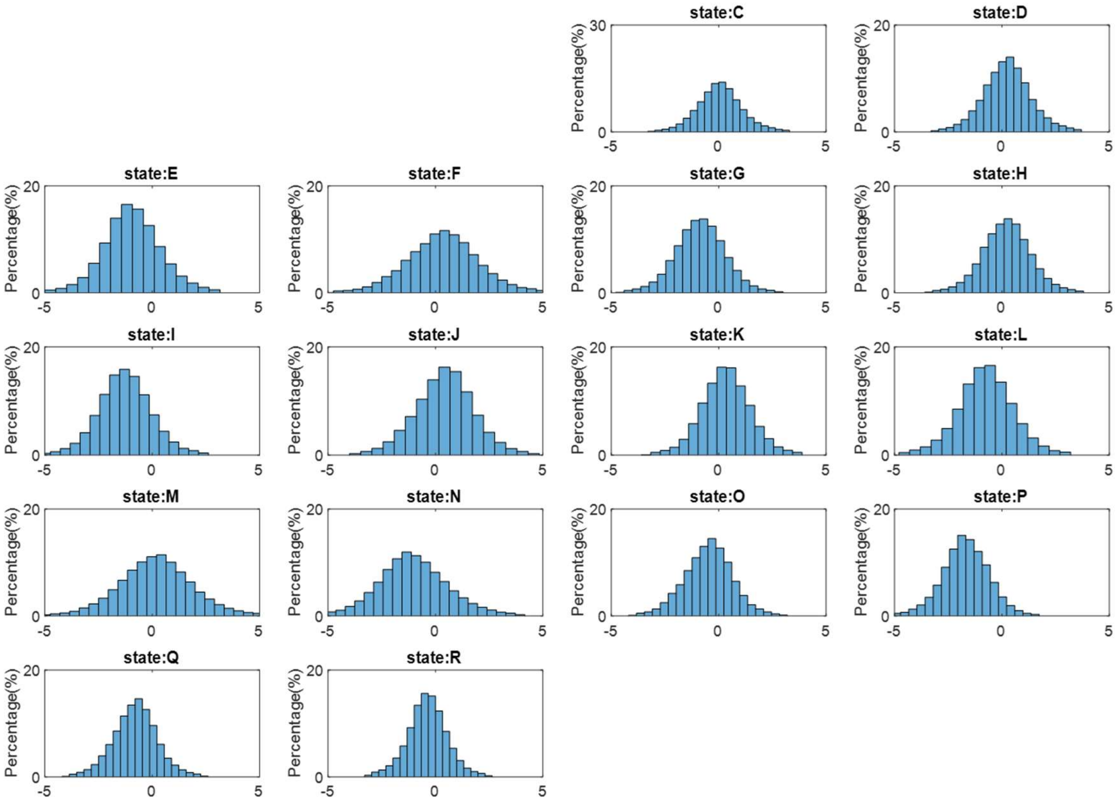

Figure B. 4: AOP measurement error distribution of MPFA under red color input, $\varphi = 10°$.

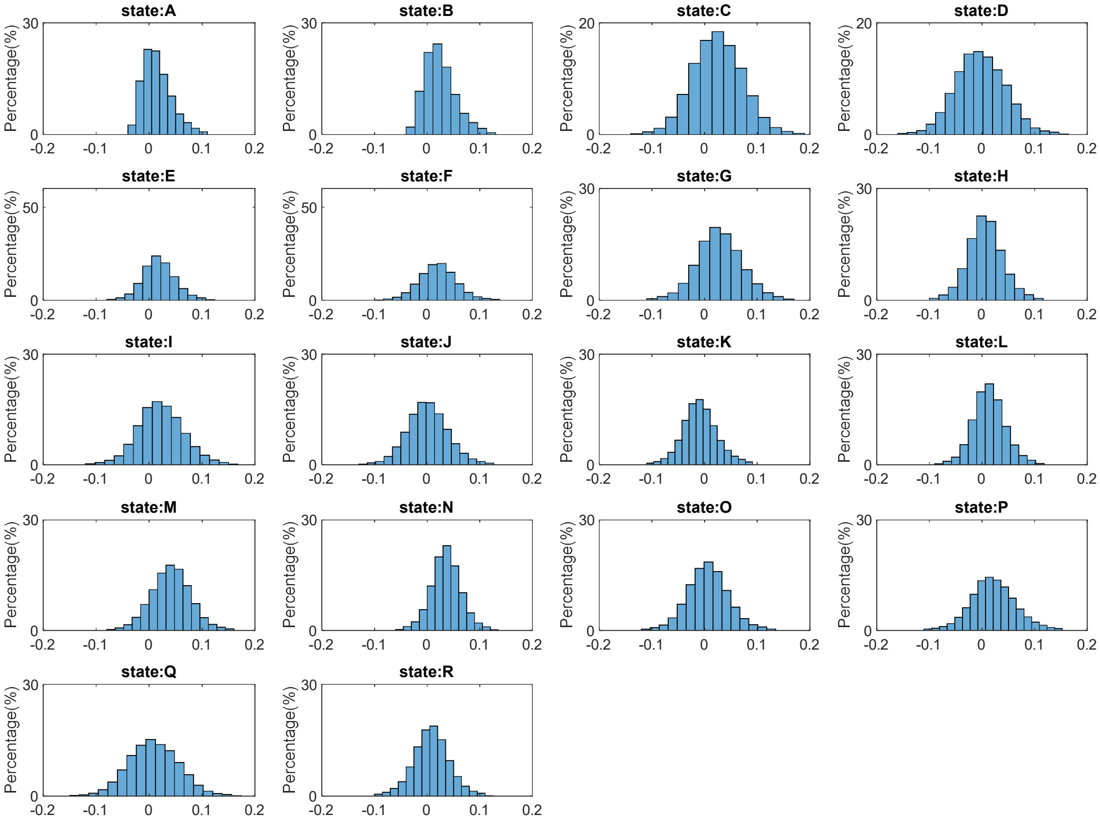

Figure B. 5: DOLP measurement error distribution of MPFA under red color input, $\varphi = 10°$

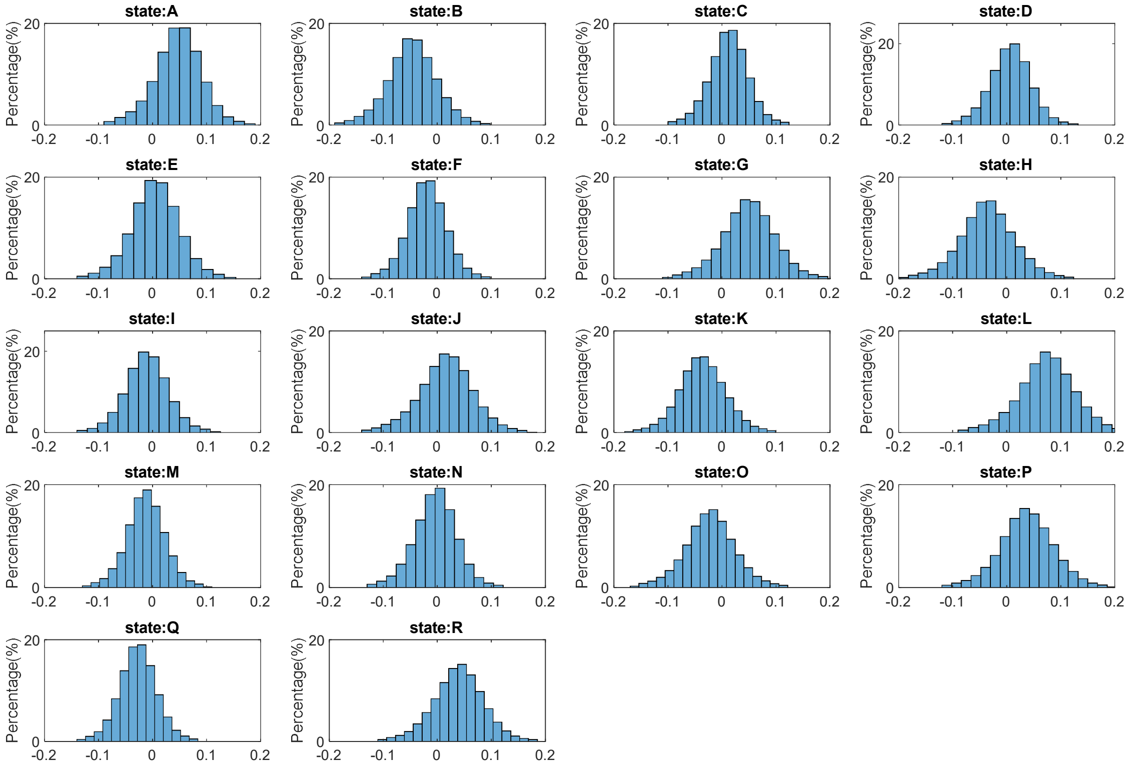

Figure B. 6: DOCP measurement error distribution of MPFA under red color input, $\varphi = 10°$

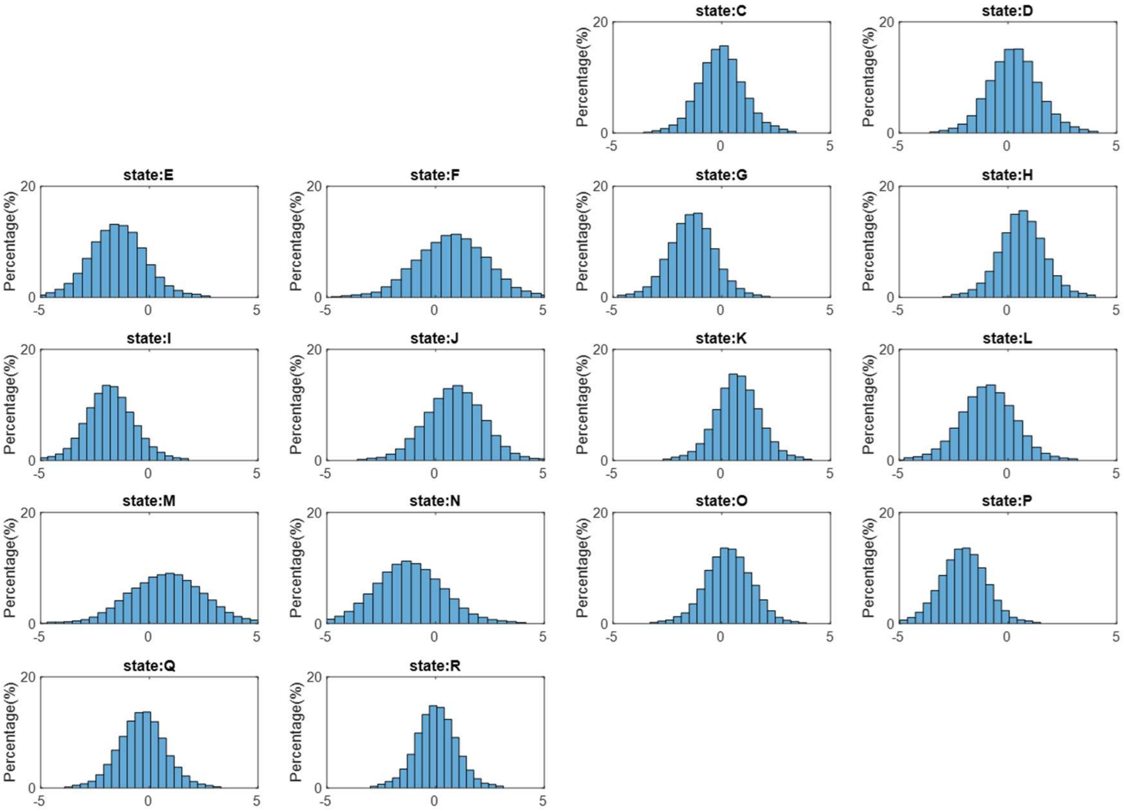

Figure B. 7: AOP measurement error distribution of MPFA under red color input, $\varphi = 20°$.

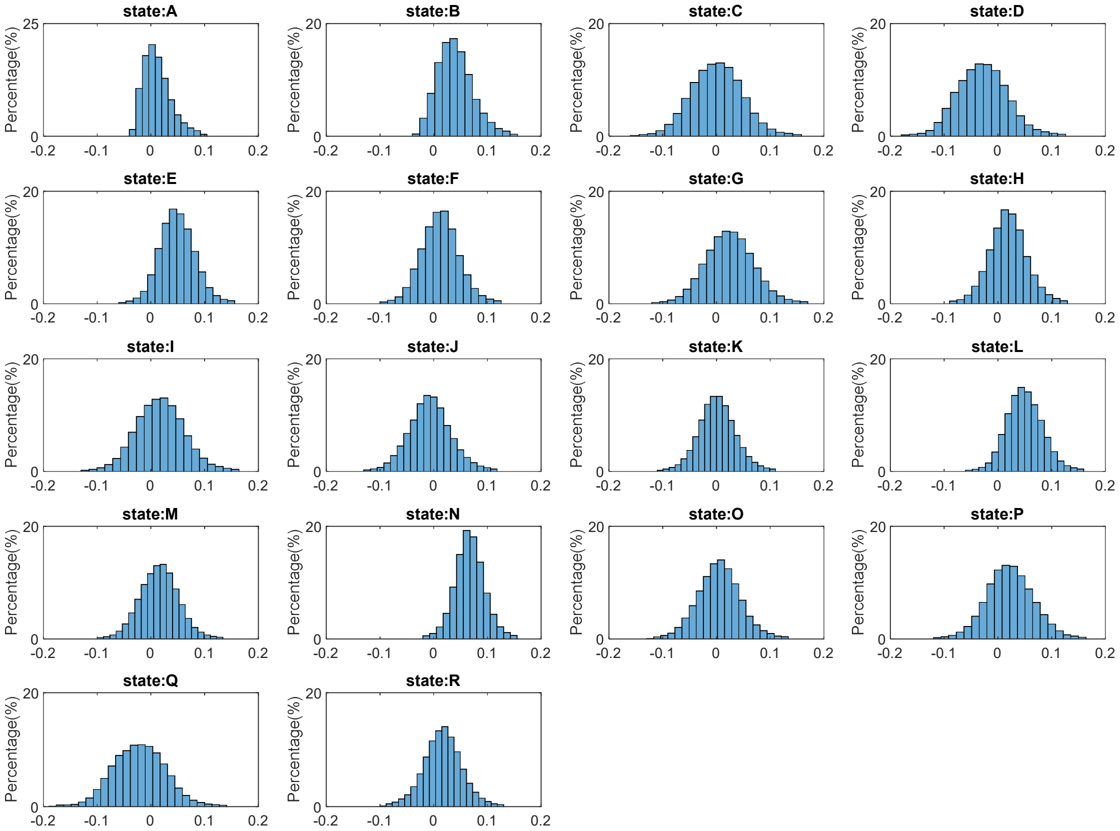

Figure B. 8: DOLP measurement error distribution of MPFA under red color input, $\varphi = 20°$

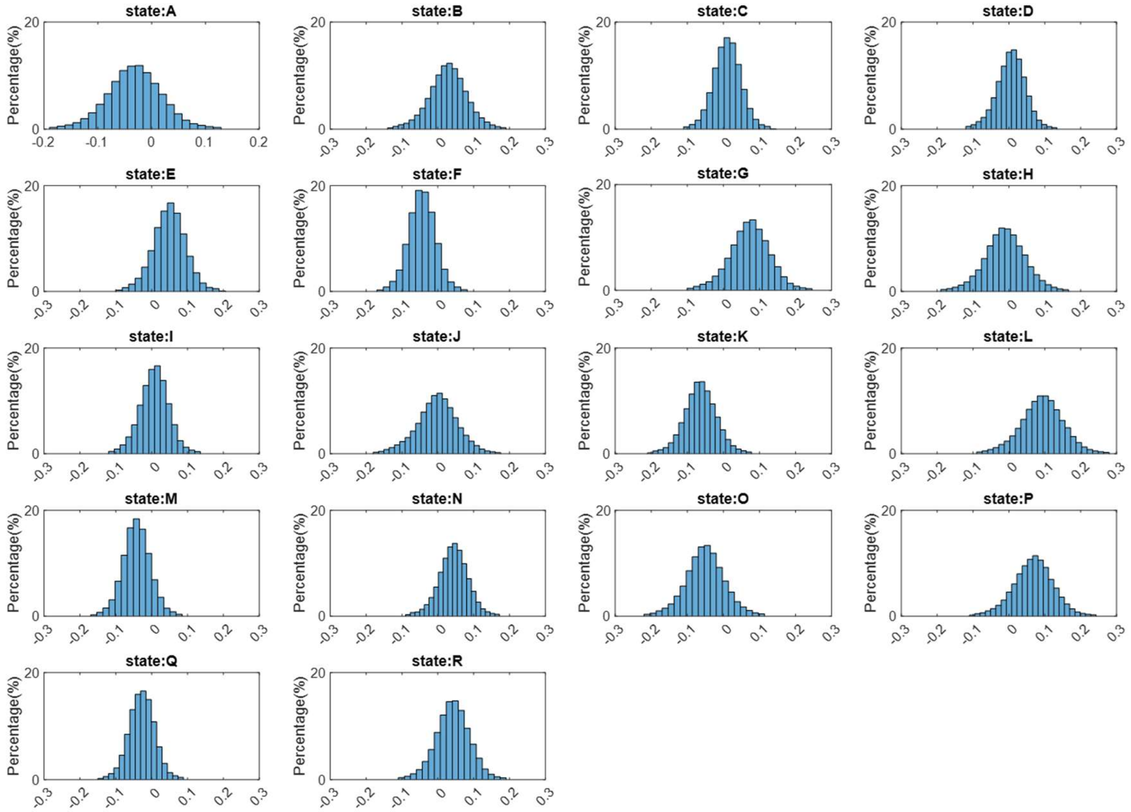

Figure B. 9: DOCP measurement error distribution of MPFA under red color input, $\varphi = 20°$

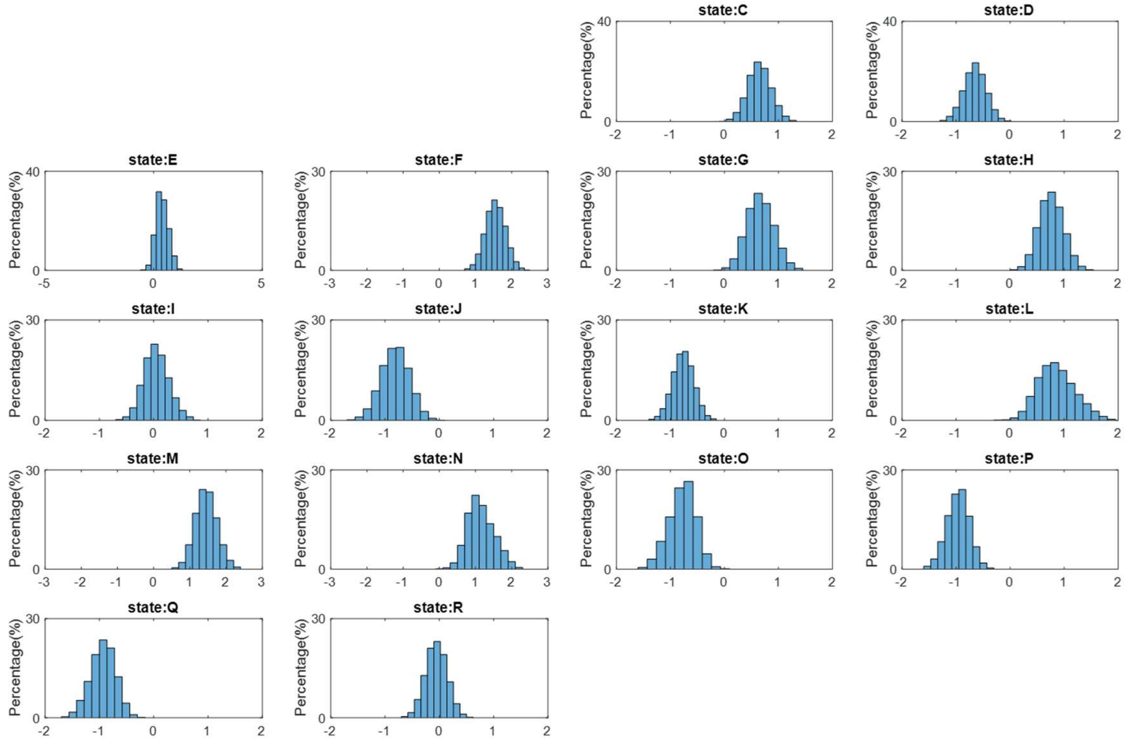

Figure B. 10: AOP measurement error distribution of MPFA under cyan color input, $\varphi = 0°$.

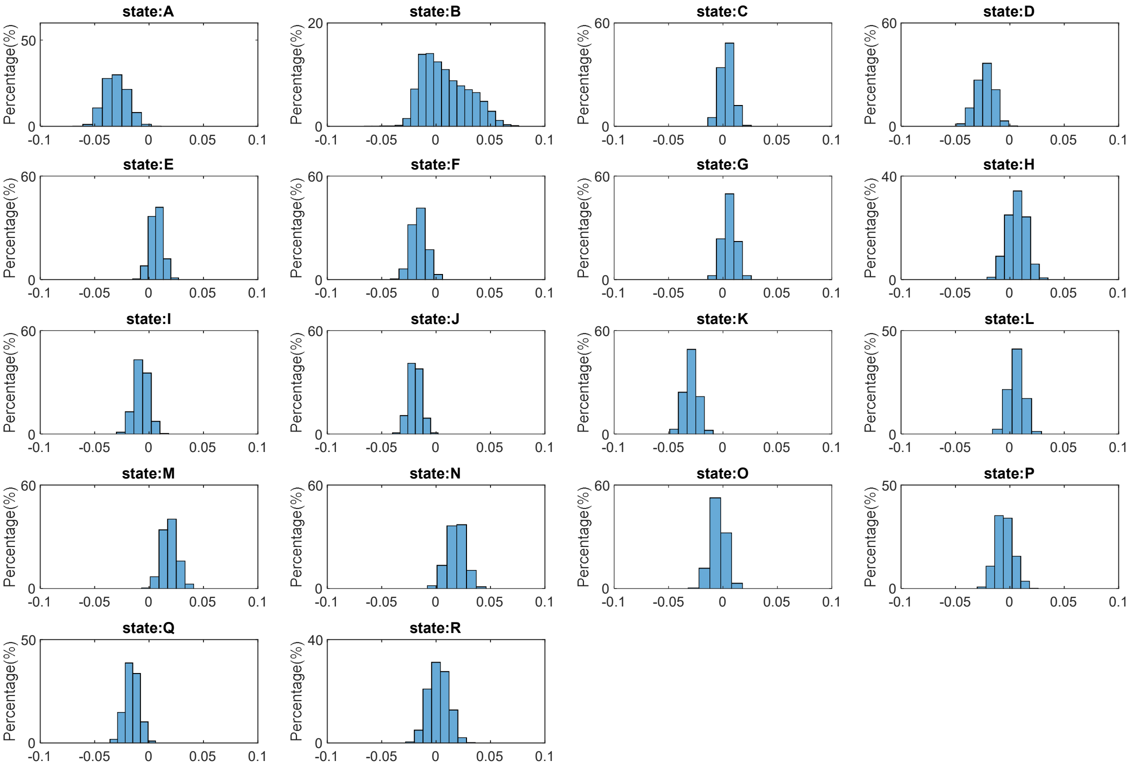
state:A state:B state:C state:D state:E state:F state:G state:H state:I state:J state:K state:L state:M state:N state:O state:P state:Q state:R

Figure B. 11: DOLP measurement error distribution of MPFA under cyan color input, $\varphi = 0°$

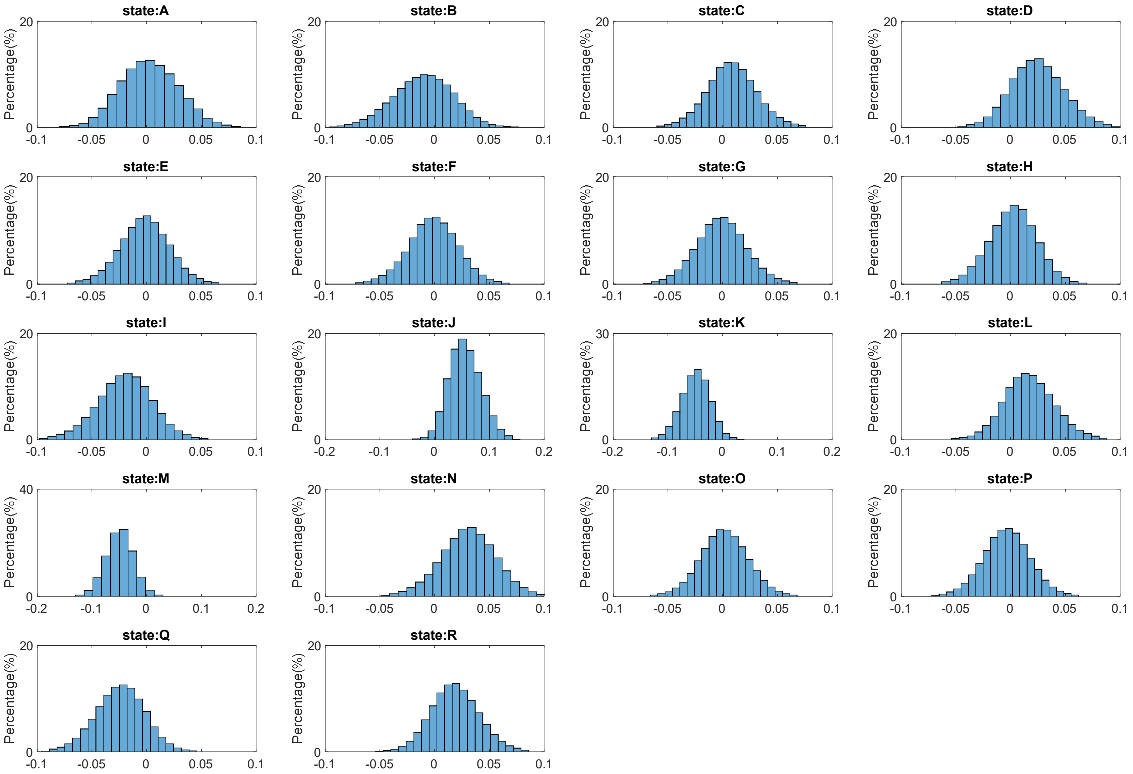

Figure B. 12: DOCP measurement error distribution of MPFA under cyan color input, $\varphi = 0°$

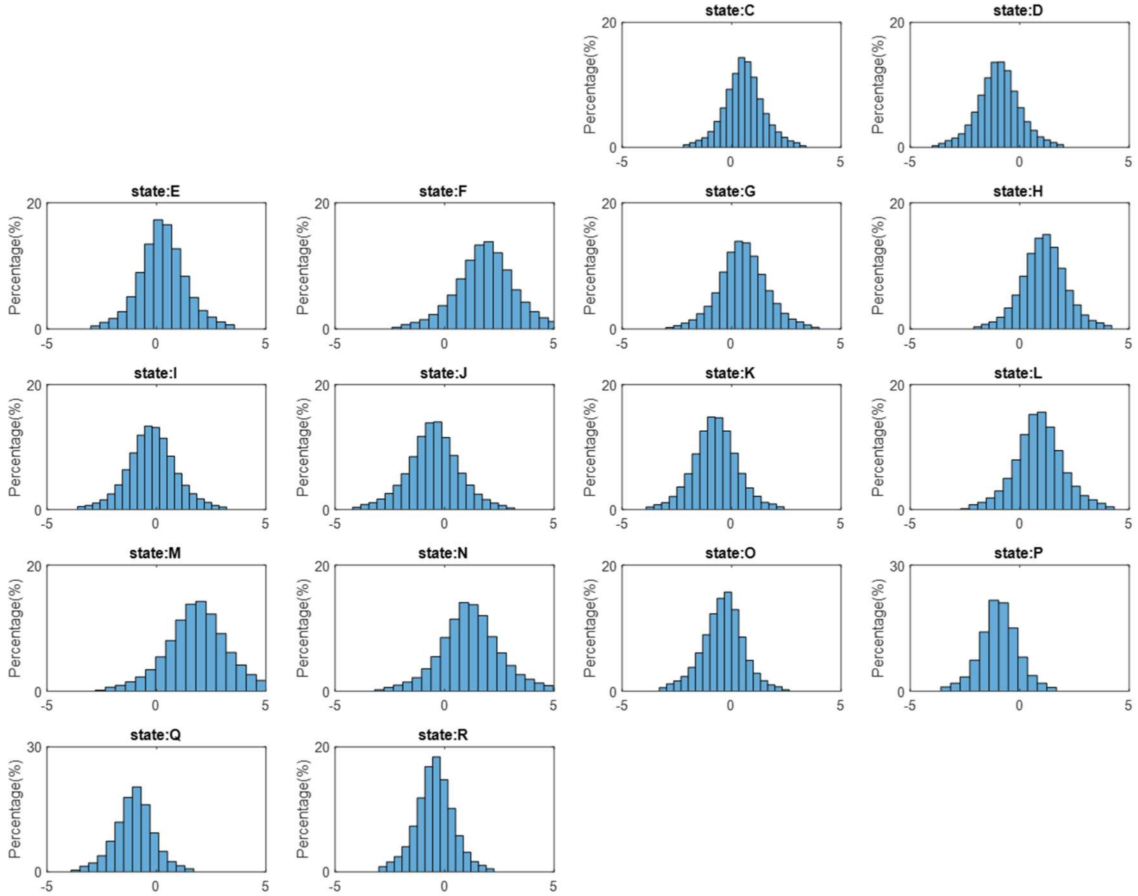

Figure B. 13: AOP measurement error distribution of MPFA under cyan color input, $\varphi = 5°$.

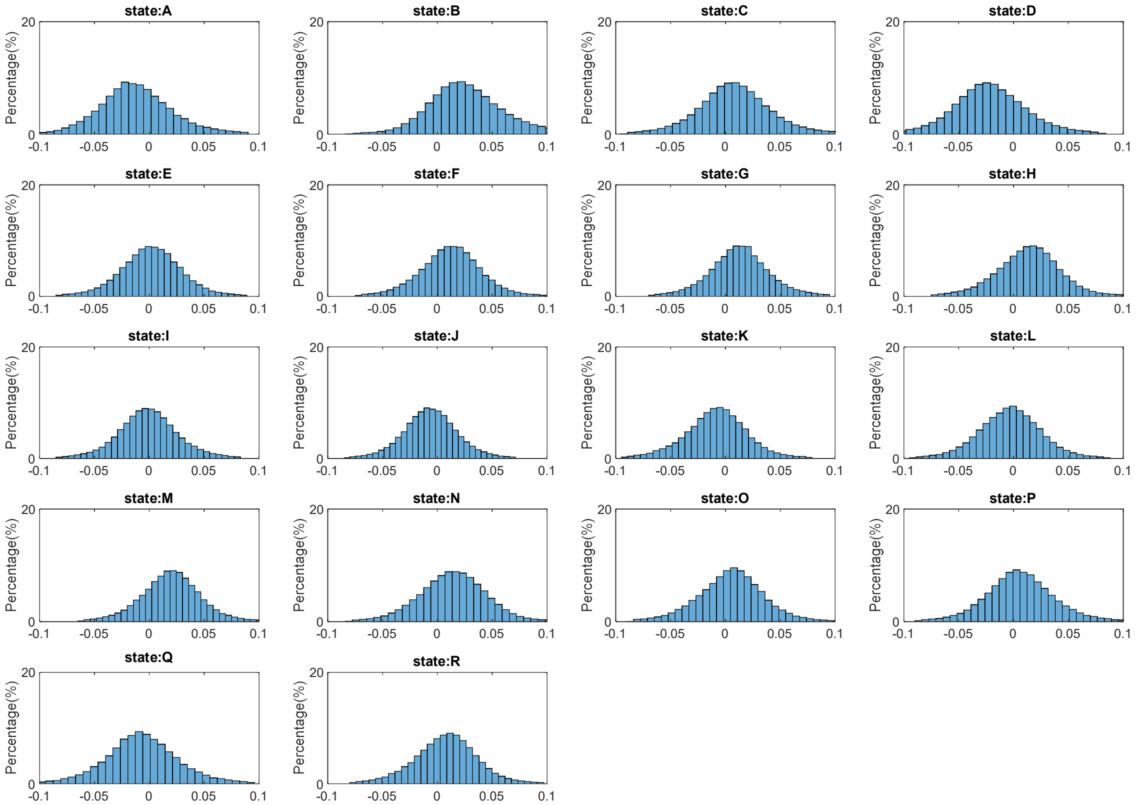

Figure B. 14: DOLP measurement error distribution of MPFA under cyan color input, $\varphi = 5°$

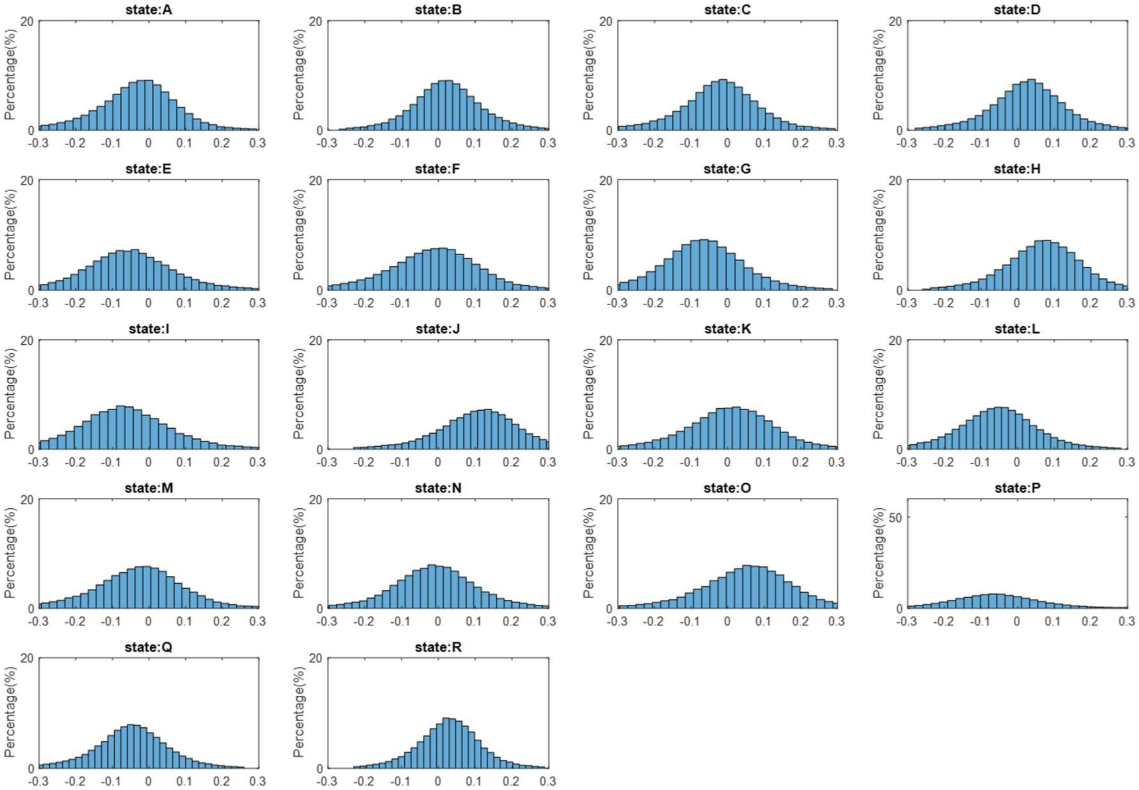

Figure B. 15: DOCP measurement error distribution of MPFA under cyan color input, $\varphi = 5^{\circ}$

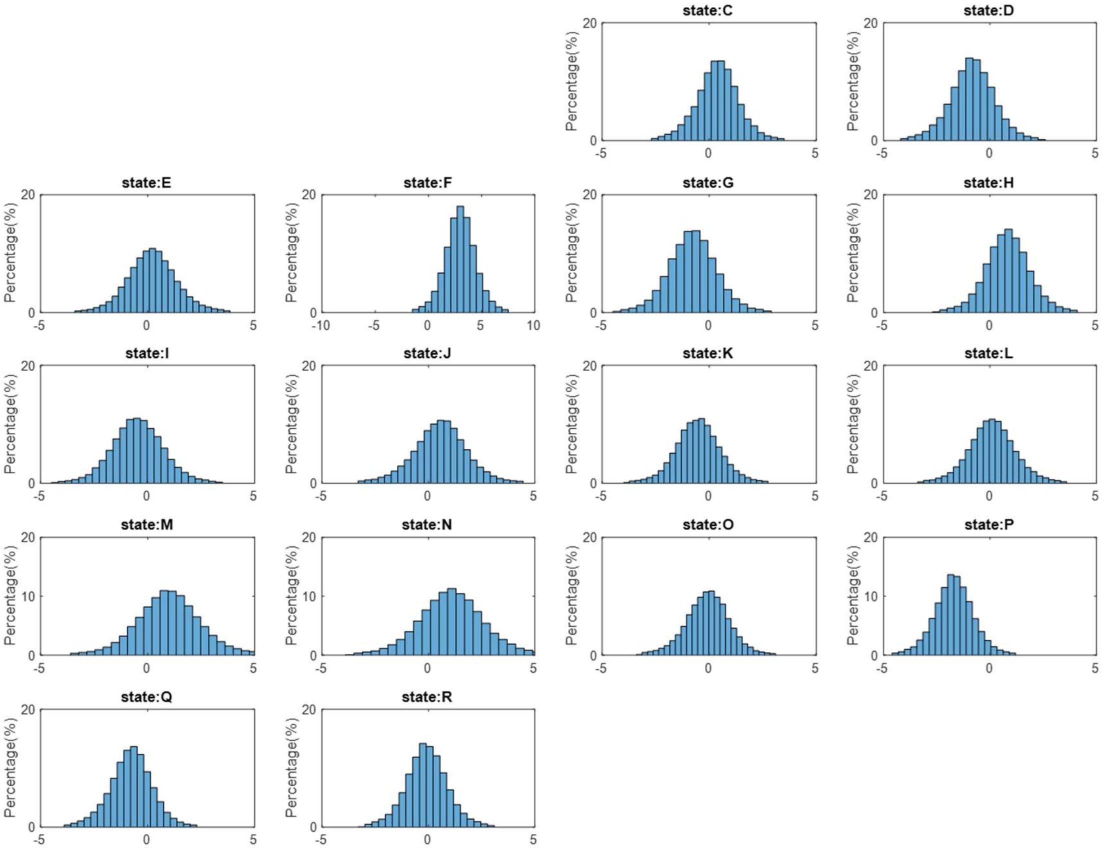

Figure B. 16: AOP measurement error distribution of MPFA under cyan color input, $\varphi = 10°$.

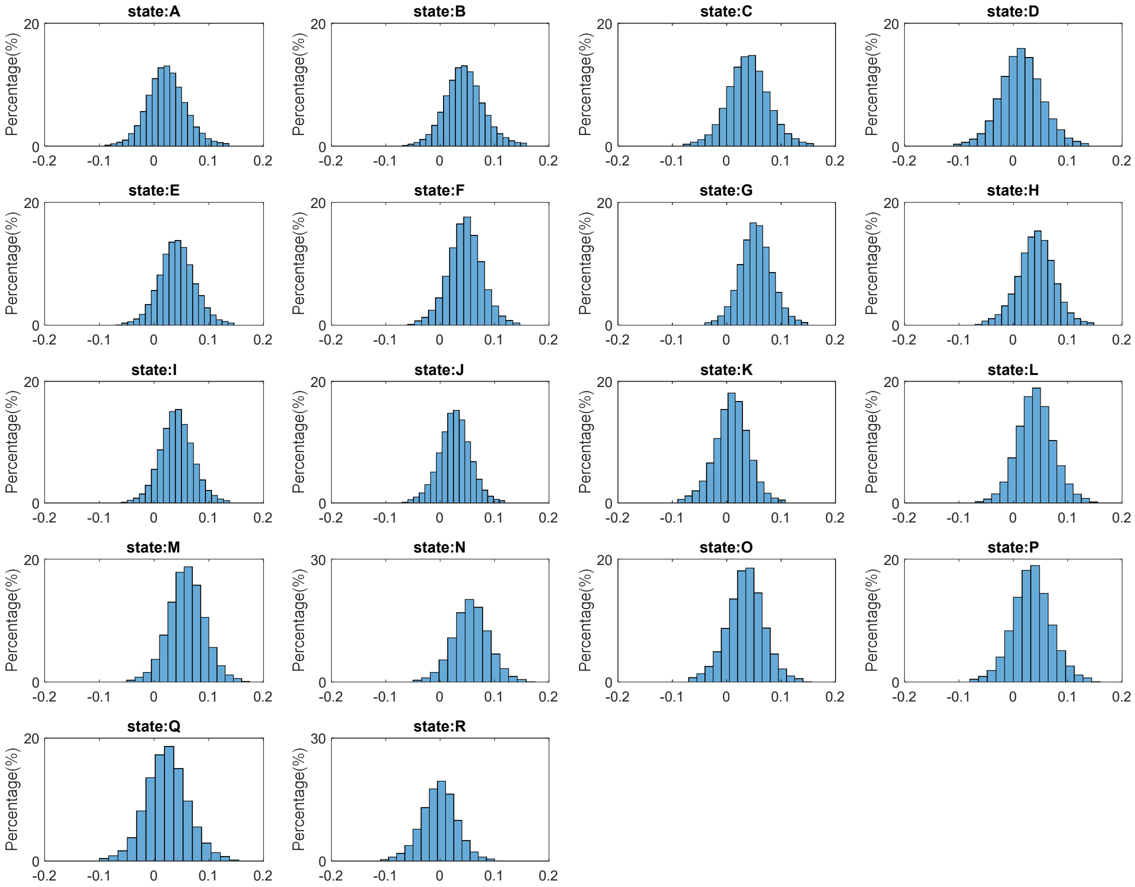

Figure B. 17: DOLP measurement error distribution of MPFA under cyan color input, $\varphi = 10°$

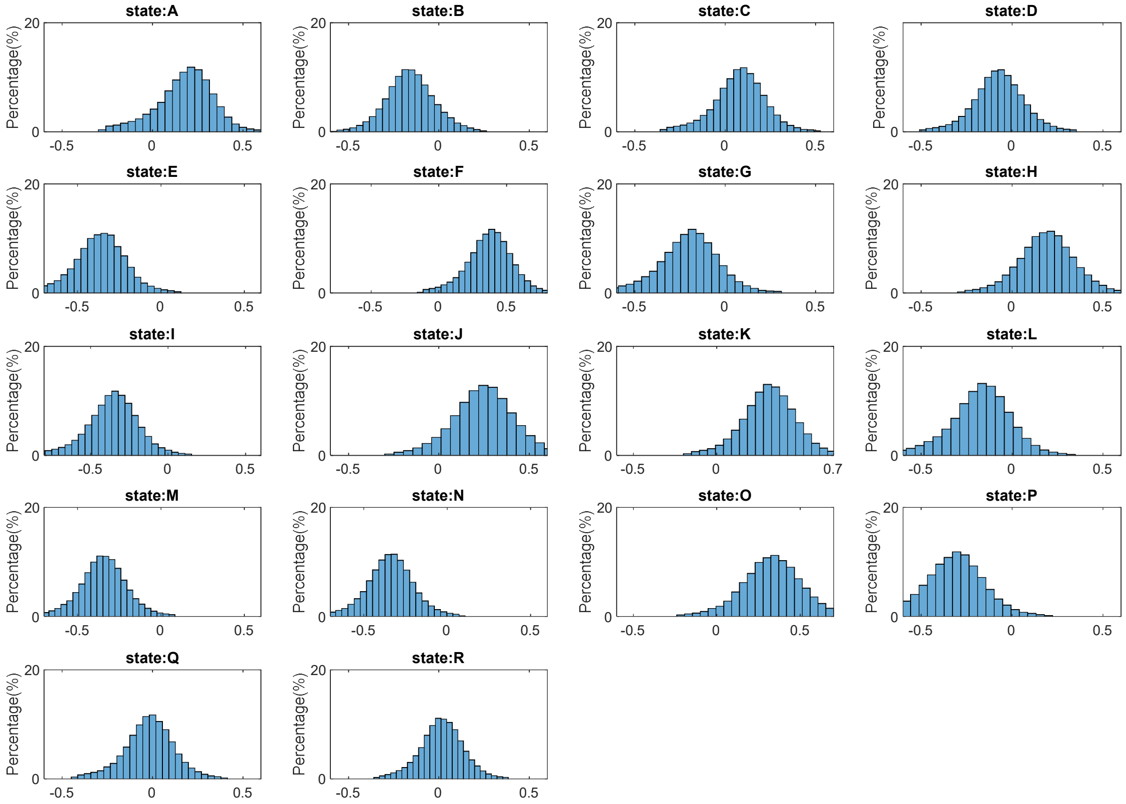

Figure B. 18: DOCP measurement error distribution of MPFA under cyan color input, $\varphi = 10°$

APPENDIX C

CHARACTERIZATION DETIALS OF COMPACT MUELLER MATRIX MICROSCOPE BASED ON CHIP-INTEGRATED FULL-STOKES POLARIMETRIC IMAGING SENSOR

Measurement

Measurement of polarization states using PSA. Light coming from a High-Intensity Fiber coupled Halogen lamp light source (Thorlabs OSL2) is firstly collimated using a parabolic mirror (Thorlabs MPD129-P01), and the iris is applied to control the beam divergence angle. The bandpass filter (red: FBH650-40 cyan: FBH500-40) is applied for wavelength selection. Lens with F=30(AC254-030-AB) and F=100(AC254-100-AB) are applied for beam expansion. The final beam divergence is controlled to be 0.5 degrees with a spot size of 9mm in diameter. Arbitrary polarization states were generated using a broadband linear polarizer (WP25M-UB by Thorlabs, Inc.) and super achromatic QWP (SAQWP05M-700 by Thorlabs, Inc.) A list of Stokes parameters was first designed, then each polarization state was normally incident onto the polarization imager. These polarization states were firstly measured by the rotation of a linear analyzer (LPIREA100-C); the transmitted intensity was then fitted to obtain the polarization states.

Mueller matrix measurement in transmission mode. Four linear polarization input corresponding to LP axis of 0° 45° 90° 135° were firstly taken, followed RCP and LCP input. These six input polarization states can be written as S_{in}^{6} , and correspondent transmitted polarization states were measured by the MPIS, denoted as S_{out}^{6} , the corresponding MM of sample M_{sample}^{T} can be obtained using the equation:

$$M_{sample}^{T} = S_{out} \cdot {S_{in}^{6}}^{-1} \tag{C.1}$$

Mueller matrix measurement in reflection mode. Similar to transmission mode, six polarization states correspond to 0° 45° 90° 135° LP, RCP and LCP were taken. The corresponding MM of sample M_{sample}^{R} can be obtained using equation:

$$M_{sample}^{T} = S_{out} \cdot {S_{in}^{6}}^{-1} \cdot {M_{PSG}^{R}}^{-1} \quad \text{(C.2)}$$

Mueller matrix of Si metasurface, honeybee wings and human lung tissues

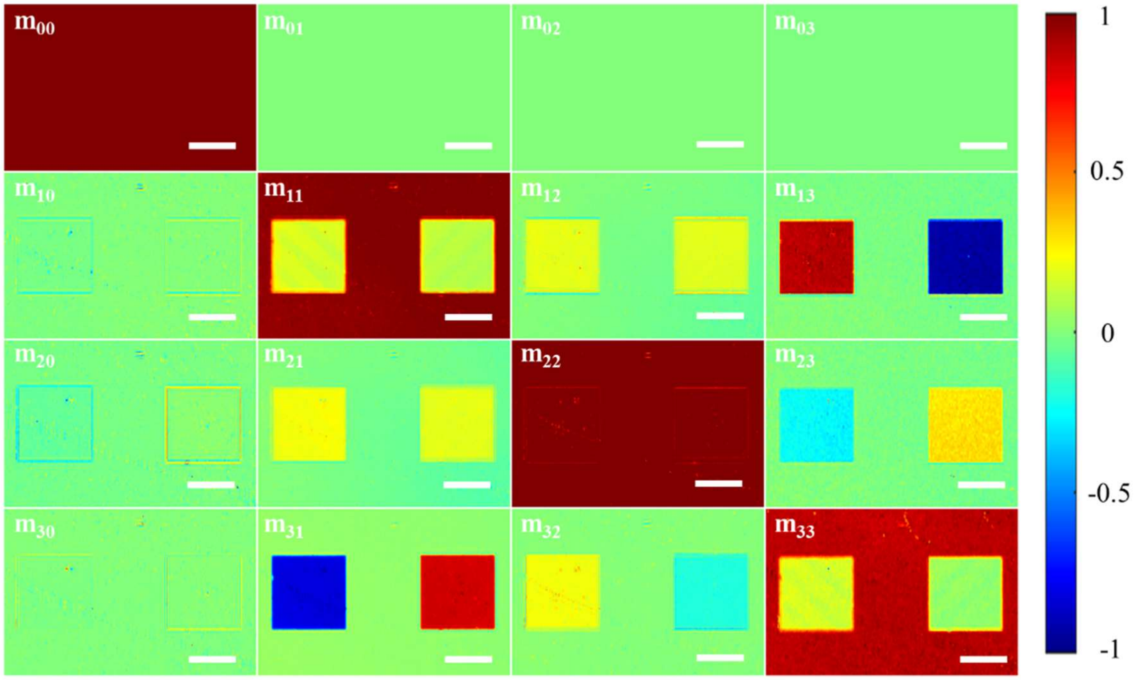

Figure C. 1: Full Mueller matrix image of Si metasurface under red color. Scale Bar: 100μm.

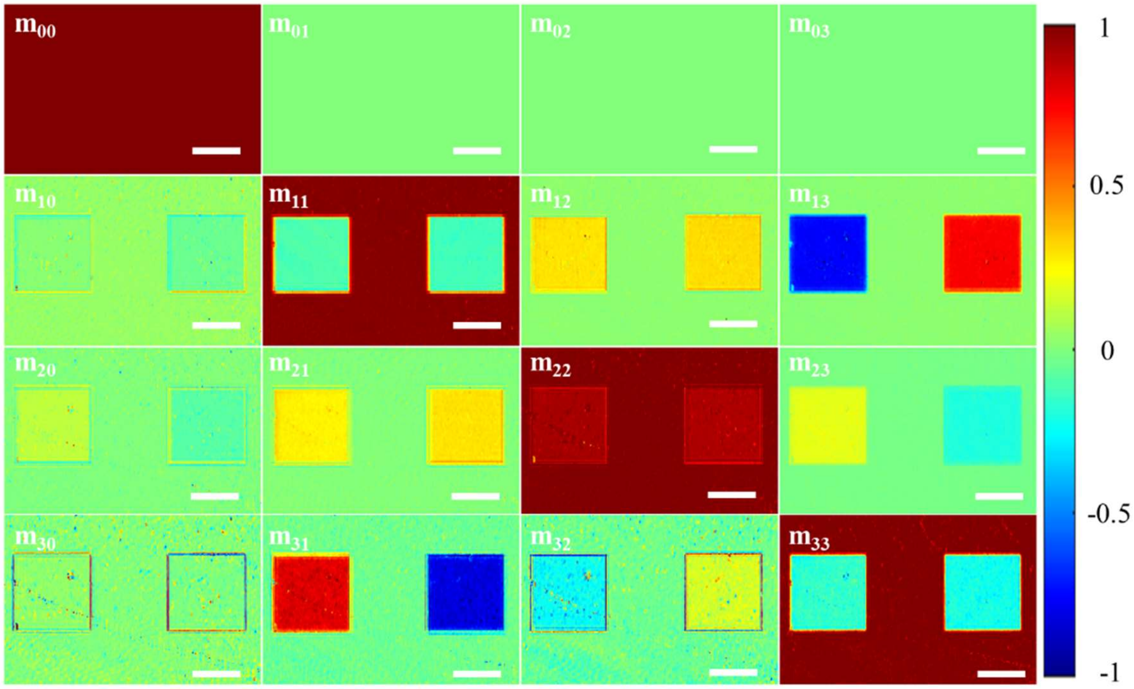

Figure C. 2: Full Mueller matrix image of Si metasurface under cyan color(transmission mode). Scale Bar: 100μm.

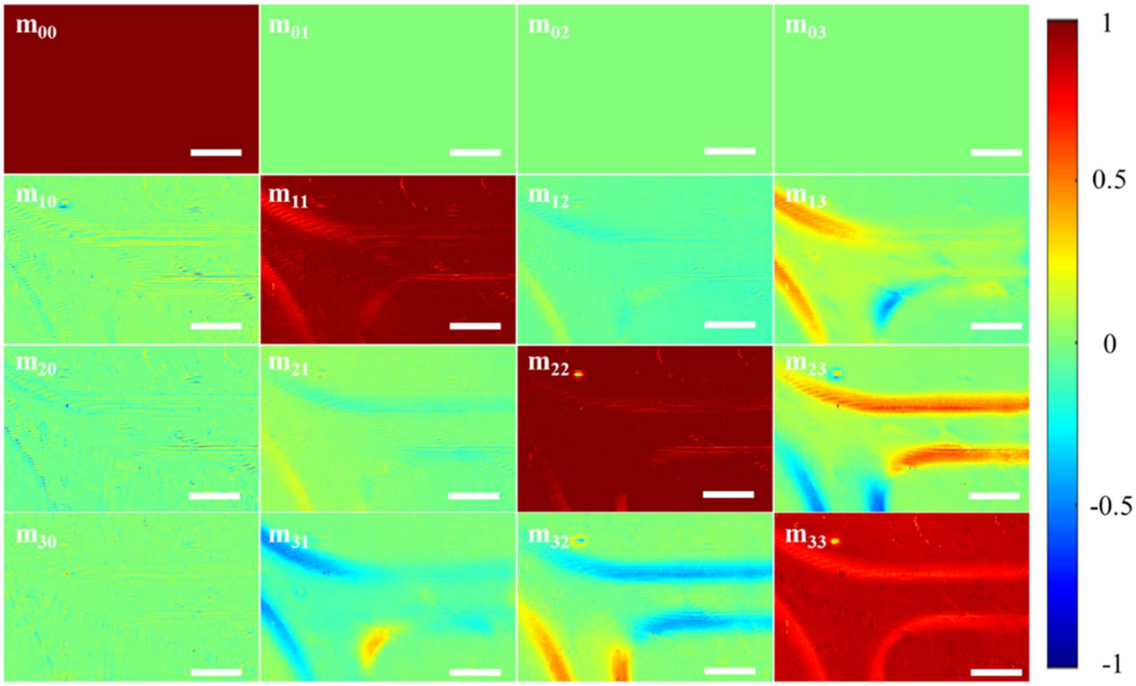

Figure C. 3: Full Mueller matrix image of honeybee wings under red color(transmission mode). Scale Bar: 100µm.

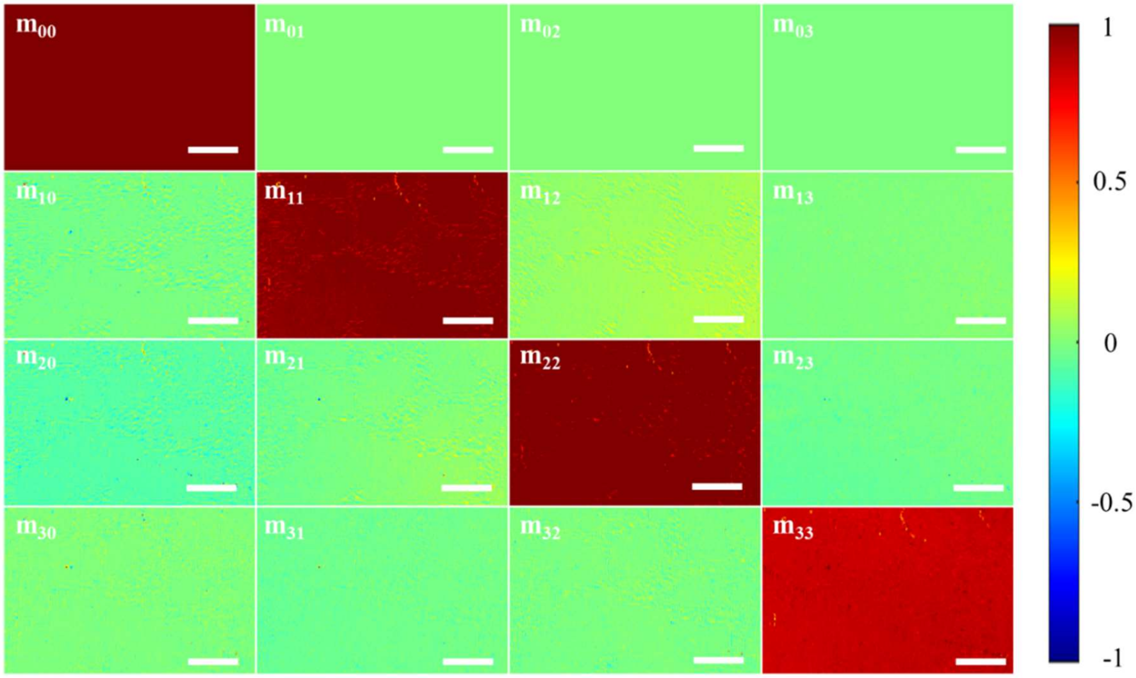

Figure C. 4: Full Mueller matrix image of human lung tissues under red color (transmission mode). Scale Bar: 100μm.

APPENDIX D

MATLAB CODE FOR POLARIZATION ABERRATION ANALYSIS USING ZEMAX POLARIZATION RAY TRACING

Code for polarization aberration calculation using Zemax polarization

ray tracing results

```
close all;
clear all;

%% The code below calculate the normalized mueller matrix of the
sample , it requires input of 40/45/90/135 degree linear polarization
input
file_path="D:\lens simulation\polarization ray tracing\Fisheye";

result = [];
%%

lens_type="US02601805-1_12";
incidnece_angle=0:2:6;
incidence_polarization=["LP_0" 'LP_90' 'LP_45' 'LP_-45' 'LCP' 'RCP'];
        input_matrix=[1,1,1,1,1,1; ...
                      1,-1,0,0,0,0 ;...
                      0,0, 1,-1, 0,0; ...
                      0,0,0,0 , -1, 1 ;...
            ];
for i=1:length(incidnece_angle)
    for j=1:6

file_name=strcat(lens_type,'_',incidence_polarization(1,j),'_',num2str(
incidnece_angle(i)),' degrees incidence_580nm','.txt');%"fish_eye_45
degree_LCP.txt";
       Data=read_lens_file_polarization(file_path,file_name);
        position_x=Data{1}(:,1);
        position_y=Data{1}(:,2);
        Ex=Data{1}(:,3);
        Ey=Data{1}(:,4);
        I=Data{1}(:,5);
        Phase=Data{1}(:,6);
        for o=1:length(Ex)

[S0(o),S1(o),S2(o),S3(o)]=Jones2Stokes(Ex(i),Ey(i),Phase(i));
        end

        S0=mean(S0(:));
        S1=mean(S1(:));
        S2=mean(S2(:));
        S3=mean(S3(:));
        S1=S1/S0;
        S2=S2/S0;
        S3=S3/S0;
        S0=S0/S0;
        output_matrix(1:4,j)= [S0; S1;S2;S3];
        output_matrix;

    end
```

```
    M{i}=output_matrix/input_matrix;% mueller matrix of different
incindent angle
    output_matrix=zeros(4,6);
end
Mueller_matrix.matrix=M;
%% Let's give some test case to check whether the mueller matrix makes
sense
% set a input as [1,1,0,0]
phi = 0:10:170;%0;%0:10:170;
chi = 0;%0:5:35;
x0=10;
y0=10;
width=400;
height=300;
for jj=1:length(phi)
    for ii=1:length(chi)
        for m=1:length(Mueller_matrix.matrix)
            S_in =
[1,cos(2*phi(jj)/180*pi).*cos(2*chi(ii)/180*pi),sin(2*phi(jj)/180*pi).*
cos(2*chi(ii)/180*pi),sin(2*chi(ii)/180*pi)]';
            DOLP_in = sqrt(S_in(2,:).^2+S_in(3,:).^2);
            AOP_in_2=atan(S_in(3,:)./(S_in(2,:)))/pi*180;
            S_out=Mueller_matrix.matrix{m}*S_in; % 0 degree

[AOP(m,ii,jj),DOLP(m,ii,jj),DOCP(m,ii,jj)]=stokes_to_AOP_DOLP_DOCP(S_ou
t);

[AOP_in(m,ii,jj),DOLP_in(m,ii,jj),DOCP_in(m,ii,jj)]=stokes_to_AOP_DOLP_
DOCP(S_in);
            AOP_error(m,ii,jj)=AOP_in(m,ii,jj)-AOP(m,ii,jj);
            DOLP_error(m,ii,jj)=DOLP_in(m,ii,jj)-DOLP(m,ii,jj);
            DOCP_error(m,ii,jj)=DOCP_in(m,ii,jj)-DOCP(m,ii,jj);
            if AOP_error(m,ii,jj)>90
                AOP_error(m,ii,jj)=AOP_error(m,ii,jj)-180;
            elseif AOP_error(m,ii,jj)<-90
                AOP_error(m,ii,jj)=AOP_error(m,ii,jj)+180;
            end
        end

        Mueller_matrix.icindence_angle=incidnece_angle;
% save(strcat('Mueller_matrix_',lens_type,'.mat'),'Mueller_matrix');
%% Now, import the AOP angle response as well as the ray incidence
angless
        file_path="D:\lens simulation\polarization ray
tracing\Fisheye\ray";
        lens_type="fish_eye_180_";

incidnece_angle=0:5:90;%["0","0.6875","1.3750","2.0625","3.4375","4.125
0","4.8125","5.5000"];
        incidence_ray=["LowerRay" 'UpperRay'];
        for i=1:length(incidnece_angle)
            for j=1:2

file_name_ray=strcat(lens_type,incidence_ray(j),'_',num2str(incidnece_a
ngle(i)),' degrees incidence_580nm','.txt');
```

```
Ray_data=read_lens_file_polar_rays(file_path,file_name_ray);
                Angle_Incidence(i,j)=Ray_data{1}(18,11);

            end
             Average_incidence(i)=mean(Angle_Incidence(i,:));
        end
 % 0 90 45 135
% fisheye ray tracing
    end
end
temp(:,:)=AOP_error(1:4,1,1:length(phi));
% temp2(:,:)=AOP_in(1:19,1,1:18);
% da=0:2:6;
%% Plot results

da=0:2:6;
figure;pcolor(phi',da',temp);hcb=colorbar;colormap(jet(256));shading
interp; ylabel('Incidence
Angle');xlabel('{\phi}');set(gcf,'position',[x0,y0,width,height]);
colorTitleHandle = get(hcb,'Title');
titleString = 'AOP error';
set(colorTitleHandle ,'String',titleString);set(gca, 'FontSize', 18);

temp(:,:)=DOLP_error(1:4,1,1:length(phi));
figure;pcolor(phi',da',abs(temp));hcb=colorbar;colormap(jet(256));shadi
ng interp; ylabel('Incidence
Angle');xlabel('{\phi}');set(gcf,'position',[x0,y0,width,height]);
colorTitleHandle = get(hcb,'Title');
titleString = 'DOLP error';
set(colorTitleHandle ,'String',titleString);set(gca, 'FontSize', 18);
temp(:,:)=DOCP_error(1:4,1,1:length(phi));
figure;pcolor(phi',da',abs(temp));caxis([0
0.01]);hcb=colorbar;colormap(jet(256));shading interp;
ylabel('Incidence
Angle');xlabel('{\phi}');set(gcf,'position',[x0,y0,width,height]);
colorTitleHandle = get(hcb,'Title');
titleString = 'DOCP error';
set(colorTitleHandle ,'String',titleString);set(gca, 'FontSize', 18);

%%
function [data]=read_lens_file_polarization(file_path,file_name)
    opt = {'Delimiter','\t', 'CollectOutput',true};
    fid=fopen(strcat(file_path,'\',file_name));
    tic
    while 1
        str = fgetl(fid);
        while ~strcmpi(str,'    Px     Py           Ex           Ey
Intensity  Phase (Deg)  Orientation') && ~feof(fid)
            str = fgetl(fid);
        end
        break;
    %     if ~ischar(tline), break, end
    %     celldata = textscan(tline,'%f %f %f %f %f %f %f');
    %     matdata = cell2mat(celldata);
```

```
    %     % match fails for text lines, textscan returns empty cells
    %     result = [result ; matdata];
    end
    data = textscan(fid,'%f %f %f %f %f %f %f',opt{:});
    toc
    fclose(fid);
end

function
polarization_pupil_visualize(position_x,position_y,data_to_visualize)
    d=[position_x,position_y,data_to_visualize'];
    X = d(:,1); Y = d(:,2); Z = d(:,3);
    Xs = unique(X);
    Ys = unique(Y);
    Xi = arrayfun( @(x) find(Xs==x), X );
    Yi = arrayfun( @(y) find(Ys==y), Y );
    Li = Yi + (Xi-1) * numel(Ys);
    XYZ = nan(numel(Ys), numel(Xs));
    XYZ( Li ) = Z;
    figure;
    pcolor(Xs,Ys,XYZ);
    shading interp
    colorbar;
    colormap(jet(256));
    set(gca,'FontSize',18);
end


function [data]=read_lens_file_polar_rays(file_path,name)
    opt = {'Delimiter','\t', 'CollectOutput',true};
    fid=fopen(strcat(file_path,'\',name));
    tic
    count=0;
%     while 1
    while count< 22
            str = fgetl(fid);
            count=count+1;
    end
    data = textscan(fid,'%f %f %f %f %f %f %f %f %f %f %f %f',opt{:});
    toc
    fclose(fid);
end


function
[M_output]=Calculate_mueller_matrix_diattenuation_model(arg,theta,ER,ef
ficiency)
%note: here the convention is horizoontal x and vertical y polarized,
%consistent with books, but, when calculate vertical nano
%grating  mueller matrix,you have to be careful because 0 degree nano
%grating detects 90 degree polarized light, so the y and x axis is
flipped.
%Its mueller matrix would be different from traditional convention!
    if arg==1%"Linear diattenuator"
```

```
        q=efficiency;
        r=q/ER;
        M_LP=1/2*[q+r, (q-r)*cos(2*theta),(q-r)*sin(2*theta),0;...
         (q-
r)*cos(2*theta),(q+r)*cos(2*theta).^2+2*sqrt(q*r)*sin(2*theta).^2,(q+r-
2*sqrt(q*r))*sin(2*theta)*cos(2*theta),0;...
         (q-r)*sin(2*theta),(q+r-
2*sqrt(q*r))*sin(2*theta)*cos(2*theta),(q+r)*sin(2*theta).^2+2*sqrt(q*r
)*cos(theta*2).^2,0;...
        0,0,0,2*sqrt(q*r)];
        M_output=M_LP;
    end
    if arg==2% "Linear retarder plus linear diattenuator" essentially a
CP detector, linear diattnuator + lossless linear retarder

        % fast axis 90 degree aSi grating horizontal
        theta_QWP=90/180*pi;
        delta=-pi/2*1.094;% x axis fast axis, y axis slow axis
        M_QWP=[1,0,0,0;...

0,cos(2*theta_QWP).^2+sin(2*theta_QWP).^2*cos(delta),sin(2*theta_QWP)*c
os(2*theta_QWP)*(1-cos(delta)),-sin(2*theta_QWP)*sin(delta);...
        0,sin(2*theta_QWP)*cos(2*theta_QWP)*(1-
cos(delta)),sin(2*theta_QWP).^2+cos(theta_QWP).^2*cos(delta),cos(2*thet
a_QWP)*sin(delta);...
        0,sin(2*theta_QWP)*sin(delta),-
cos(2*theta_QWP)*sin(delta),cos(delta)];

        q=efficiency;
        r=q/ER;
        M_LP=1/2*[q+r, (q-r)*cos(2*theta),(q-r)*sin(2*theta),0;...
         (q-
r)*cos(2*theta),(q+r)*cos(2*theta).^2+2*sqrt(q*r)*sin(2*theta).^2,(q+r-
2*sqrt(q*r))*sin(2*theta)*cos(2*theta),0;...
         (q-r)*sin(2*theta),(q+r-
2*sqrt(q*r))*sin(2*theta)*cos(2*theta),(q+r)*sin(2*theta).^2+2*sqrt(q*r
)*cos(theta*2).^2,0;...
        0,0,0,2*sqrt(q*r)];
        M_output=M_LP*M_QWP;
    end
    if arg==3%for "Linear retarder" consider lossless linear retarder
        M_output=[1,0,0,0;...

0,cos(2*theta).^2+sin(2*theta).^2*cos(delta),cos(2*theta)*sin(2*theta)*
(1-cos(delta)),sin(2*theta)*sin(delta);...
        0,cos(2*theta)*sin(2*theta)*(1-
cos(delta)),cos(2*theta).^2*cos(delta)+sin(2*theta).^2,-
cos(2*theta)*sin(delta);...
        0,-sin(2*theta)*sin(delta),cos(2*theta)*sin(delta),cos(delta)];
    end

    if arg==4
        delta=-pi/2*1.094;
        q=0.3002/sqrt(2);
        r=0.2960/sqrt(2);
```

```
        M_QWP=1/2*[q+r,q-r,0,0;...
            q-r,q+r,0,0;...
            0,0,2*sqrt(q*r)*cos(delta),2*sqrt(q*r)*sin(delta);...
            0,0,-2*sqrt(q*r)*sin(delta),2*sqrt(q*r)*cos(delta)];
        q=efficiency;
        r=q/ER;
        M_LP=1/2*[q+r, (q-r)*cos(2*theta),(q-r)*sin(2*theta),0;...
         (q-
r)*cos(2*theta),(q+r)*cos(2*theta).^2+2*sqrt(q*r)*sin(2*theta).^2,q+r-
2*sqrt(q*r)*sin(2*theta)*cos(2*theta),0;...
         (q-r)*sin(2*theta),(q+r-
2*sqrt(q*r))*sin(2*theta)*cos(2*theta),(q+r)*sin(2*theta).^2+2*sqrt(q*r
)*cos(theta*2).^2,0;...
        0,0,0,2*sqrt(q*r)];
        M_output=M_LP*M_QWP*5.2;
    end

end


function [Ins_theo]=Calculate_instrument_matrix_LP_sensor(LP_info)
    LPER=LP_info.LPER_0;
    efficiency=LP_info.LP_0_efficiency;

M_LP_diatten_0=Calculate_mueller_matrix_diattenuation_model(1,0/180*pi,
LPER,efficiency);
    LPER=LP_info.LPER_90;
    efficiency=LP_info.LP_90_efficiency;

M_LP_diatten_90=Calculate_mueller_matrix_diattenuation_model(1,90/180*p
i,LPER,efficiency);
    LPER=LP_info.LPER_45;
    efficiency=LP_info.LP_45_efficiency;

M_LP_diatten_45=Calculate_mueller_matrix_diattenuation_model(1,45/180*p
i,LPER,efficiency);
    LPER=LP_info.LPER_135;
    efficiency=LP_info.LP_135_efficiency;

M_LP_diatten_135=Calculate_mueller_matrix_diattenuation_model(1,135/180
*pi,LPER,efficiency);
%% theoretical instrument matrix


Ins_theo=[M_LP_diatten_0(1,:);M_LP_diatten_90(1,:);M_LP_diatten_45(1,:)
;M_LP_diatten_135(1,:)];

end


function
[LP_info]=match_incidence_with_lens_angle_response(incidence_angle,LPER
_Angle)
    n=[0,5,10,15,20,25];
```

```
    [val,idx]=min(abs(n-incidence_angle));
    minVal=n(idx);
    LP_info.LPER_0=LPER_Angle.LP0(idx(1));
    LP_info.LPER_90=LPER_Angle.LP90(idx(1));
    LP_info.LPER_45=LPER_Angle.LP45(idx(1));
    LP_info.LPER_135=LPER_Angle.LP135(idx(1));
    LP_info.LP_0_efficiency=1;
    LP_info.LP_45_efficiency=1;
    LP_info.LP_90_efficiency=1;
    LP_info.LP_135_efficiency=1;
end

function [AOP,DOLP,DOCP]=stokes_to_AOP_DOLP_DOCP(Stokes)
    S0=Stokes(1);
    S1=Stokes(2);
    S2=Stokes(3);
    S3=Stokes(4);
    AOP_Gray_2=atan(S2./S1)/pi*180;
    if(S1<0)
        AOP_Gray_2=AOP_Gray_2+180;
    end
    if AOP_Gray_2<0
        AOP_Gray_2=360+AOP_Gray_2;
    end
    DOLP=sqrt(S1.^2+S2.^2)./S0;
    AOP_Gray=0.5*AOP_Gray_2;
    for ii=1:size(AOP_Gray)
      if AOP_Gray(ii)>180
        AOP_Gray(ii)=AOP_Gray(ii)-180;
      end
    end
    AOP=AOP_Gray;
    DOCP=S3;
end



function [S0, S1, S2, S3, Coeff]= Jones2Stokes(Ex, Ey, PhaseDiff)

if nargin == 2

    S0=abs(Ex).^2 + abs(Ey).^2;
    S1=abs(Ex).^2 - abs(Ey).^2;
    S2=2*real(Ex.*conj(Ey));
    S3=-2*imag(Ex.*conj(Ey));

    Coeff = S0;
    S0 = S0./S0; S1 = S1./S0; S2 = S2./S0; S3 = S3./S0;

elseif nargin == 3

    PhaseDiff = PhaseDiff ./180 *pi;
    Ey = Ey.*exp(1i*PhaseDiff);
```

```
    S0=abs(Ex).^2 + abs(Ey).^2;
    S1=abs(Ex).^2 - abs(Ey).^2;
    S2=2*real(Ex.*conj(Ey));
    S3=-2*imag(Ex.*conj(Ey));

    Coeff = S0;
    S0 = S0./Coeff;
    S1 = S1./Coeff;
    S2 = S2./Coeff;
    S3 = S3./Coeff;
else
    Display("Wrong arguments")
end
end
```